Phase behavior of charged colloids

many-body effects, charge renormalization and charge regulation

Phase behavior of charged colloids

many-body effects, charge renormalization and charge regulation

Fasegedrag van geladen colloïden
veel-deeltjesgedrag, ladingsrenormalizatie en ladingsregulatie

(met een samenvatting in het Nederlands)

Proefschift

ter verkrijging van de graad van doctor aan de Universiteit Utrecht
op gezag van de rector magnificus, prof.dr. W.H. Gispen, ingevolge
het besluit van het college voor promoties in het openbaar te
verdedigen op vrijdag 8 september 2006 des middags te 12:45 uur

door

Bastiaan Zoetekouw

geboren op 29 oktober 1977 te Tiel

Promotor: prof.dr. H. van Beijeren
Copromotor: dr. R. van Roij

The work described in this thesis is part of the research programme of the '*Stichting voor Fundamenteel Onderzoek der Materie (FOM)*', which is financially supported by the '*Nederlandse Organisatie voor Wetenschappelijk Onderzoek (NWO)*'.

ISBN-10: 90-393-4341-1
ISBN-13: 978-90-393-4341-8

The full text of this thesis is available from from http://www.zoetekouw.net/bas/PhDthesis.pdf.

Contents

CHAPTER 1

Introduction: Soft Matter and Colloids

1.1 Soft matter

The term "soft matter" is used to describe a huge variety of different systems, ranging from polymer networks to virus particles, and from clays to cell membranes. The general characteristic of these systems is that they consist of mesoscopic particles, often in a background of microscopic solvent particles.

De Gennes, who in his 1991 Nobel lecture coined the term "soft matter" [1], identified the two main features of such systems to be *flexibility* and *complexity*. The flexibility, and the adjective "soft" in "soft matter", refer to the soft mechanical response of such systems: they are often easily deformable, compressed or sheared.

Furthermore, soft matter systems are generally very complex. One cause for this complexity is the huge zoo of different particles that such systems can consist of: apart from the rigid, spherical colloidal particles that will be the main focus of this thesis, also surfactants, polymers, lipids, viruses, proteins and other macromolecules, and all kinds of irregularly shaped particles might be present. An additional complication is the generally very large scale difference in soft matter systems. Colloidal particles, for example, might be as large as 1 μm, with a charge of several thousand electron charges, but to fully describe such a colloidal system, also the interactions with monovalent micro-ions of a few Ångströms in size have to be taken into account. This makes theoretical modeling of these systems highly nontrivial.

Because of the mesoscopic length scales of particles in soft matter systems, these systems can be described using classical statistical mechanics and, usually, no quantum effects are involved. On the other side, the particles are small enough

not to be totally governed by gravity and friction (like, for example, granular systems are). Another consequence of the mesoscopic sizes of soft matter systems is that the typical energy scales are of the order of the thermal energy. The dynamics is therefore governed by (overdamped) Brownian motion and thermal fluctuations.

There has been much interest in soft matter systems lately, both from fundamental and applied sciences, and from industry. Soft matter systems are omnipresent in industry; their applications range from liquid crystal displays in televisions and computer screens to yogurt and sun tan lotion. Also new applications of soft matter systems, like electronic paper and photonic band-gap materials, are rapidly being developed.

One of the reasons why soft matter systems are interesting from a fundamental point of view, is that they are much easier to observe in real space and real time than conventional, microscopic condensed matter systems. In addition, very well characterized particles (such as mono-disperse colloids or polymers) can be synthesized, and their interactions can be easily tuned, either by modifying the chemical composition of the materials, or by varying the environmental parameters, like changing the solvent that is used or adjusting the concentration of background ions. Also, because of the mesoscopic size of the particles, they can be tracked easily using optical microscopy, and individual particles can be manipulated using, for example, optical tweezers. On top of this, the increase in computer power in the past decade has made study of soft matter systems by Monte-Carlo simulations and molecular dynamics a viable area of research.

Another appealing aspect of these complex systems is the large connection and overlap of soft matter physics with (molecular) biology and (physical) chemistry. Indeed, solutions of DNA molecules and proteins are typical examples of soft matter systems; to understand their behavior in biological systems, one has to combine the chemistry of the DNA molecules with soft matter physics of charged, flexible rods mixed with microscopic cations and anions. Soft matter systems therefore constitute a great new challenge at the borders of physics, chemistry and biology.

1.2 Colloids

A specific example of soft matter systems are colloidal suspensions. These are multi-components systems that consist of mesoscopic particles suspended in a molecular solvent, for example pigment particles in paint or ink, or fat droplets in milk. Often other chemical components are present as well, e.g., microscopic ions, polymers, or proteins. The colloidal particles themselves range in size from several nanometers to a few microns, and can have all kinds of different shapes. Apart from, for example, naturally occurring colloidal particles like clay platelets in mud, it is nowadays possible to create all kinds of different particles in laboratory: silica or metallic spheres [2, 3], needles [4], magnetic particles [5, 6], dumbbell-shaped particles [7], particles with cores and shells of different materials [8], hollow particles [9], dipolar spheres [10], etc.

Experimentally, one has very much control over the synthesis of these particles, and very mono-disperse and well characterized systems can be synthesized nowadays. In experimental setups, colloidal particles can be visualized and controlled extremely well: using confocal video-microscopy the trajectories of thousands of colloids can be imaged and followed in real space, and by using laser-tweezers many particles can be individually controlled and manipulated simultaneously (see, e.g., Refs. [11, 12]). Because of this very accurate control, colloidal suspension are very nice model systems for condensed matter systems, as certain phenomena, such as phase transitions and structures, can be studied in much more detail than in, e.g., atomic or molecular systems. An example is the recent experimental observation in real space of capillary waves at the gas–liquid interface between two coexisting phases in a colloid–polymer mixture [13, 14]. In microscopic condensed matter systems, capillary waves can only be studied in scattering experiments.

Predicting or understanding the properties of colloidal systems from a microscopic perspective is generally complicated, because the large asymmetry in size and charge between the colloids and the other components in practice inhibits a treatment of all the components on an equal footing. The standard way out is to regard the suspension as an effective system of colloids only, in which all microscopic degrees of freedom of the medium (solvent, ions, polymers, etc.) are suitably averaged out.

For instance, in the case of colloidal hard spheres in a medium with non-adsorbing ideal polymers, the so-called depletion effect [15, 16] leads to effective attractions between pairs of colloids at separations comparable to the polymer sizes, and in the case of charged colloidal spheres in an electrolyte with Debye length κ^{-1}, the effective interaction between a colloidal pair at center-to-center separation r becomes a repulsive screened-Coulomb potential $\propto \exp(-\kappa r)/r$. The advantage of such a one-component viewpoint is that all of the machinery of classical one-component fluids (integral equations, perturbation theory, simulations, etc.) can be employed to study the equilibrium properties of colloidal suspensions. Performing this averaging explicitly is generally a tremendous statistical mechanics problem, that can only be solved approximately in some cases [17, 18, 19].

One important problem is that the effective colloidal interactions are not necessarily pairwise additive, i.e. triplet or higher-order many-body potentials may appear even if the underlying interactions in and with the medium are strictly pairwise. On physical grounds, one generally expects the breakdown of pairwise additivity of the effective interactions if the typical length scale of the structures in the background is of the order of the typical colloidal length scale, e.g. the colloidal radius a. For colloid–polymer mixtures it was indeed shown that equal-sized colloids and polymers have bulk and interfacial properties that differ dramatically from predictions based on pairwise potentials [20, 21], and charged colloids in an electrolyte were shown to exhibit non-negligible effective triplet attractions on top of the pairwise repulsions [22, 23, 24] at (extremely) low salt concentrations where $\kappa^{-1} \sim a$.

In this thesis, we will study such many-body effects in suspensions of charged colloids.

1.3 Donnan equilibrium

Historically, one of the first descriptions of suspensions of charged colloids was given by Donnan in 1911 [25, 26]. This description is a very coarse-grained one, in which all particle–particle correlations are neglected, such that the system of colloids, cations and anions is approximated by an ideal-gas mixture interacting through a self-consistent electric potential

We consider a colloidal suspension of volume V and temperature T, containing N colloidal particles of charge $-Ze$, with e the proton charge, and density $n = N/V$, and we assume the suspension to be in osmotic equilibrium with a reservoir which contains monovalent positive and negative salt-ions, each with concentration c_s. Apart from the counter-ions, which are present in the system with density Zn for charge neutrality, and which are assumed to be of the same species as the positive ions in the reservoir, also some of the salt-ions from the reservoir will migrate into the suspension, giving rise to a (spatially) average concentration $\bar{\rho}_+$ of positive salt-ions (including counter-ions) and $\bar{\rho}_-$ of negative salt-ions in the suspension.

From the Boltzmann distribution, we find that the relation between the micro-ion concentrations and the average electric potential ϕ_D in the suspension is given by $\bar{\rho}_\pm = c_s \exp[\mp\phi_D]$, where the potential is fixed to $\phi_D \equiv 0$ in the salt reservoir. Furthermore, charge neutrality of the system implies that

$$\frac{Zn}{2c_s} = \frac{\bar{\rho}_+ - \bar{\rho}_-}{2c_s} = -\sinh\phi_D, \tag{1.1}$$

which defines the Donnan potential ϕ_D [25, 26, 27, 28]. Note that $\phi_D < 0$ for negatively charged colloids (i.e., $Z > 0$), and thus the total concentration of salt ions that migrated from the reservoir to the system is $\bar{\rho}_+ + \bar{\rho}_- - Zn = 2\bar{\rho}_- < 2c_s$, i.e., if colloids are added to the system, salt-ions are ejected into the reservoir. This is called the Donnan effect.

Treating the colloids and the salt-ions on the ideal gas level, the osmotic pressure Π of the suspension (defined as the difference in pressure between the system and the reservoir) is given by $\beta\Pi = n + \bar{\rho}_+ + \bar{\rho}_- - 2c_s$, where $\beta = 1/k_B T$ is the inverse temperature with k_B Boltzmann's constant. Using the Donnan relation (1.1), we find that the osmotic pressure is

$$\beta\Pi = n + 2c_s(\cosh\phi_D - 1) = n + 2c_s\left\{\sqrt{1 + \left(\frac{Zn}{2c_s}\right)^2} - 1\right\}. \tag{1.2}$$

Note that the osmotic compressibility $(\mathrm{d}\Pi/\mathrm{d}n)_{c_s}$ that follows from Eq. (1.2) is always positive, i.e., the Donnan theory does not predict a spinodal gas–liquid instability.

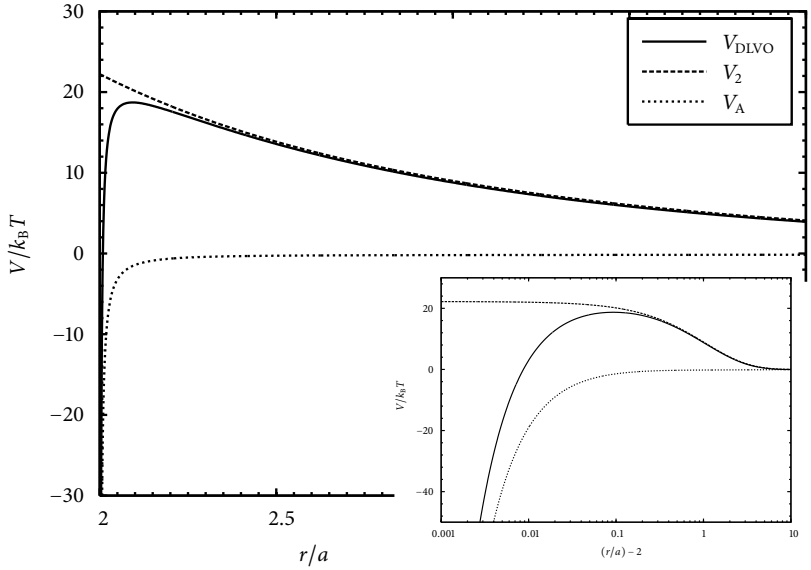

FIGURE 1.1 — The figure shows the DLVO pair-potential $V_{\text{DLVO}}(r)$, its repulsive component $V_2(r)$, and its attractive component $V_{\text{A}}(r)$ as a function of the distance r between the particle centers, for a typical colloidal particle with radius $a = 100\lambda_{\text{B}}$, charge $Z = 100$, screening constant $\kappa a = 0.5$ and Hamaker constant $A = 10^{-20}$J. The inset show the same data on a logarithmic axis. Note that the Van der Waals term $V_{\text{A}}(r)$ is extremely short ranged.

.

The Donnan approximation breaks down for strongly interacting or dense systems, but for dilute systems of lowly charged colloids, it works very well. It has, for example, been used recently to calculate the sedimentation profiles of colloidal suspensions in a gravitational or centrifugal field [29, 30, 31]. In Section 4.3.2, we compare the Donnan expression for the osmotic pressure with more advanced expressions, which do take into account interactions and correlations between the particles.

1.4 DLVO theory

In this thesis, we will focus on bulk suspensions of colloidal hard spheres carrying a (big) charge, which we assume to be homogeneously distributed on the colloidal surface. The classical theory for these systems dates back to the 1940s, when Derjaguin and Landau [32] and Verwey and Overbeek [33] independently calculated the effective potential between two identical homogeneously charged colloidal spheres (radius a, fixed total charge $-Ze$ with e the proton charge) in a bulk electrolyte medium with dielectric constant ϵ and Debye length κ^{-1}. This

DLVO potential is given by

$$V_{\text{DLVO}}(r) = \begin{cases} \infty & r < 2a; \\ V_{\text{A}}(r) + V_2(r) & r > 2a, \end{cases} \tag{1.3}$$

where $V_2(r)$ is a repulsive Yukawa potential, given by

$$V_2(r) = \frac{Z^2 e^2}{\epsilon} \left(\frac{\exp(\kappa a)}{1 + \kappa a} \right)^2 \frac{\exp(-\kappa r)}{r}, \tag{1.4}$$

and $V_A(r)$ is the (attractive) Van der Waals potential, which is given by

$$V_{\text{A}}(r) = -\frac{A}{6} \left\{ \frac{2a^2}{r^2 - 4a^2} + \frac{2a^2}{r^2} + \ln \frac{r^2 - 4a^2}{r^2} \right\}, \tag{1.5}$$

with $A > 0$ the Hamaker constant [34], which depends quadratically on the difference between the refractive indices of the particles and the background solvent [35, 36]. The screening parameter κ is defined as

$$\kappa^2 = 8\pi\lambda_{\text{B}} c_{\text{s}} \tag{1.6}$$

in the case of a 1:1 background electrolyte, consisting of monovalent, point-like cations and anions, with total ion concentration $2c_{\text{s}}$ far from the colloids, where $\lambda_{\text{B}} = \beta e^2/\epsilon$ is the Bjerrum length, $\beta = 1/k_{\text{B}}T$, and T is the temperature [32, 33]. Note that this DLVO interaction not only involves "intrinsic" colloidal properties (Z, a), but also properties of the medium (ϵ, c_{s}, T). Also note that the DLVO potential (1.3) is not valid at molecular distances from the colloidal surface, as at these length scales quantum effects become important; such effects, however, are not relevant for the theory discussed in this thesis.

In Fig. 1.1, the pair potential $V_{\text{DLVO}}(r)$ has been plotted together with its repulsive component $V_2(r)$ and the Van der Waals component $V_{\text{A}}(r)$ for a typical colloidal system. Observe the very short range of the Van der Waals contribution $V_{\text{A}}(r)$ compared to the range of the repulsive Yukawa part $V_2(r)$ of the potential. For systems with low salt concentrations, which we will be studying later on in this thesis, we will show in more detail that the pair potential (1.4) is due to a diffuse electric double-layer of counter-ions that surrounds and screens the charges on the colloidal surface. The typical thickness of this double-layer is the Debye length κ^{-1}.

As the Van der Waals contribution is very short-ranged, it is only important for very small particle separations. Because of the potential barrier of $> 10k_{\text{B}}T$ that the particles would have to overcome in the situation of Fig. 1.1, however, it is generally safe to neglect the attractive Van der Waals forces and approximate $A = 0$ in Eq. (1.3), as we will do in the remainder of this thesis. Moreover, in experimental setups, the refractive index of the solvent can be matched to the refractive index of the particles, thus reducing the Hamaker constant A and the Van der Waals forces greatly.

On the basis of Eq. (1.3) with $A = 0$, and a Hamiltonian $H = \sum_{i<j} V_2(|\mathbf{R}_i - \mathbf{R}_j|)$ of pair potentials, one can explain many experimental observations, including the crystallization of (essentially) hard spheres ($Z = 0$ or $\kappa a \gg 1$) at packing fractions $\eta = \frac{4}{3}\pi a^3 n > 0.5$ into an FCC crystal [37, 38], the crystallization into BCC crystals for sufficiently soft spheres [39, 40], the measured osmotic equation of state [41, 42], structure factor [43, 44], radial distribution function [45], pair interactions [46, 47], and many other colloidal phenomena. It is therefore fair to state that the DLVO theory as defined by Eq. (1.3) is one of the corner stones of colloid science.

1.5 Attractions?

However, not all experimental observations are in (qualitative) agreement with DLVO theory. For instance, the experimental observation of "voids" and "Swiss cheese" structures in otherwise homogeneous suspensions have been interpreted as manifestations of gas–liquid coexistence with a large density difference between the coexisting phases [48, 49], and the small lattice spacing of colloidal crystals compared to the one expected on the basis of the known density n was interpreted as evidence for gas–crystal coexistence [50]. These possibilities seemed to be confirmed by direct observations of (meta-)stable gas–crystal coexistence [51], and a (disputed) macroscopic gas–liquid meniscus [52, 53, 54], both with much larger differences in density between the two phases than predicted by DLVO theory.

Despite the ongoing debates due to a lack of experimental consensus, these experimental results, which were all obtained at low ionic strength with c_s in the μM-regime, triggered a lot of theoretical activities to find the source of cohesive energy that stabilizes the dense liquid or crystal phase in coexistence with a dilute gas phase [55]. The Van der Waals forces would be the first natural candidate to provide the cohesion, but their range and strength is generally considered to be too small to dominate over the electrostatic repulsions with a range of $\kappa^{-1} \sim 100$ nm at these low salt concentrations (see Section 1.4).

It was also found that ion–ion correlations, which are ignored in the derivation of $V_2(r)$, can lead to attractive contributions to the pair potential. However, the effect is small and too short-ranged to explain the observed phase coexistences for monovalent ions at room temperature in water [39].

Another avenue of research involves the study of the breakdown of pairwise additivity. Within Poisson–Boltzmann theory, the triplet potential was calculated, and it turned out to be attractive indeed [22], thereby suggesting that many-body interactions could be the source of cohesive energy. Phase diagrams based on repulsive pair interactions (1.3) and the attractive triplet potential indeed showed coexistence of a dilute gas with very dense crystal phases (as well as crystal–crystal coexistence) [56, 57], while experimental evidence for the breakdown of pairwise additivity was obtained by an inverse Ornstein–Zernike analysis of measured colloidal radial distribution functions [58, 59, 60], as well as by direct measurement [23, 24]. However, although pairwise additivity seems to be breaking down at low

salinity, it is yet questionable whether an approach based on the explicit calculation of triplet, quartet, quintet, and higher-order potentials, if feasible at all, is very efficient, as convergence is probably slow: there is hardly any justification to ignore the four-body potential when including the triplet potential changes the phase diagram completely compared to the pairwise case. This notion was made explicit by a recent simulation study of the primitive model (charged colloids and explicit micro-ions) that underlies the effective one-component system of Ref. [57]: the gas–crystal coexistence that was found with included triplet interactions disappeared again in the simulations of the full system [61].

An alternative approach to take into account non-pairwise interactions is based on density-dependent pair-potentials. Rather than explicitly taking into account the coordinate-dependence of higher-body potentials, the multi-body effects are smeared out and included through a state-dependent modification of the pair-potential. In the case of charged colloids, it seems natural to modify the screening constant κ of Eq. (1.6), such that not only the background (reservoir) salt concentration $2c_s$ but also the finite concentration Zn of the counter-ions and the hard-core exclusion from the colloidal volume is taken into account. For instance, one replaces κ by $\tilde{\kappa} = \sqrt{4\pi\lambda_B(2c_s + Zn)}$, $\sqrt{4\pi\lambda_B(2c_s + Zn)/(1-\eta)}$ or similar expressions [39, 62, 63, 64, 65, 66, 67, 68, 69] that reduce to κ as given by Eq. (1.6) in the dilute limit $n \to 0$. Often $\tilde{\kappa}(n) > \kappa$, and one could interpret the resulting reduction of the pairwise repulsions due to the more efficient screening at higher density as an effective attractive many-body effect.

Interestingly, however, a careful analysis of the total free energy of the suspension reveals that a density-dependent screening constant affects not only the pair-interactions but also one-body contributions, such as the free energy of each colloid within its "own" diffuse cloud of counter-ions [63, 64, 65, 66, 67, 68, 70, 71, 72]. The thickness of this double layer is typically $\tilde{\kappa}^{-1}$, and hence its typical (free) energy is of the order of $u = -(Ze)^2/\epsilon(a + \tilde{\kappa}^{-1})$, i.e. the Coulomb energy of two charges $\pm Ze$ at separation $a + \tilde{\kappa}^{-1}$. This term lowers progressively with increasing n and thus provides cohesive energy, whereas it is an irrelevant constant offset of the free energy if a constant κ is taken instead of $\tilde{\kappa}(n)$. It was shown that the density-dependence of these so-called *volume terms* could drive a gas–liquid spinodal instability at low salt concentrations [63, 65, 71, 72], and could hence (qualitatively) explain some of the puzzling experimental observations. In fact, at low-enough background salt concentrations, we have $\tilde{\kappa} = (4\pi\lambda_B Zn)^{1/2}$, and hence the self-energy per unit volume $\propto Nu/V \propto -n^{3/2}$, which is very similar to the excess free energy of 1:1-electrolytes within Debye–Hückel theory, as we will see below.

1.6 The 1:1-electrolyte

The situation in the case of 1:1-electrolytes, i.e., systems of hard spheres of diameter d with charges $\pm q$, is much clearer than the case of colloidal systems, even though colloidal suspension can be viewed as very asymmetric electrolytes. It is

well-established nowadays that such 1:1-electrolytes phase-separate if the dimensionless temperature $T^\star = \epsilon k_B T d/q^2$ is low enough (or the (symmetric) charge q is large enough).

Debye and Hückel derived in the 1920s [73], that the excess (non-ideal) free energy of such a 1:1: electrolyte, due to the ion–ion correlations in the fluid, scales like $F^{(\mathrm{exc})} \propto -V(n_+ + n_-)^{3/2}$, where $n_\pm$ are the average densities of the positive and negative ionic species, respectively [74]. The excess free energy density is negatively curved with regards to the density and can thus drive a Van der Waals loop. The theory of Debye and Hückel predicts a critical point at $T^\star = \frac{1}{16} \approx 0.063$ which is in reasonable agreement with computer simulations [75]. Extensions to Debye–Hückel theory that have been derived recently, give excellent agreement with simulations. [76, 77]

Although computer simulations and theoretical analyses have been extended to asymmetrical electrolytes with charge asymmetries up to $Z = 80$ [61, 78, 79, 80, 81], the experimental parameters for which possible phase-instabilities have been observed ($Z \sim 10^3$) are still out of reach for computer experiments, and the gap between 1:1-electrolytes and colloidal suspension has not been overcome.

We return to the relation between Debye–Hückel theory for electrolytes and volume terms for charged colloids in Chapter 5.

1.7 Charge regulation

In the discussion so far, the origin of the charge on the colloidal surface was not taken into account. Typically, the colloidal particles are uncharged in vacuum or a non-polar solvent like air, and the charge emerges because groups at the surface of the colloid can dissolve in a polar background solvent (such as water), leaving behind a charge at the colloidal surface. The colloidal charge is thus actually a dynamical quantity that may depend on system parameters like the temperature and the background ion concentrations. While the charge is often considered to be constant and fixed, this is not always the case in practise.

For example, a typical group that exists at the colloid surface is carbon hydroxide [82]. For such a particle, the colloidal charge is the result of protons dissolving into the background solvent, e.g., through the reaction

$$\mathrm{–COOH} \rightleftharpoons \mathrm{–COO^-} + \mathrm{H^+} \tag{1.7}$$

at the colloid surface. Clearly, if the proton concentration in the solution is high (i.e., the salt concentration in the reservoir is high), the chemical equilibrium will shift to the left, and the particle will discharge. Similarly, if the colloidal density is increased, the counter-ion density will increase and again the equilibrium of Eq. (1.7) shifts to the left and the colloid discharges.

This charge regulation effect should be taken into account to correctly describe a suspension of charged colloids. We return to this issue in Chapters 6 and 7.

1.8 Overview

The main topic of this thesis will be to combine Poisson–Boltzmann theory in two of its approximations: (i) a linear approximation that takes state-dependent pair-interactions and one-body terms explicitly into account at the expense of neglecting nonlinear screening effects like charge renormalization, and (ii) a cell approximation that explicitly takes into account these non-linear effect at the expense of ignoring the multi-centered nature of the systems. Furthermore, we will add charge regulation effects to this combined multi-centered, non-linear Poisson–Boltzmann theory

In Chapter 2, we review some general statistical mechanics that is relevant for integrating out the micro-ionic degrees of freedom, and we derive the traditional Poisson–Boltzmann theory. In Chapter 3, we review the cell approximation of Poisson–Boltzmann theory, and introduce the concepts of renormalized and saturated charge, originally due to Alexander [83]. In Chapter 4, we revisit the linear multi-centered approximation to Poisson–Boltzmann theory, and derive the state-dependent effective pair-potentials and volume terms in a grand-canonical setting. In Chapter 5, we develop a new theory for colloidal suspensions, combining the strengths of the cell approach of Chapter 3 and the multi-centered approach of Chapter 4. Then, in Chapter 6, we apply the concept of charge regulation to the cell model of Chapter 3, and finally in Chapter 7, we add charge regulation to the model derived in Chapter 5.

CHAPTER 2

Poisson–Boltzmann theory

2.1 Introduction

We are interested in the macroscopic properties of charged colloids, suspended in a molecular solvent with (monovalent) cations and anions. In its simplest form, the system is therefore a four-component mixture, as depicted schematically in Fig. 2.1(a). The system is in osmotic equilibrium with a salt reservoir containing cations and anions which can move freely between the system and the reservoir; the colloids, however, are contained in the system and cannot enter the reservoir. Note that the picture is not to scale, in the sense that (i) the size asymmetry between the colloids on the one hand and the ions and solvent molecules on the other hand is often much more extreme than depicted, and (ii) the density of the solvent is much higher than depicted.

In fact, for many thermodynamic purposes, the solvent can be seen as an incompressible medium, as shown in Fig. 2.1(b). In such an approach, the solvent background is generally considered to be a linear dielectric, and is only characterized by its dielectric constant ϵ. Although several studies exists which take into account finite density effects of the solvent background [84, 85], we will not take such effects into account in this thesis, for reasons of simplicity.

The next degree of coarse graining involves an average over the ionic degrees of freedom, as schematically depicted in Fig. 2.1(c). At this level, the colloidal coordinates $\{\mathbf{R}_i\}$ $(i = 1, \ldots, N)$ are still treated explicitly, but the micro-ions are represented by their density profiles $\rho_\pm(\mathbf{r}; \{\mathbf{R}_i\})$. Using the framework of Density Functional Theory (DFT), we can determine the equilibrium ionic density profiles, and calculate the effective Hamiltonian $H(\{\mathbf{R}_i\})$ of the "one-component" colloidal system. Specifically, as we will show in this chapter, the Coulomb interaction between large, charged spheres is screened by the micro-ionic species, resulting in

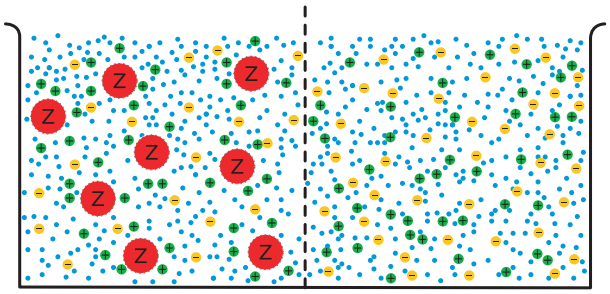

(a) Microscopic system

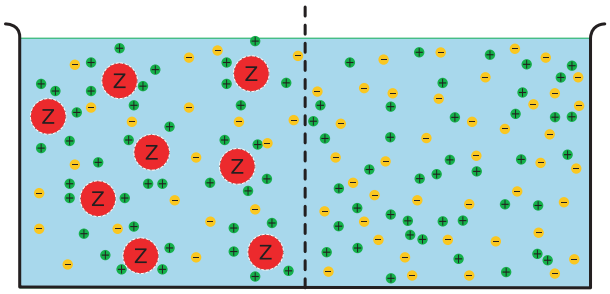

(b) Continuous solvent background

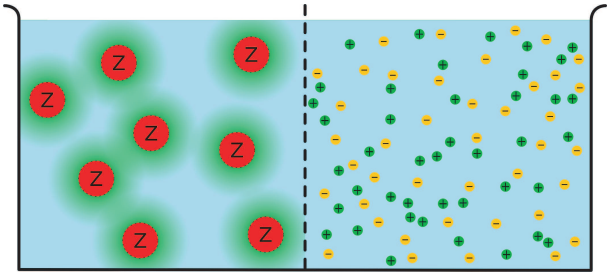

(c) Effective system of mesoscopic particles

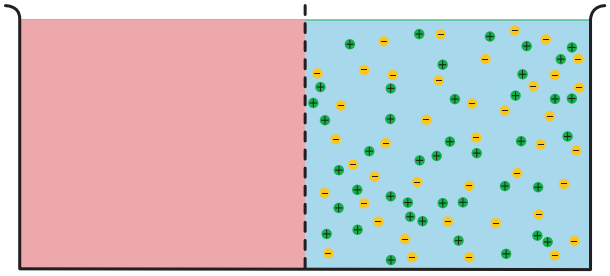

(d) macroscopic (Donnan) equilibrium

FIGURE 2.1 — A schematic overview of the different levels of approximation used to describe colloidal suspensions. Note that the particle sizes are not to scale.

an effective Yukawa potential between the particles, rather than the bare Coulomb interactions, as was discussed already in Chapter 1.

Finally, at the macroscopic level as depicted in Fig. 2.1(d), the system is characterized by the thermodynamic quantities only, e.g., by the free energy F and the osmotic pressure Π of the system as a function of the colloid density. These thermodynamic quantities can be calculated from the effective Hamiltonian $H(\{\mathbf{R}_i\})$, as we will see. Note that the Donnan theory of Section 1.3 also acts at this level of coarse graining.

In this thesis, the only interactions that we consider between the particles are hard-core and Coulomb interactions: we only take into account the hard-core interactions of the colloids (i.e., the colloids cannot overlap, and neither can the micro-ions penetrate the colloid cores) and the Coulomb interactions between the particles (i.e., micro-ion–micro-ion, micro-ion–colloid and colloid–colloid). Van der Waals attractions are neglected throughout, which is justified for most of the colloidal systems of interest here, with high charge at low salinity (see Section 1.4). We also ignore other specific effects such as hydrogen bonding, hydration shells, etc.

In this chapter, we describe the statistical mechanical background of the coarse-graining of the micro-ion degrees of freedom, i.e., the procedure how to get from the situation depicted in Fig. 2.1(b) to the situation of Fig. 2.1(c). We derive the Poisson–Boltzmann equation, which describes the electrostatic potential $\phi(\mathbf{r})$ in a mean-field approximation. We will point out the problems with the Poisson–Boltzmann equation, and we will describe our strategy for dealing with them in this thesis.

2.2 Model

We consider a suspension of volume V of N hard, spherical colloids of radius a, mass m, fixed charge $-Ze$, which is distributed homogeneously over the surface, and density $n = N/V$ in a continuous background solvent, which is characterized by the Bjerrum length $\lambda_B = e^2/\epsilon k_B T$, with $-e$ the electron charge, ϵ the dielectric constant of the solvent, k_B Boltzmann's constant and T the temperature. The system is also assumed to contain N_+ positive and N_- negative monovalent, point-like salt-ions.

Charge neutrality dictates that $N_+ = N_- + ZN$. The total interaction Hamiltonian of the system can be written as

$$\mathcal{H} = \mathcal{H}_{cc} + \mathcal{H}_{cs} + \mathcal{H}_{ss}, \tag{2.1}$$

where the bare colloid–colloid Hamiltonian $\mathcal{H}_{cc}$, the colloid–salt Hamiltonian $\mathcal{H}_{cs}$, and the salt–salt Hamiltonian $\mathcal{H}_{ss}$ are pairwise sums of hard-core and (unscreened)

Coulomb potentials. We write $\mathcal{H}_{cc} = \sum_{i<j}^{N} V_{cc}(R_{ij})$ with

$$\beta V_{cc}(r) = \begin{cases} \infty & r < 2a; \\ \dfrac{Z^2 \lambda_B}{r} & r > 2a, \end{cases} \tag{2.2}$$

and $\mathcal{H}_{cs} = \mathcal{H}_{c+} + \mathcal{H}_{c-}$ with $\mathcal{H}_{c\pm} = \sum_{i=1}^{N} \sum_{j=1}^{N_\pm} V_{c\pm}(|\mathbf{R}_i - \mathbf{r}_j^\pm|)$, where

$$\beta V_{c\pm}(r) = \begin{cases} \infty & r < a; \\ \mp \dfrac{Z \lambda_B}{r} & r > a, \end{cases} \tag{2.3}$$

where $\mathbf{r}_j^\pm$ is the position of the jth positive (negative) micro-ion. The expression for $\mathcal{H}_{ss}$ is similar, but contains no hard-core terms because of the point-like nature of the ions.

2.3 A grand-canonical approach

In principle, the thermodynamic properties of this system could be calculated from the Helmholtz free energy of the system $\mathcal{F}(N, N_-, V, T)$, which is defined by the relation $\exp(-\beta\mathcal{F}) = \mathrm{tr_c tr_+ tr_-} \exp(-\beta\mathcal{H})$. Note that one can ignore the explicit N_+ dependence of $\mathcal{F}$ because of the charge neutrality condition. The classical canonical trace of the colloid degrees of freedom is defined as

$$\mathrm{tr_c}(\ldots) = \frac{1}{N! \mathcal{V}^N} \int_V \mathrm{d}\mathbf{R}^N (\ldots), \tag{2.4}$$

where $\mathcal{V}$ is an irrelevant constant volume, accounting for the kinetic energy and the internal partition function of the colloid, and likewise we define the traces $\mathrm{tr_+}$ and $\mathrm{tr_-}$ over the degrees of freedom of the positive and negative salt-ions, respectively.

This canonical formulation of the free energy has some drawbacks, the main ones being that the numerical work in the canonical ensemble for these systems is more involved than in a grand-canonical approach, and that in experimental work on the systems of interest, the suspension is often in diffusive equilibrium with a reservoir. We therefore prefer to treat the anions and cations grand-canonically.

We thus assume the suspension to be in diffusive contact with a (dilute) reservoir of monovalent anions and cations at chemical potential $\mu_\pm = k_B T \ln(c_s \Lambda_\pm^3)$, where $2c_s$ is the total ion density in the (charge neutral) reservoir, and where $\Lambda_\pm$ is the thermal De Broglie wavelength of the cations (+) and anions (−), respectively. The colloidal particles cannot enter the ion reservoir (for example, because of a semi-permeable membrane in an actual experimental setting), and remain treated canonically (fixed N and V) as before. The thermodynamic potential of this ensemble, which we will call the "Donnan-ensemble", is denoted by $F = \mathcal{F} - \mu_+ N_+ - \mu_- N_-$, and is a function of the variables N, V, T, and $\mu_\pm$. It is related to the microscopic Hamiltonian $\mathcal{H}$ by the "Donnan partition function"

$$\exp(-\beta F) = \mathrm{tr_c\, Tr_+\, Tr_-}\, \exp(-\beta\mathcal{H}), \tag{2.5}$$

where $\mathcal{H}$ was defined in Eq. (2.1) and the grand canonical traces are defined as

$$\mathrm{Tr}_\pm(\ldots) = \sum_{N_\pm=0}^{\infty} \exp(\beta\mu_\pm N_\pm)\mathrm{tr}_\pm(\ldots) = \sum_{N_\pm=0}^{\infty} \frac{{c_\mathrm{s}}^{N_\pm}}{N_\pm!} \int \mathrm{d}\mathbf{r}_\pm^{N_\pm}(\ldots). \tag{2.6}$$

Here we have used that $\exp(\beta\mu_\pm)/\Lambda_\pm^3 = c_\mathrm{s}$ (where the factor $1/\Lambda_\pm^3$ follows from the classical momentum integration), and we denoted the micro-ion coordinates by $\mathbf{r}_\pm^{N_\pm}$. For convenience we will drop the explicit T-dependence from now on, and we replace $\mu_\pm$ by the reservoir concentration c_s.

Even though our main objective is to calculate $F(N, V, c_\mathrm{s})$ as defined in Eq. (2.5), we will first focus on an important and convenient intermediate entity the effective Hamiltonian H, which depends on the colloid configuration $\{\mathbf{R}\}$ and parametrically on the reservoir salt concentration c_s. It is defined as

$$\begin{aligned} \exp(-\beta H) =& \mathrm{Tr}_+\,\mathrm{Tr}_-\,\exp(-\beta\mathcal{H}) \\ =& \exp(-\beta\mathcal{H}_\mathrm{cc})\mathrm{Tr}_+\,\mathrm{Tr}_-\,\exp(-\beta\mathcal{H}_\mathrm{cs} - \beta\mathcal{H}_\mathrm{ss}) \\ \equiv& \exp(-\beta\mathcal{H}_\mathrm{cc})\exp(-\beta\Omega), \end{aligned} \tag{2.7}$$

where, in the last step, we defined the grand partition function $\exp(-\beta\Omega)$ of the *inhomogeneous* system of interacting cations and anions (through $\mathcal{H}_\mathrm{ss}$) in the external potential of the colloidal particles at positions $\{\mathbf{R}_i\}$ (through $\mathcal{H}_\mathrm{cs}$). The corresponding grand potential of this system is Ω, which is the quantity that we need to calculate in order to find the effective Hamiltonian given from Eq. (2.7) as

$$H = \mathcal{H}_\mathrm{cc} + \Omega. \tag{2.8}$$

Once H is known, we can use standard one-component techniques to obtain approximate expressions for F, since $\exp(-\beta F) = \mathrm{tr}_\mathrm{c}\exp(-\beta H)$ is precisely the Helmholtz free energy of a one-component system with Hamiltonian H.

Once the free energy F is known, thermodynamic properties of the system can be calculated. Because of the extensive character of F we can write $F(N, V, c_\mathrm{s}) = Vf(n, c_\mathrm{s})$, and the thermodynamic properties follow then as $\mu = (\partial F/\partial N) = (\partial f/\partial n)$ and $P = -(\partial F/\partial V) = n\mu - f$, where the derivatives are to be taken at fixed c_s and T. Phase-coexistence is determined by chemical and mechanical equilibrium between the two phases, i.e., the chemical potential of the cations, the chemical potential of the anions and the pressure must be equal in the two phases. Because of the grand-canonical nature of the theory presented here, however, the salt-ions in both phases are already in equilibrium with the salt reservoir, and thus the phase-coexistence conditions simplify to the *two* conditions

$$\begin{cases} P(n^{(1)}, c_\mathrm{s}) &= P(n^{(2)}, c_\mathrm{s}); \\ \mu(n^{(1)}, c_\mathrm{s}) &= \mu(n^{(2)}, c_\mathrm{s}), \end{cases} \tag{2.9}$$

for the *two* unknown coexisting colloid densities $n^{(i)}$, at fixed c_s. This is a considerable reduction of the numerical effort compared to the work that is needed

to calculate phase equilibria in the canonical ensemble, where a system of three equations with three unknowns has to be solved [72]. Note that the mechanical equilibrium condition is equivalent to equal osmotic pressure Π in the two coexisting phases, where $\Pi(n, c_s) = P(n, c_s) - P(0, c_s)$ is the suspension's excess pressure over the reservoir pressure $P(0, c_s) = 2c_s k_B T$. This simple relation allows for a rather direct comparison to experimental measurements of the osmotic pressure, as we will show below.

2.4 The Poisson–Boltzmann equation

The task at hand is to find an explicit expression for the grand potential $\Omega(\{\mathbf{R}_i\})$ of the colloidal system. We employ Density Functional Theory (DFT), according to which the grand potential may be determined as the minimum of a suitable functional [86, 87]. It turns out be be more convenient to include the direct colloid–colloid interactions right away, and thus calculate the effective Hamiltonian (2.8) directly rather than the grand potential $\Omega(\{\mathbf{R}_i\})$. Taking into account only Coulombic and hard-core interactions between the different species, the effective Hamiltonian can, in mean-field approximation, be written as

$$\begin{aligned}\beta H(\{\mathbf{R}_i\}) = &\sum_{\alpha=\pm} \int \mathrm{d}\mathbf{r}\, \rho_\alpha(\mathbf{r}) \left[\ln \frac{\rho_\alpha(\mathbf{r})}{c_s} - 1 \right] \\ &+ \frac{1}{2} \int \mathrm{d}\mathbf{r}\, \left[\rho_+(\mathbf{r}) - \rho_-(\mathbf{r}) + q(\mathbf{r})\right] \phi(\mathbf{r}) \\ &+ \sum_{\alpha=\pm} \int \mathrm{d}\mathbf{r}\, \rho_\alpha(\mathbf{r}) \beta U_\alpha^{\mathrm{HC}}(\mathbf{r}),\end{aligned} \tag{2.10}$$

where $\rho_+(\mathbf{r})$ and $\rho_-(\mathbf{r})$ denote the (yet unknown) concentrations of positive and negative salt-ions, respectively, and H (and Ω) is now to be interpreted as a functional of these densities. the hard-core potentials of the colloids is denoted by $\beta U_\pm^{\mathrm{HC}}(\mathbf{r})$ and is infinite inside the hard cores, and vanishes elsewhere. The charge on the colloids is distributed homogeneously over the surface, and is supposed to be fixed (i.e., polarization effects are neglected). The colloidal charge distribution is thus given by

$$q(\mathbf{r}) = \sum_{i=1}^{N} \frac{-Z}{4\pi a^2} \delta(|\mathbf{r} - \mathbf{R}_i| - a). \tag{2.11}$$

The first term of Eq. (2.10) describes the entropy of the micro-ions. The chemical potential, describing the diffusive equilibrium with the reservoir, is here taken into account implicitly through the relation $\beta\mu_s = \ln[c_s \Lambda \pm^3]$, which holds in the reservoir. The second term of Eq. (2.10) describes the Coulombic interactions in the system; the (dimensionless) electric potential $\phi(\mathbf{r})$ is defined as

$$\phi(\mathbf{r}) = \lambda_B \int \mathrm{d}\mathbf{r}'\, \frac{\rho_+(\mathbf{r}') - \rho_-(\mathbf{r}') + q(\mathbf{r}')}{|\mathbf{r} - \mathbf{r}'|}. \tag{2.12}$$

The potential $\phi(\mathbf{r})$ is fixed such that $\phi(\mathbf{r}) \equiv 0$ in the reservoir (where $\rho_+(\mathbf{r}) = \rho_-(\mathbf{r}) \equiv c_s$ and $q(\mathbf{r}) \equiv 0$). The final term of the functional (2.10) takes into account the exclusion of the micro-ionic species from the hard cores of the colloids. Any other contribution to the grand potential (2.10) is due to ion–ion correlations, which are not very important for dilute systems with monovalent ions at room temperature [17], and which we will ignore here.

The definition (2.12) of the electric potential can also be written in differential form, which leads to Poisson's equation

$$\nabla^2\phi(\mathbf{r}) = -4\pi\lambda_B\left[\rho_+(\mathbf{r}) - \rho_-(\mathbf{r}) + q(\mathbf{r})\right]. \tag{2.13}$$

The equilibrium salt-ion concentrations $\rho_\pm(\mathbf{r})$ can be found by minimization of the functional Eq. (2.10) [86, 87]. The minimum condition of this functional with respect to the ionic density profiles $\rho_\pm(\mathbf{r})$ is given by

$$0 \equiv \frac{\delta\beta\Omega}{\delta\rho_\pm(\mathbf{r})} = \frac{\delta\beta H}{\delta\rho_\pm(\mathbf{r})} = \ln\frac{\rho_\pm(\mathbf{r})}{c_s} \pm \phi(\mathbf{r}) + \beta U_\pm^{\mathrm{HC}}(\mathbf{r}), \tag{2.14}$$

which is Boltzmann's relation $\rho_\pm(\mathbf{r}) = c_s \exp[\mp\phi(\mathbf{r})]$ outside the hard cores and $\rho_\pm(\mathbf{r}) \equiv 0$ inside the hard cores. Combining the two relations (2.13) and (2.14), we recover the usual non-linear Poisson–Boltzmann equation

$$\nabla^2\phi(\mathbf{r}) = \kappa^2 \sinh\phi(\mathbf{r}) \qquad \mathbf{r} \text{ outside cores} \tag{2.15a}$$

$$\mathbf{n}_i \cdot \nabla\phi(\mathbf{r}) = Z\lambda_B/a^2 \qquad \mathbf{r} = \mathbf{R}_i + a\mathbf{n}_i, \tag{2.15b}$$

where $\mathbf{n}_i$ denotes the normal to the surface of colloid i. The parameter κ denotes the inverse Debye length in the reservoir, and is given by $\kappa^2 = 8\pi\lambda_B c_s$.

In principle, the electric potential $\phi(\mathbf{r})$ is completely determined by the boundary value problem (2.15a)–(2.15b) alone, together with the choice $\phi(\mathbf{r}) \equiv 0$ in the reservoir. From the solution $\phi(\mathbf{r})$, one obtains the equilibrium density profiles, and by insertion of those into Eq. (2.10) one finds, in principle at least, the grand potential needed in Eq. (2.8). However, due to the combination of the nonlinear character of the differential equation (2.15a) and the multi-centered geometry of the boundary conditions (2.15b), this boundary value problem is extremely difficult, and computationally very expensive, to solve: extremely fine or spatially inhomogeneous grids are needed to deal with the large gradients close to the spherical colloidal surfaces, while simultaneously the space between the colloids must be covered adequately to describe the colloid–colloid interactions properly. Although some studies of this type exist they do not cover large parts of parameter space because of the computational costs involved [88, 89, 90, 91].

2.5 Approximations to the Poisson–Boltzmann equation

As an alternative to solving the full, non-linear problem (2.15a)–(2.15b), several approximation schemes have been devised over the years. These can be divided into

two broad classes: (i) linear Poisson–Boltzmann theory (LPB), and (ii) Wigner-Seitz cell theory (WSC).

2.5.1 Linear Poisson–Boltzmann theory

In linear Poisson–Boltzmann theory, the multi-centered boundary (2.15b) condition is left unchanged, while $\sinh\phi(\mathbf{r})$ in Eq. (2.15a) is linearized as $\sinh\tilde{\phi}+(\phi(\mathbf{r})-\tilde{\phi})\cosh\tilde{\phi}$ with $\tilde{\phi}$ a spatial constant. The resulting multi-centered equation can be solved analytically, as will be shown in more detail in Chapter 4. If one sets $\tilde{\phi}\equiv 0$, one finds essentially $H=\sum_{i<j}^{N}V_2(R_{ij};\kappa,Z)$ with the pair potential given by

$$\beta V_2(R;\kappa,Z)=\left(\frac{Z\exp(\kappa a)}{1+\kappa a}\right)^2\lambda_{\mathrm{B}}\frac{\exp(-\kappa r)}{r}, \tag{2.16}$$

the electrostatic part of the traditional Derjaguin–Landau–Verwey–Overbeek (or DLVO) potential [32, 33]. This Hamiltonian does *not* predict a spinodal instability at low salinity as it contains only repulsions and no cohesive terms. If one chooses to set $\tilde{\phi}$ equal to the Donnan potential ϕ_{D} as defined in Section 1.3 (i.e., the volume average of $\phi(\mathbf{r})$), then one finds the effective Hamiltonian $H=\Phi(N,V,\tilde{\kappa})+\sum_{i<j}^{N}V_2(R_{ij};\tilde{\kappa},Z)$, where $\tilde{\kappa}=\kappa\sqrt{\cosh\tilde{\phi}}$ and $\Phi(N,V,\tilde{\kappa})$ are the so-called volume terms, which describe the self-energy of the colloids in their own clouds of counter-ions. This version of the linear Poisson–Boltzmann theory does predict gas–liquid and gas–solid coexistence of systems of highly charged colloids at low salinity, and may therefore explain some of the surprising experimental results. However, the parameter regime where these transitions are being predicted is such that $Z\lambda_{\mathrm{B}}/a\gtrsim 10$, and for such high charges the linear approximation is inappropriate as will be shown later on.

2.5.2 The Poisson–Boltzmann cell model

In the Wigner–Seitz-cell approaches, on the other hand, the nonlinear character of the problem (2.15a) is retained at the expense of replacing the multi-centered boundary condition (2.15b) by a radially symmetric problem with one colloid in the center. In Alexander's original work the cell radius R was taken such that the cell volume equals the volume per colloid in the system, i.e. $R=a(\eta_{\max}/\eta)^{1/3}$, with $\eta_{\max}\approx 0.74$ the packing fraction of a densely packed crystal and Eq. (2.15a) was solved with the boundary conditions $\phi'(a)=Z\lambda_{\mathrm{B}}/a^2$ and $\phi'(R)=0$ such that the cell is charge-neutral [83, 92]. In the more recent jellium-like versions of this theory, the cell extends to infinity and the Poisson–Boltzmann equation $\nabla^2\phi(\mathbf{r})=\kappa^2\sinh\phi(r)-4\pi\lambda_{\mathrm{B}}Zn$ is solved with boundary conditions $\phi'(a)=-Z\lambda_{\mathrm{B}}/a^2$ and $\phi'(\infty)=0$, i.e. the other (non-central) colloids are represented by their average density [93, 94]. In all of these central-symmetric approaches the concept of a renormalized charge Z^* (and an effective screening constant κ^*) appears naturally from the decay of $\phi(r)$ close to the cell boundary. It is then *presumed* that

the colloid–colloid Hamiltonian in the state-point of interest is a pairwise sum of $V_2(R_{ij};\kappa^*,Z^*)$, while the cell is actually charge neutral or contains the other colloids already. Although density-dependent repulsive pair interactions may give rise to a gas–liquid spinodal [62], these have not been predicted on the basis of the Wigner–Seitz-cell and jellium theories.

The Poisson–Boltzmann cell model will be further discussed in Chapter 3.

2.6 Conclusion

In this chapter, we have identified two effects that are important in the study of suspensions of charged colloids with Poisson–Boltzmann theory:

1. many-body effects such as volume terms and state-dependent pair interactions in multi-centered solution of the Poisson–Boltzmann equation;
2. charge renormalization and non-linear effects in the Poisson–Boltzmann cell model;

The many-body effects will be further discussed in Chapter 4, and the nonlinear charge renormalization effects in Chapter 3.

CHAPTER 3

Wigner–Seitz cell Poisson–Boltzmann theory

Abstract

We briefly review the Poisson–Boltzmann cell model as introduced by Alexander and others in Ref. [83] in 1984. We describe its main features, derive the expression for Alexander charge renormalization and show the effective charge and the saturated effective charge as a function of the system parameters.

3.1 Model

We consider a suspension of N spherical colloidal particles of radius a and charge $-Ze$, with $-e$ the electron charge. The background solvent, typically water, ethanol, or a similar medium, is treated as a continuous dielectric background, characterized by the Bjerrum length $\lambda_B = e^2/\epsilon k_B T$, where ϵ is the dielectric constant of the solvent, k_B is Boltzmann's constant and T is the temperature. The system is assumed to be in thermal and diffusive equilibrium with a reservoir which contains monovalent, ionic salt pairs with pair density c_s, giving rise to (yet unknown) densities $\rho_\pm(\mathbf{r})$ of salt ions inside the system.

As argued in the previous chapter, the system is completely described by the (dimensionless) electric potential $\phi(\mathbf{r})$, which we define to be equal to zero in the salt reservoir. In the previous chapter, we have derived the Poisson–Boltzmann equation

$$\nabla^2\phi(\mathbf{r}) = \kappa^2 \sinh[\phi(\mathbf{r})]; \tag{3.1a}$$

$$\mathbf{n}_i \cdot \nabla\phi(\mathbf{r}) = Z\lambda_B/a^2, \quad (\mathbf{r} = \mathbf{R}_i + a\mathbf{n}_i), \tag{3.1b}$$

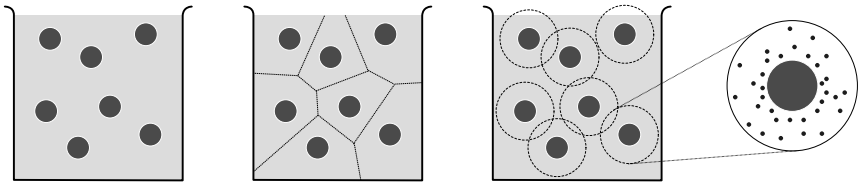

FIGURE 3.1 — The different stages in the cell approximation of a colloidal suspension: the colloids in suspension (a) are inside their Wigner–Seitz cells (b). The Wigner–Seitz cells are approximated by spherical cells (c), each of which is treated independently (d).

where $\kappa^{-1} = (8\pi\lambda_B c_s)^{1/2}$ is the Debye length in the reservoir.

Solving Eq. (3.1a) with the boundary conditions of a fixed electric field at the colloid surfaces leads to a solution $\phi(\mathbf{r})$, for which the mean-field effective Hamiltonian $H(\{\mathbf{R}_i\})$ of Eq. (2.7) follows. In practice, however, obtaining this solution is extremely difficult, because of the combination of the complicated multi-centered boundary conditions and the non-linear character of the differential equation. To overcome this problem, the system is commonly divided into (charge neutral) Wigner–Seitz cells, which are then approximated to be identical and spherically symmetric (see Fig. 3.1), reducing the hard problem (3.1a) to a one-dimensional non-linear boundary value problem

$$\frac{1}{r^2}\frac{\partial}{\partial r}\left[r^2\frac{\partial}{\partial r}\phi_c(r)\right] = \kappa^2 \sinh[\phi_c(r)], \tag{3.2a}$$

$$\phi_c'(a) = Z\lambda_B/a^2; \quad \phi_c'(R) = 0 \tag{3.2b}$$

where we have denoted the potential in the cell by $\phi_c(r)$. We denote the radius of the cell by R, such that $R = a(\eta_{max}/\eta)^{1/3}$, with $\eta_{max} \approx 0.74$ the packing fraction of a closely packed crystal. This boundary value problem is easy to solve numerically on a grid.

A typical solution for colloids of radius $a = 100\lambda_B$, charge $Z = 1000$ at screening constant $\kappa a = 3$ and density $\eta = 0.093$ (i.e., cell radius $R = 2a$), is shown in Fig. 3.2. In the top figure, the electric potential $\phi(r)$ is shown as a function of the coordinate inside the cell. Note that the derivative at the cell boundary $r = R$ is indeed equal to zero, expressing the charge-neutrality of the cell. The derivative at the colloid surface is determined by the colloid charge Z. The bottom figure shows the micro-ionic densities, as determined from Boltzmann's equation $\rho_\pm(\mathbf{r}) = c_s \exp[\mp\phi(\mathbf{r})]$, corresponding to the same solution. The solid line shows the density of positive ions (i.e., counter-ions plus positive salt-ions), the dotted line show the density of negative micro-ions, and the dotted-dashed line denotes the charge density $\rho(r) = \rho_+(r) - \rho_-(r)$.

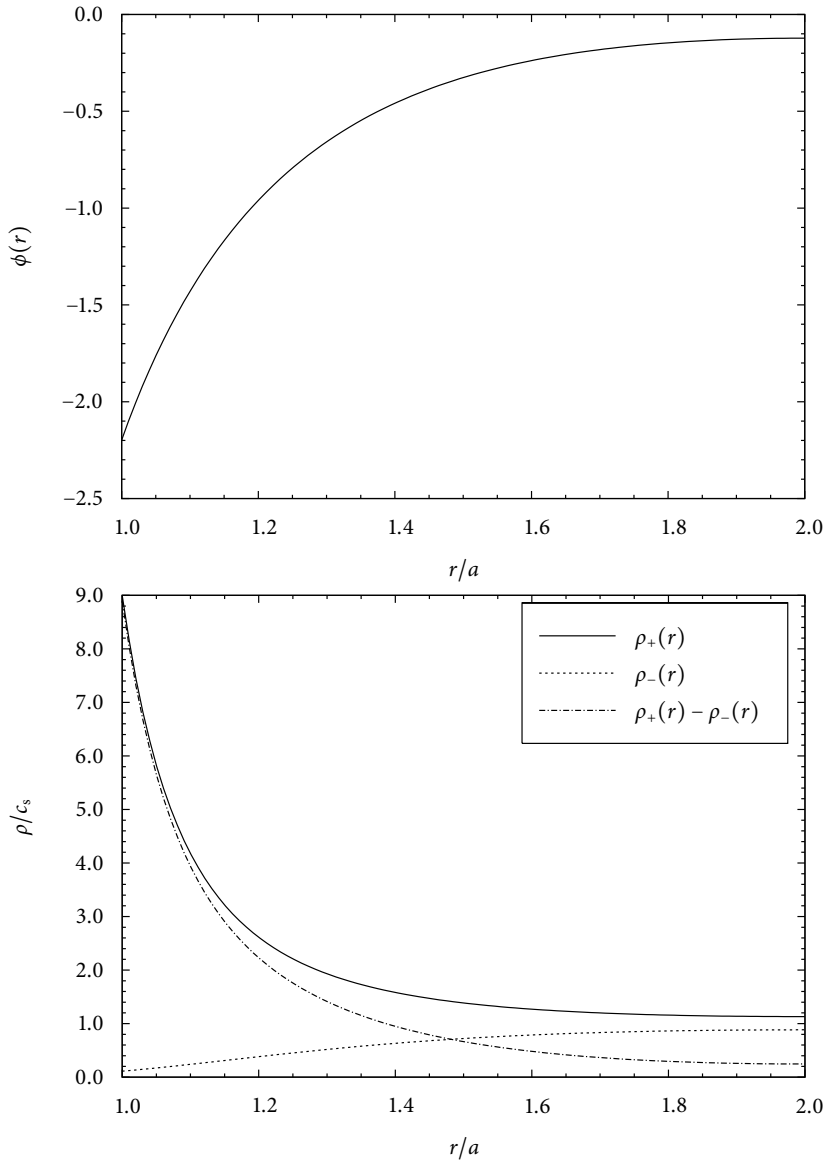

FIGURE 3.2 — A typical solution of the cell boundary value problem (3.2a)–(3.2b) for $\kappa a = 3$, $a/\lambda_B = 100$, $R/a = 2$ and $Z = 1000$. The top figure shows the potential $\phi(r)$, the bottom figure shows the micro-ion densities $\rho_\pm(r)$ and the charge density $\rho(r)$.

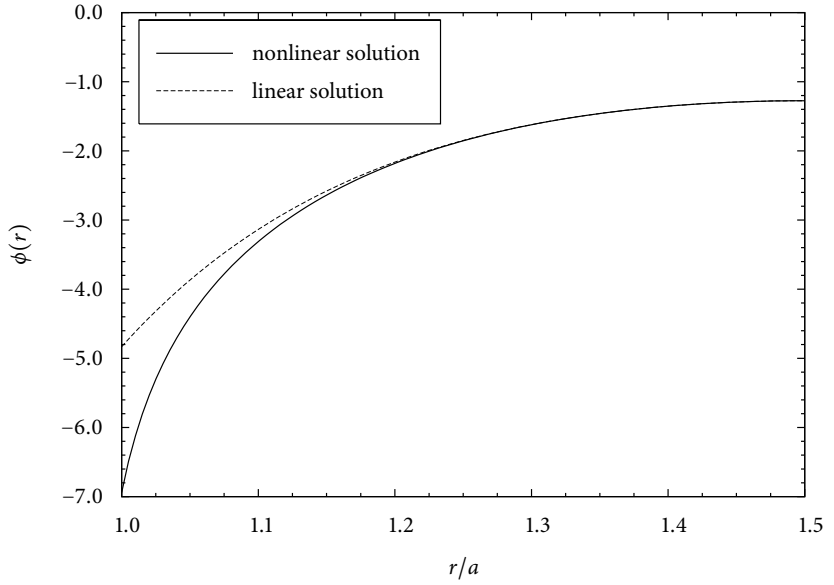

FIGURE 3.3 — The (dimensionless) electric potential $\phi(r)$ for a system with $\kappa a = 3$, $a/\lambda_B = 100$, $R/a = 1.5$ and $Z = 10000$. The solid line show the nonlinear solution, while the dashed line shows the linear solution that matches at the cell boundary. The effective charge is determined by the derivative of the potential at the colloid surface, and is given by $Z^\star = 2201$.

3.2 Effective charge

Far away from the colloidal surface, near the cell boundary, the potential is reasonably flat. Therefore, in this part of the cell, it is allowed to linearize the Poisson–Boltzmann equation (3.2a). Denoting the linearization point by $\tilde{\phi}$ and the linearized solution by $\phi_\ell^{\text{cell}}(r)$, the linearized Poisson–Boltzmann equation is given by

$$\frac{1}{r^2}\frac{\partial}{\partial r}\left[r^2\frac{\partial}{\partial r}[\phi_\ell^{\text{cell}}(r)-\tilde{\phi}]\right] = \tilde{\kappa}^2\left\{\tanh[\tilde{\phi}] - (\phi_\ell^{\text{cell}}(r)-\tilde{\phi})\right\}, \tag{3.3}$$

where $\tilde{\kappa}^2 = \kappa^2\cosh\tilde{\phi}$. We choose the linearization point equal to the potential at the cell boundary: $\tilde{\phi} = \phi_\ell^{\text{cell}}(R) = 0$. The general solution of Eq. (3.3) is given by

$$\phi_\ell^{\text{cell}}(r) = \tilde{\phi} + \tanh[\tilde{\phi}]\left(\nu_+\frac{\lambda_B}{r}e^{\tilde{\kappa}(r-R)} + \nu_-\frac{\lambda_B}{r}e^{-\tilde{\kappa}(r-R)} - 1\right) \tag{3.4}$$

The coefficients $\nu_\pm$ can be determined from the boundary conditions. If we match the linearized potential $\phi_\ell^{\text{cell}}(r)$ at the cell boundary to the full nonlinear solution $\phi_c(r)$, i.e., if we demand $\phi_\ell^{\text{cell}}(R) = \tilde{\phi} = \phi_c(R)$ and $\phi_\ell^{\text{cell}\prime}(R) = \phi_c'(R)$, we find that

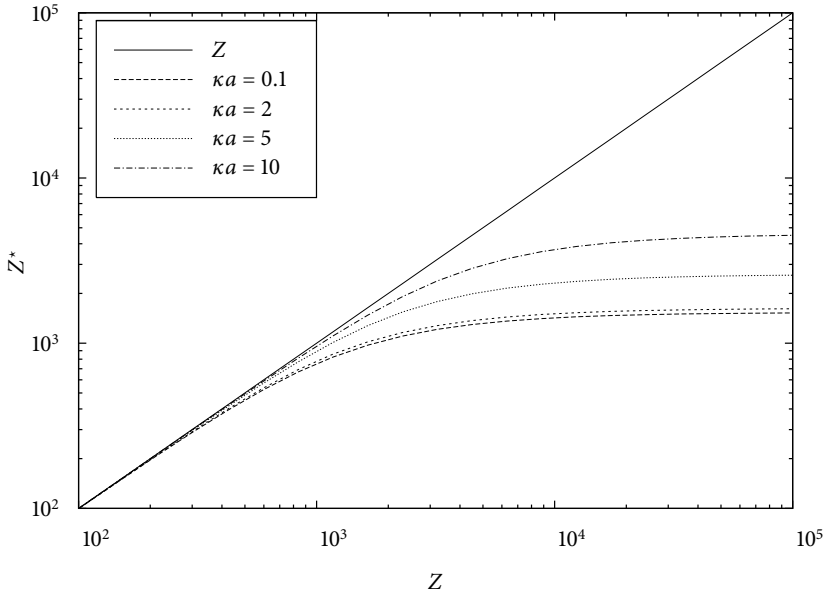

FIGURE 3.4 — The effective charge $Z^\star$ as a function of the bare charge Z for different values of κa. The colloid radii are kept fixed at $a = 100\lambda_B$ and the density is $\eta = 0.1$.

the coefficients are given by

$$\nu_\pm = \frac{\tilde{\kappa}R \pm 1}{2\tilde{\kappa}\lambda_B}, \tag{3.5}$$

fully fixing the linear Poisson–Boltzmann solution (3.4).

In Fig. 3.3, the electric potential $\phi_c(r)$ is plotted for a typical system with charge $Z = 10^4$, colloid radius $a = 100\lambda_B$, and screening constant $\kappa a = 3$. Also plotted is the solution of the linearized Poisson–Boltzmann equation (3.3) for the same system. From this figure, it is clear that, except for the region very close to the colloid surface, the linear solution is indeed a good approximation. This is generally true and therefore it makes sense to define an effective charge $Z^\star$ based on the derivative of the linear solution at the colloidal surface, i.e., $\phi_\ell^{\text{cell}\,\prime}(a) \equiv Z^\star\lambda_B/a^2$. This concept was first introduced by Alexander in Ref. [83]; a more recent review can be found in Ref. [92].

As the linear solution $\phi_\ell^{\text{cell}}(r)$ is known explicitly from Eqs. (3.4) and (3.5), is is straightforward to find an explicit expression for the effective charge $Z^\star$. This

leads to the following expression for $Z^\star$

$$Z^\star = -\frac{\tanh\frac{\tilde{\phi}}{4}}{\tilde{\kappa}\lambda_B}\Big\{(\tilde{\kappa}^2 aR - 1)\sinh[\tilde{\kappa}(R-a)] + \tilde{\kappa}(R-a)\cosh[\tilde{\kappa}(R-a)]\Big\}, \tag{3.6}$$

which was derived in this closed form by Trizac in Ref. [92]. As this effective charge $Z^\star$ governs the behavior of the potential in the outer part of the cells, it is assumed to also determine the pair interaction between two colloids at sufficient distance from each other (see Refs. [83, 92]). We will substantiate this assumption in Chapter 5.

The behavior of the effective charge $Z^\star$ as a function of the bare charge Z is plotted in Fig. 3.4 for a typical colloidal system. Clearly it can be seen that the two charges Z and $Z^\star$ are equal for low Z, as is to be expected from the observation that the linearization (3.3) is a very good approximation for low colloidal charges. At higher charges, starting from approximately $Z\lambda_B/a \gtrsim 10$, the charge renormalization becomes important. Note specifically that at a high bare charge, the effective charge becomes independent of the bare charge and converges to a *saturated charge* $Z^\star_{\text{sat}}$.

This saturated charge is plotted in Fig. 3.5 as a function of the screening κa and the packing fraction η. Note that the saturated charge increases with both the screening and the colloid density. Recently, Trizac and Bocquet and others have derived that the saturated charge is determined by the condition [95, 96]

$$|\phi_\ell^{\text{cell}}(R) - \phi_\ell^{\text{cell}}(a)| \approx 4. \tag{3.7}$$

This observation immediately explains the increase of the saturated charge with κa and η: if the screening κa increases and the decay of the potential between the colloidal surface and the cell boundary must stay constant as prescribed by Eq. (3.7), that means that electric field (i.e., the derivative of the potential) at the colloid surface must increase. Likewise, if the cell radius decreases while still the condition (3.7) must hold, the potential must decay faster for the cell to stay charge-neutral, and thus the derivative at the colloid surface should increase.

3.3 Effective Hamiltonian and free energy

The effective Hamiltonian was defined in Eq. (2.10). Neglecting explicit interparticle interaction and focussing on the cell interiors, where $\beta U_\pm(\mathbf{r}) \equiv 0$ only, the effective Hamiltonian for the cell model is approximated as

$$H(\{\mathbf{R}_i\}) \approx N\Omega_{\text{WSC}}, \tag{3.8}$$

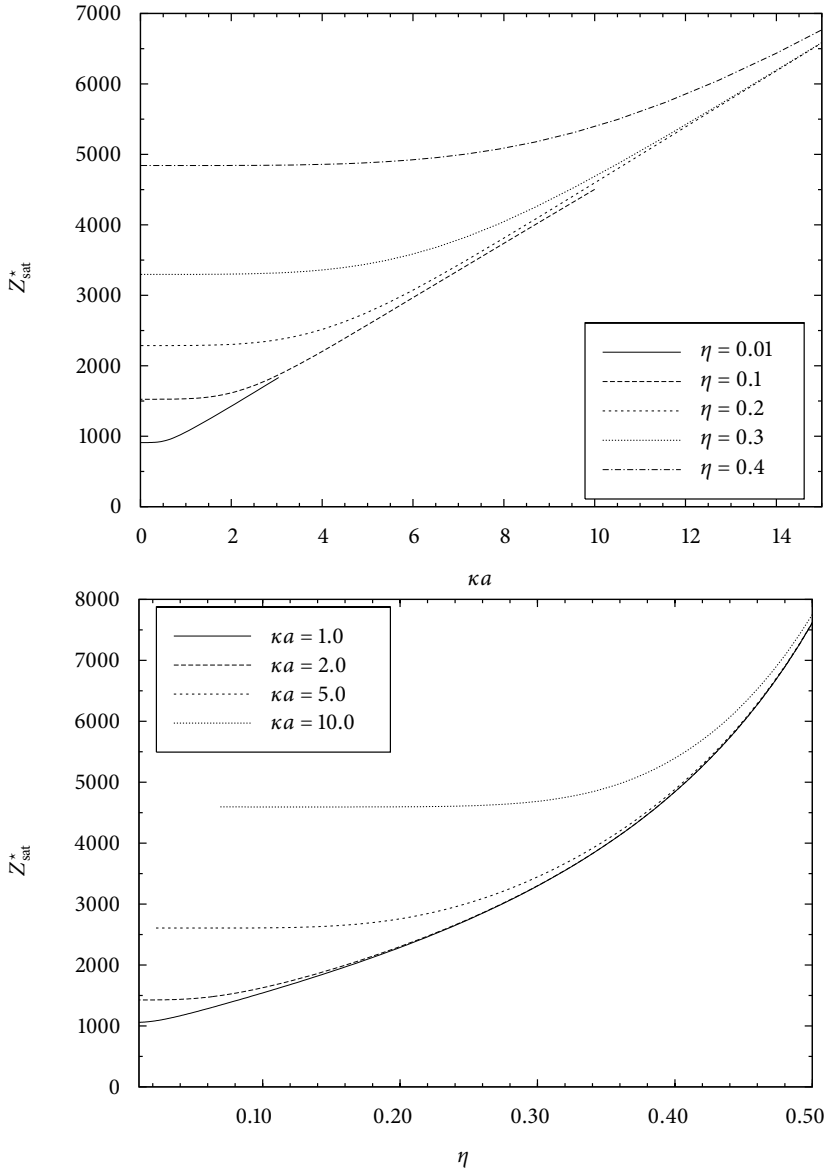

FIGURE 3.5 — The saturated effective charge $Z^{\star}_{\mathrm{sat}}$ as a function of κa (top) and η (bottom). The colloid radii are kept fixed at $a = 100\lambda_{\mathrm{B}}$.

where Ω_{WSC} is the internal grand potential of an individual cell, which does no longer depend on the colloid coordinates $\{\mathbf{R}_i\}$. It is given by (cf. Eq. (2.10)

$$\begin{aligned}\beta\Omega[\rho_\pm(r)] = \sum_{\alpha=\pm}\int_{\text{cell}} \mathrm{d}\mathbf{r}\,\rho_\alpha(r)\left[\ln\frac{\rho_\alpha(r)}{c_\text{s}} - 1\right] \\ + \frac{1}{2}\int_{\text{cell}}\mathrm{d}\mathbf{r}\,\left[\rho_+(r) - \rho_-(r) + q(r)\right]\phi(r),\end{aligned} \tag{3.9}$$

where the integration are now over the interior of a single cell. This first term of Eq. (3.9) denotes the entropy of the micro-ions in the system; note that the diffusive equilibrium of the salt-ions with the reservoir has been taken into account here by inserting the chemical potential $\mu_{\pm,\text{res}} = k_\text{B}T\ln[c_\text{s}\Lambda_\pm]$, with $\Lambda_\pm$ the thermal wavelength of the positive and negative ions. The second term of the functional (3.9) denotes the electrostatic interactions between the constituents of the cell. The charge of the colloids is given by $q(r) = -(Z/4\pi a^2)\delta(r-a)$, and the (dimensionless) electric potential in the cell was defined in Eq. (2.12).

By exploiting Poisson's and Boltzmann's equations, the cell grand potential of Eq. (3.9) can be written in the form

$$\begin{aligned}\beta\Omega_{\text{WSC}} &= \sum_{\alpha=\pm} 4\pi\int_a^R \mathrm{d}r\,r^2\left\{\rho_\alpha(r)\left(\ln\left[\frac{\rho_\alpha(r)}{c_\text{s}}\right]-1\right) + \frac{[\phi_\text{c}'(r)]^2}{2\lambda_\text{B}}\right\} \\ &= -\frac{Z}{2}\phi(a) + 4\pi c_\text{s}\int_a^R \mathrm{d}r\,r^2\left\{\phi_\text{c}(r)\sinh\phi_\text{c}(r) - 2\cosh\phi(r)\right\},\end{aligned} \tag{3.10}$$

See for example Ref. [97] for a rigorous derivation of this grand potential. From the effective Hamiltonian (3.8), we calculate the free energy F of the cell model, which takes the simple form $F = F_{\text{id}} + N\Omega_{\text{WSC}}$. From the free energy, the osmotic pressure $\Pi = -(\mathrm{d}F)/(\mathrm{d}V)$ and the inverse osmotic compressibility $\chi^{-1} = (\mathrm{d}\Pi)/(\mathrm{d}n)$ (and other thermodynamic quantities) can be calculated.

The free energy F as determined from Eq. (3.10) is a convex function of the colloid density n, and therefore $\chi > 0$ and no spinodal instabilities are possible in the Poisson–Boltzmann cell model. Many studies have been performed on the phase behavior in the Poisson–Boltzmann cell model [97, 98, 99], and it is generally agreed upon that, for the reason cited above, no gas–liquid coexistence is possible in the cell model.

3.4 Conclusion

In this chapter, we have given a brief review of the Poisson–Boltzmann cell model. The Poisson–Boltzmann equation was solved inside a spherically symmetric cell, and we defined the Alexander effective charge. The Poisson–Boltzmann cell model does not give rise to any spinodal instability.

CHAPTER 4

Volume terms for charged colloids: a grand-canonical treatment

Abstract

We present a study of thermodynamic properties of suspensions of charged colloids on the basis of linear Poisson–Boltzmann theory. We calculate the effective Hamiltonian of the colloids by integrating out the ionic degrees of freedom grand-canonically. This procedure not only yields the well-known pairwise screened-Coulomb interaction between the colloids, but also additional volume terms which affect the phase behavior and the thermodynamic properties such as the osmotic pressure. These calculations are greatly facilitated by the grand-canonical character of our treatment of the ions, and allow for relatively fast computations compared to earlier studies in the canonical ensemble. Moreover, the present derivation of the volume terms are relatively simple, make a direct connection with Donnan equilibrium, yield an explicit expression for the effective screening constant, and allow for extensions to include, for instance, nonlinear effects.

4.1 Introduction

In this chapter we will focus on a description of effective interactions (or the effective Hamiltonian) in bulk suspensions of charged colloids within linear Poisson–Boltzmann theory. As we will see below, and already touched upon in Chapter 1, these linear Poisson–Boltzmann theories result in density-dependent pair interactions and volume terms.

In the past few years, many studies haven been performed of this linear theory [63, 65, 71, 72]. There are, however, several reasons to revisit these studies. First of all, they are often formulated in the canonical ensemble (fixed ion concentrations), which not only obscures its close relationship with the classical Donnan theory for colloidal suspensions [27, 100], but also unnecessarily complicates the numerical calculation of phase diagrams.

Moreover, and more importantly, the derivation of the explicit expressions for the total free energy was perhaps not very transparent in Refs. [71, 72], and may have hindered extensions of the theory to include, for instance, charge renormalization or regulation. This nonlinear effect was first studied in a cell geometry [83], and, more recently, in a jellium-like model [93, 94]. In both of those models, the nonlinear character of the theory is retained, while its complicated multi-centered nature is replaced by a radially symmetric structure. The effective colloidal charge Z^* that appears in the prefactor of the DLVO repulsions, is then reduced from its bare value Z due to a tightly adsorbed layer of counter-ions in the vicinity of the colloidal surface. This effect is important when $Z\lambda_B/a \gg 1$ [83, 92, 96, 99, 101], and therefore casts serious doubt [98] on the predictions of the gas–liquid and gas–crystal transitions in e.g. Refs. [63, 71, 72] since large values of Z were needed to have the transitions [94, 97]. If one now realizes that Z^* depends on n and $\tilde{\kappa}(n)$, as was shown in e.g. Ref. [92], it is easy to imagine that the volume terms are affected non-trivially by charge renormalization similarly as by the n-dependence of the screening parameter. It is therefore important to be able to include this effect into volume-term-type theories, and hence to reformulate these theories as transparently as possible.

In order to be able to address all these issues, we revisit the purely linear screening theory with volume terms in this chapter. Its nonlinear extension to include charge renormalization will be discussed in Chapter 5. The present chapter is organized as follows. In section 4.2 we calculate H by minimizing the mean-field grand potential functional of the ions, whereby explicit expression for the density-dependent screening parameter, the Donnan potential, and the Donnan effect are obtained as intermediate results. In section 4.3 we consider the thermodynamics of the suspension, in particular the free energy and the osmotic pressure, with a few interesting canceling contributions. In section 4.4 we calculate a few phase diagrams. We conclude and summarize in section 4.5.

It turns out, as we will show in this chapter, that at least some of these shortcomings and drawbacks of working in the canonical ensemble can be lifted by treating the anions and cations grand-canonically.

4.2 The grand potential Ω

In this section, we calculate the grand potential Ω as defined in Eqs. (2.7) and (2.8). Although the general structure of the linear theory is similar to that of the gen-

eral Poisson–Boltzmann theory of Chapter 2, we rewrite the expression (2.10) in a slightly different form in the current chapter for reasons of convenience.

4.2.1 Density functional

We consider a suspension of N hard, spherical colloids of radius a, mass m, fixed charge $-Ze$ and density $n = N/V$ in a continuous background solvent, which is characterized by the Bjerrum length $\lambda_B = e^2/k_B T$, with $-e$ the electron charge, k_B Boltzmann's constant and T the temperature. The system is in diffusive equilibrium with a salt reservoir of inverse temperature $\beta = 1/k_B T$; the reservoir contains monovalent, point-like salt ions with pair density c_s. This gives rise to (yet to be determined) concentrations $\rho_\pm(\mathbf{r})$ of positive and negative ions in the suspension.

The cations and anions experience external potentials $U_+(\mathbf{r})$ and $U_-(\mathbf{r})$, respectively, due to the Coulomb and excluded volume interactions with a fixed configuration $\{\mathbf{R}\}$ of colloidal particles. These potentials are explicitly given by

$$U_\pm(\mathbf{r}) = \sum_{i=1}^{N} V_{c\pm}(|\mathbf{R}_i - \mathbf{r}|) \tag{4.1}$$

where the colloid–ion pair potentials $V_{c\pm}(r)$ were defined in Eq. (2.3). We can now write the grand-potential functional within a simple mean-field approximation as

$$\begin{aligned} \Omega[\rho_+, \rho_-] &= \Omega_{id}[\rho_+] + \Omega_{id}[\rho_-] + \frac{e^2}{2\epsilon} \int d\mathbf{r} d\mathbf{r}' \, \frac{\rho(\mathbf{r})\rho(\mathbf{r}')}{|\mathbf{r} - \mathbf{r}'|} \\ &+ \int d\mathbf{r} \Big(\rho_+(\mathbf{r}) U_+(\mathbf{r}) + \rho_-(\mathbf{r}) U_-(\mathbf{r}) \Big), \end{aligned} \tag{4.2}$$

where we defined the ion charge density $\rho(\mathbf{r}) = \rho_+(\mathbf{r}) - \rho_-(\mathbf{r})$, and where the ideal-gas grand potential functional can be written as

$$\begin{aligned} \Omega_{id}[\rho_\pm] &= \int d\mathbf{r} \, \rho_\pm(\mathbf{r}) \Big(-\mu_\pm + k_B T \big(\ln \rho_\pm(\mathbf{r}) \Lambda_\pm^3 - 1 \big) \Big) \\ &= k_B T \int d\mathbf{r} \, \rho_\pm(\mathbf{r}) \Big(\ln \frac{\rho_\pm(\mathbf{r})}{c_s} - 1 \Big). \end{aligned} \tag{4.3}$$

Here we have substituted the identity $\mu_\pm = k_B T \ln c_s \Lambda_\pm^3$.

The Euler–Lagrange equations $\delta\Omega/\delta\rho_\pm(\mathbf{r}) = 0$ that follow from Eq. (4.2), can be cast, for $\mathbf{r}$ outside a colloidal hard core, into the form $\rho_\pm(\mathbf{r}) = c_s \exp[\mp\phi(\mathbf{r})]$. The dimensionless potential $\phi(\mathbf{r})$ must then satisfy the nonlinear multi-centered Poisson–Boltzmann equation [102]

$$\nabla^2 \phi(\mathbf{r}) = \kappa^2 \sinh \phi(\mathbf{r}) - \frac{Z\lambda_B}{a^2} \sum_{i=1}^{N} \delta(|\mathbf{r} - \mathbf{R}_i| - a), \tag{4.4}$$

where $\delta(r)$ is the Dirac-delta. Unfortunately, no analytical solution to Eq. (4.4) is known for the multi-centered geometry of interest here. Even solving Eq. (4.4)

numerically is far from trivial, and requires a serious computational effort [88, 89, 90, 91, 103, 104].

For this reason we will first make further approximations to the functional, and then perform its minimization afterwards. The main approximation involves the expansion, up to quadratic order, of the ideal-gas grand potential terms about the, as of yet unknown, ion densities $\bar{\rho}_\pm$, such that $\rho_\pm(\mathbf{r}) - \bar{\rho}_\pm$ are considered to be the "small" expansion parameters. This expansion yields $\Omega_{\mathrm{id}}[\rho_\pm] \approx \Omega'_{\mathrm{id}}[\rho_\pm]$ with

$$\begin{aligned}\beta\Omega'_{\mathrm{id}}[\rho_\pm] &= \bar{\rho}_\pm\Big(\ln\frac{\bar{\rho}_\pm}{c_{\mathrm{s}}} - 1\Big)V + \ln\frac{\bar{\rho}_\pm}{c_{\mathrm{s}}}\int \mathrm{d}\mathbf{r}\,\big(\rho_\pm(\mathbf{r}) - \bar{\rho}_\pm\big) \\ &+ \frac{1}{2\bar{\rho}_\pm}\int \mathrm{d}\mathbf{r}\,\big(\rho_\pm(\mathbf{r}) - \bar{\rho}_\pm\big)^2. \end{aligned} \tag{4.5}$$

In principle, this expansion holds for arbitrary $\bar{\rho}_\pm$, but later on we will choose $\bar{\rho}_\pm$ to be equal to the average ion concentrations in the system, such that $\int \mathrm{d}\mathbf{r}\,(\rho_\pm(\mathbf{r}) - \bar{\rho}_\pm) = 0$, i.e. $V\bar{\rho}_\pm = N_\pm$ is the number of ions in the suspension. As will be shown below, this linearization corresponds to a linearization of Eq. (4.4) about $\phi(\mathbf{r}) = \bar{\phi}$ with $\bar{\phi}$ the Donnan potential. This is in line with Ref. [105].

It turns out to be convenient, and necessary, to rewrite the external potentials $U_\pm(\mathbf{r})$ for the ions such that $U_\pm(\mathbf{r}) = \pm V(\mathbf{r}) + W(\mathbf{r})$, where we defined the electrostatic potential (due to the colloids) $V(\mathbf{r}) = \sum_i v(|\mathbf{r} - \mathbf{R}_i|)$ and the hard-core potential $W(\mathbf{r}) = \sum_i w(|\mathbf{r} - \mathbf{R}_i|)$, with

$$\beta v(r) = \begin{cases} \beta v_0 & r < a; \\ -Z\lambda_{\mathrm{B}}/r & r > a, \end{cases} \tag{4.6a}$$

and

$$\beta w(r) = \begin{cases} \beta w_0 & r < a; \\ 0 & r > a. \end{cases} \tag{4.6b}$$

Although in an exact theory the hard-core parameters βv_0 and βw_0 would be infinite, we approximate them by finite values in the current theory. As we will show below, these finite values are necessary and sufficient to ensure, within the linearized theory, a vanishing ion density in the colloidal hard cores.

Collecting the results we can write the approximate grand-potential functional as

$$\begin{aligned}\Omega[\rho_+,\rho_-] &= \Omega'_{\mathrm{id}}[\rho_+] + \Omega'_{\mathrm{id}}[\rho_-] + \frac{e^2}{2\epsilon}\int \mathrm{d}\mathbf{r}\mathrm{d}\mathbf{r}'\,\frac{\rho(\mathbf{r})\rho(\mathbf{r}')}{|\mathbf{r}-\mathbf{r}'|} \\ &+ \int \mathrm{d}\mathbf{r}\,\Big\{\rho(\mathbf{r})V(\mathbf{r}) + \big(\rho_+(\mathbf{r}) + \rho_-(\mathbf{r})\big)W(\mathbf{r})\Big\}, \end{aligned} \tag{4.7}$$

which is minimized by those (equilibrium) profiles that satisfy the Euler–Lagrange equations

$$\ln\frac{\bar{\rho}_\pm}{c_{\mathrm{s}}} + \frac{\rho_\pm(\mathbf{r}) - \bar{\rho}_\pm}{\bar{\rho}_\pm} \pm \phi(\mathbf{r}) + \beta W(\mathbf{r}) = 0. \tag{4.8}$$

Here we introduced the (dimensionless) electrostatic potential $\phi(\mathbf{r})$, given by

$$\phi(\mathbf{r}) = \lambda_B \int d\mathbf{r}' \, \frac{\rho(\mathbf{r}')}{|\mathbf{r} - \mathbf{r}'|} + \beta V(\mathbf{r}). \tag{4.9}$$

4.2.2 Equilibrium profiles and Donnan equilibrium

We leave the hard-core parameters v_0 and w_0 undetermined for now, and start the analysis of the Euler–Lagrange equations by integrating Eq. (4.8) over the volume. At the same time, we impose that $\int d\mathbf{r} \, [\rho_\pm(\mathbf{r}) - \bar{\rho}_\pm] = 0$, i.e. we choose $\bar{\rho}_\pm$ such that it is the actual average ion density in the suspension. After rearrangement, we find that

$$\bar{\rho}_\pm = c_s \exp[\mp\bar{\phi} - \eta\beta w_0], \tag{4.10}$$

where $\bar{\phi} = \int d\mathbf{r} \, \phi(\mathbf{r})/V$ is the spatially averaged electric potential, i.e. the Donnan potential. Since global charge neutrality imposes that $\bar{\rho}_+ - \bar{\rho}_- = Zn$, we can conclude from Eq. (4.10) that the Donnan potential satisfies

$$\sinh\bar{\phi} = -\frac{Zn}{2c_s} \exp[\eta\beta w_0], \tag{4.11}$$

which reduces to the usual Donnan expressions in the point-colloid limit $\eta \to 0$ (see Section 1.3 and Refs. [27, 106]). Combining Eq. (4.11) with (4.10) yields

$$\bar{\rho}_\pm = \tfrac{1}{2}\left(\sqrt{(Zn)^2 + (2c_s)^2 \exp(-2\eta\beta w_0)} \pm Zn\right), \tag{4.12}$$

which explicitly relates the salt concentration in the suspension to the colloid density and the salt reservoir concentration, provided the parameter w_0 is known.

Using these relations for $\bar{\phi}$ and $\bar{\rho}_\pm$ we consider two specific linear combinations of the Euler–Lagrange equations, and rewrite Eqs. (4.8) as

$$\frac{\rho_+(\mathbf{r})}{\bar{\rho}_+} + \frac{\rho_-(\mathbf{r})}{\bar{\rho}_-} - 2 = -2\,(\beta W(\mathbf{r}) - \eta\beta w_0)\,; \tag{4.13a}$$

$$\begin{aligned}\rho(\mathbf{r}) - \bar{\rho} = &-(\bar{\rho}_+ + \bar{\rho}_-)(\phi(\mathbf{r}) - \bar{\phi}) \\ &- \bar{\rho}\,(\beta W(\mathbf{r}) - \eta\beta w_0)\,,\end{aligned} \tag{4.13b}$$

where we defined the short-hand notation $\bar{\rho} = \bar{\rho}_+ - \bar{\rho}_- = Zn$ for the overall ionic charge density. This particular linear combination was chosen, because (i) the charge density is the physical quantity of interest here, and (ii) the electric potential is decoupled from the "charge-neutral" density.

It is straightforward to solve the "hard-core" linear combination, Eq. (4.13a). Imposing that $\rho_+(\mathbf{r})/\bar{\rho}_+ + \rho_-(\mathbf{r})/\bar{\rho}_- \equiv 0$ within the hard-core of any of the colloids (i.e. wherever $W(\mathbf{r}) = w_0$) yields a value for the hard-core parameter,

$$\beta w_0 = \frac{1}{1-\eta}, \tag{4.14}$$

whereas outside any of the colloidal hard core positions we have

$$\frac{\rho_+(\mathbf{r})}{\bar{\rho}_+} + \frac{\rho_-(\mathbf{r})}{\bar{\rho}_-} = \frac{2}{1-\eta}. \tag{4.15}$$

The solution of the "charge" linear combination, Eq. (4.13b), is most straightforwardly found by Fourier transformation. For an arbitrary function $f(\mathbf{r})$ we define and denote the Fourier transform as $f_{\mathbf{k}} = \int \mathrm{d}\mathbf{r}\, f(\mathbf{r}) \exp(i\mathbf{k}\cdot\mathbf{r})$. One easily checks from equation (4.13b) that

$$\begin{aligned}\rho_{\mathbf{k}} =& (2\pi)^3 \left\{\bar{\rho} + (\bar{\rho}_+ + \bar{\rho}_-)\bar{\phi} + \bar{\rho}\eta\beta w_0\right\}\delta(\mathbf{k}) \\ & - (\bar{\rho}_+ + \bar{\rho}_-)\phi_{\mathbf{k}} - \bar{\rho} W_{\mathbf{k}},\end{aligned} \tag{4.16}$$

where we have from Eq. (4.6b) that

$$W_{\mathbf{k}} = \frac{4\pi a w_0}{k^2}\left(\frac{\sin(ka)}{ka} - \cos(ka)\right)\sum_{j=1}^{N} e^{i\mathbf{k}\cdot\mathbf{R}_j}, \tag{4.17}$$

and from Eqs. (4.9) and (4.6a) that

$$\begin{aligned}\phi_{\mathbf{k}} =& 4\pi\lambda_{\mathrm{B}}\frac{\rho_{\mathbf{k}}}{k^2} - \frac{4\pi a}{k^2}\sum_{j=1}^{N}\exp(i\mathbf{k}\cdot\mathbf{R}_j) \\ & \times\left\{\left(\beta v_0 + Z\frac{\lambda_{\mathrm{B}}}{a}\right)\cos ka - \beta v_0\frac{\sin ka}{ka}\right\}.\end{aligned} \tag{4.18}$$

Equations (4.16) and (4.18) are two linear equations in the unknowns $\phi_{\mathbf{k}}$ and $\rho_{\mathbf{k}}$, which can be solved straightforwardly. Fixing the remaining hard-core parameter v_0 to

$$\beta v_0 = -Z\frac{\bar{\kappa}\lambda_{\mathrm{B}}}{1+\bar{\kappa}a} + \beta w_0\frac{\bar{\rho}_+ - \bar{\rho}_-}{\bar{\rho}_+ + \bar{\rho}_-}, \tag{4.19}$$

we find that the charge density is given by

$$\begin{aligned}\rho_{\mathbf{k}} =& (2\pi)^3\left\{\frac{\bar{\rho}}{1-\eta} + (\bar{\rho}_+ + \bar{\rho}_-)\bar{\phi}\right\}\frac{k^2}{k^2+\bar{\kappa}^2}\delta(\mathbf{k}) \\ & + \frac{Z}{1+\bar{\kappa}a}\frac{\cos ka + \frac{\bar{\kappa}}{k}\sin ka}{1+k^2/\bar{\kappa}^2}\sum_j e^{i\mathbf{k}\cdot\mathbf{R}_j},\end{aligned} \tag{4.20}$$

where the effective Debye screening parameter is defined as

$$\begin{aligned}\bar{\kappa} \equiv& \sqrt{4\pi\lambda_{\mathrm{B}}(\bar{\rho}_+ + \bar{\rho}_-)} \\ =& \sqrt{4\pi\lambda_B}\left\{(Zn)^2 + (2c_s\exp[-\eta/(1-\eta)])^2\right\}^{1/4}.\end{aligned} \tag{4.21}$$

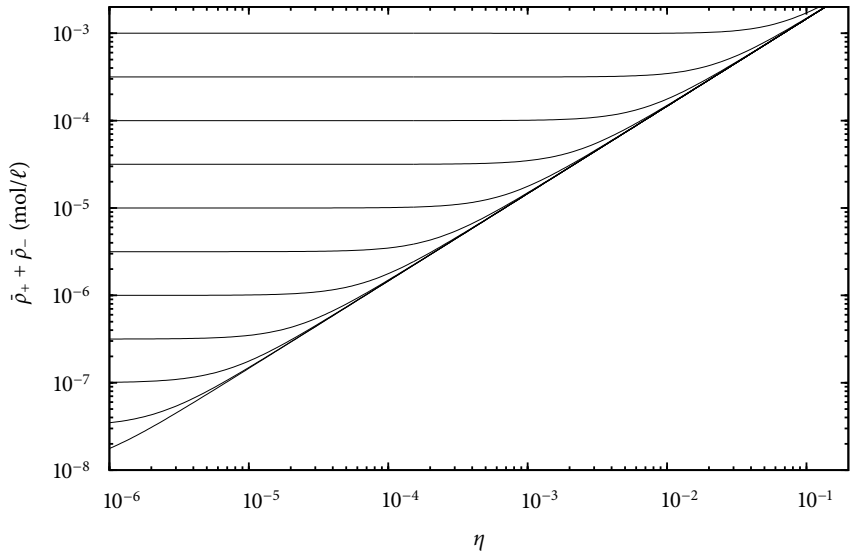

(a)

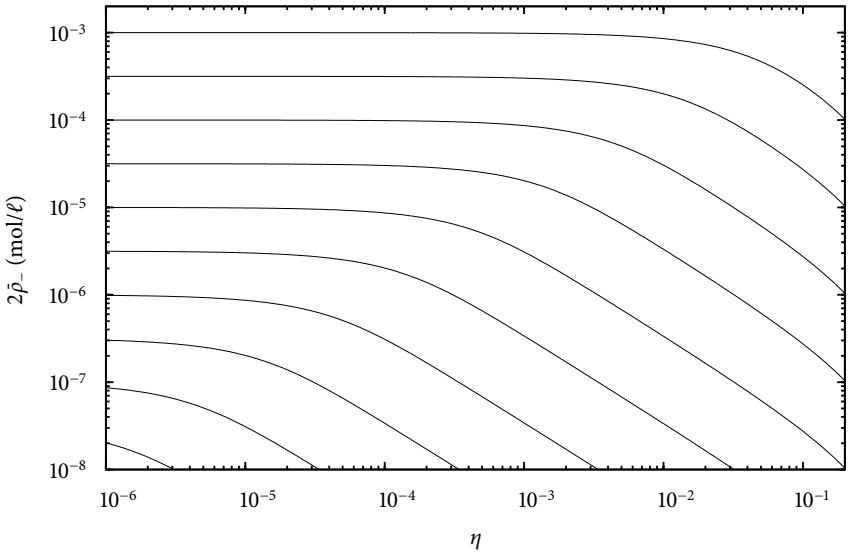

(b)

FIGURE 4.1 — Total ion concentration $\bar{\rho}_+ + \bar{\rho}_-$ (a) and concentration of added salt $\bar{\rho}_-$ (b) as a function of the colloid packing fraction for different reservoir concentrations, using the expressions of Eq. (4.12) and (4.14). The colloidal charge and radius are $Z = 50$ and $a = 21.9$nm, respectively, and the solvent is ethanol at room temperature such that $\lambda_B = 2.37$nm. This matches the parameters from the experiments by Raşa et al [31]. The asymptote in the top figure matches the $Zn \gg c_s$ limit $\bar{\rho}_+ + \bar{\rho}_- \to Zn$ of Eq. (4.12).

Here we used Eqs. (4.11), (4.12), and (4.14) in rewriting the first into the second line. Note that the factor $\exp[-\eta/(1-\eta)]$ that appears in Eq. (4.21) can be accurately represented by $(1-\eta)$, with a relative deviation less than 0.01 for $\eta < 0.1$ and less than 0.1 for $\eta < 0.35$.

The first term in expression (4.20) is of the form $\propto k^2\delta(\mathbf{k})$ and does *not* contribute to the charge density (4.22). It does, however, contribute to the electric potential $\phi(\mathbf{r})$ though the first term of Eq. (4.18), as we will see below.

The real space representation of the charge density is a multi-centered sum $\rho(\mathbf{r}) = \sum_i \rho_1(|\mathbf{r}-\mathbf{R}_i|)$, where the one-particle density profiles (the "orbitals") have the usual DLVO form [32, 33]:

$$\rho_1(r) = \begin{cases} 0 & r < a; \\ \dfrac{Z\bar{\kappa}^2}{4\pi}\dfrac{\exp(\bar{\kappa}a)}{1+\bar{\kappa}a}\dfrac{\exp(-\bar{\kappa}r)}{r} & r > a. \end{cases} \tag{4.22}$$

We note that the vanishing of $\rho_1(r)$ inside the colloidal hard core is a direct consequence of our particular choice for v_0 given by Eq. (4.19); other choices for v_0 would have yielded a finite ion charge density inside the hard core. Note also that the multi-centered charge density $\rho(\mathbf{r})$ is *not* vanishing within the hard cores, since the exponential tail of the orbital centered around colloid i penetrates the hard core of all the other colloids $j \neq i$.

By inserting Eq. (4.14) into (4.12), explicit expressions for the average concentrations $\bar{\rho}_\pm$ of ions in the suspension are obtained as a function of the colloid density n, colloid charge Z, and the reservoir concentration $2c_s$ — this was already used to obtain Eq. (4.21). These expressions reduce, in the limit of point-like colloids (for which $\eta = 0$) to the standard expressions for the Donnan effect [27, 100].

This effect is illustrated in Fig. 4.1, where we plot the total ion concentration $\bar{\rho}_+ + \bar{\rho}_-$ in (a), and the concentration of added salt $2\bar{\rho}_- = \bar{\rho}_+ + \bar{\rho}_- - Zn$ in (b), on the basis of our expressions for $\bar{\rho}_\pm$. The parameters are close to those of the experiments by Raşa et al. [31, 107]: $Z = 50$, $\lambda_B = 2.37$nm, and $a = 21.9$nm (ethanol). The reservoir salt concentration equals the $\eta = 0$ limit of each of the curves, and the crossover from the low-η plateau to the high-η linear part corresponds to the crossover from added-salt dominance to counter-ion dominance. Note the expulsion of added salt back into the reservoir at high η in (b). An important aspect of these intermediate results is that the screening parameter $\bar{\kappa}$ *increases* with n essentially $\propto \sqrt{Zn}$ in the counter-ion-dominated regime (which may occur at packing fractions as low as $\eta \simeq 10^{-4}$ if $c_s \simeq 3\mu$M).

As we have now solved the Euler–Lagrange equations (4.8) for the two linear combinations $\rho_+(\mathbf{r})/\bar{\rho}_+ + \rho_-(\mathbf{r})/\bar{\rho}_-$ and $\rho_+(\mathbf{r}) - \rho_-(\mathbf{r})$, it is straightforward to disentangle the equilibrium profiles and obtain the profiles $\rho_\pm(\mathbf{r})$ of the two ionic species separately.

It is important to realize, however, that these results depend on the particular choice that we have made for the hard-core potentials in Eqs. (4.6a) and (4.6b).

Different choices for these hard-core potentials lead to other, non-equivalent minima of the grand-potential. For instance, instead of $U_\pm(\mathbf{r}) = \pm V(\mathbf{r}) + W(\mathbf{r})$, we could have considered the choice $U_\pm(\mathbf{r}) = \pm V(\mathbf{r}) + 2\bar{\rho}_\mp W(\mathbf{r})/(\bar{\rho}_+ + \bar{\rho}_-)$, which, with $\beta v_0 = -Z\bar{\kappa}\lambda_B/(1+\bar{\kappa}a)$ and $\beta w_0 = 1/(1-\eta)$ would lead to a vanishing $\rho_1(r)$ and $\rho_+(\mathbf{r})/\bar{\rho}_+ + \rho_-(\mathbf{r})/\bar{\rho}_-$ inside the hard cores. This choice was actually made in Refs. [71, 72], and leads to similar, but not identical results for the effective Hamiltonian — see Appendix A.2.

4.2.3 The minimum of the functional

In Appendix A.1, we derive the equilibrium grand potential Ω by insertion of our solution of the Euler–Lagrange equations (4.13a) and (4.13b) into the functional (4.2). The effective interaction Hamiltonian $H = \mathcal{H}_{cc} + \Omega$ then takes the form

$$H(\{\mathbf{R}\}, N, V, c_s) = \Phi(V, n, c_s) + \sum_{i<j}^{N} V_2'(R_{ij}; n, c_s). \tag{4.23}$$

The first term Φ, is independent of the colloidal coordinates $\mathbf{R}_i$, and is called the "volume term" as it is a density-dependent, extensive thermodynamic quantity that scales with the volume of the system. The second term of Eq. (4.23) is a pairwise sum that does depend on the colloidal coordinates (and on the density n). For later convenience we decompose the volume term as $\Phi = \Phi_D + \Phi_0$, with the so-called "Donnan" term defined by

$$\frac{\beta\Phi_D}{V} = \sum_\pm \bar{\rho}_\pm \left(\ln\frac{\bar{\rho}_\pm}{c_s} - 1\right), \tag{4.24}$$

and the other term by

$$\frac{\beta\Phi_0}{V} = -\frac{1}{2}\frac{(Zn)^2}{\bar{\rho}_+ + \bar{\rho}_-} + \frac{\eta}{1-\eta}\frac{2\bar{\rho}_+\bar{\rho}_-}{\bar{\rho}_+ + \bar{\rho}_-} - \frac{n}{2}\frac{Z^2\bar{\kappa}\lambda_B}{1+\bar{\kappa}a}. \tag{4.25}$$

In Section 4.3.2 below, we will see that Φ_D, which takes the form of ideal-gas contributions, accounts for the Donnan equation of state (except for the colloidal ideal gas contribution); hence the nomenclature. The term Φ_0 appears as an electrostatic (and hard-core) free energy contribution. This separation is slightly misleading, however, since the two terms both depend on n and Z through the expressions (4.12) and (4.21), which stem from the Donnan potential (4.11) and hence from the balance between electrostatics and entropy.

The effective pair potential between the colloids, $V_2'(R_{ij})$, that appears in the second term of Eq. (4.23), is given by

$$\beta V_2'(r) = \begin{cases} \infty & r < 2a; \\ (1+\Gamma)Z_>^2\lambda_B\dfrac{\exp(-\bar{\kappa}r)}{r} & r > 2a, \end{cases} \tag{4.26}$$

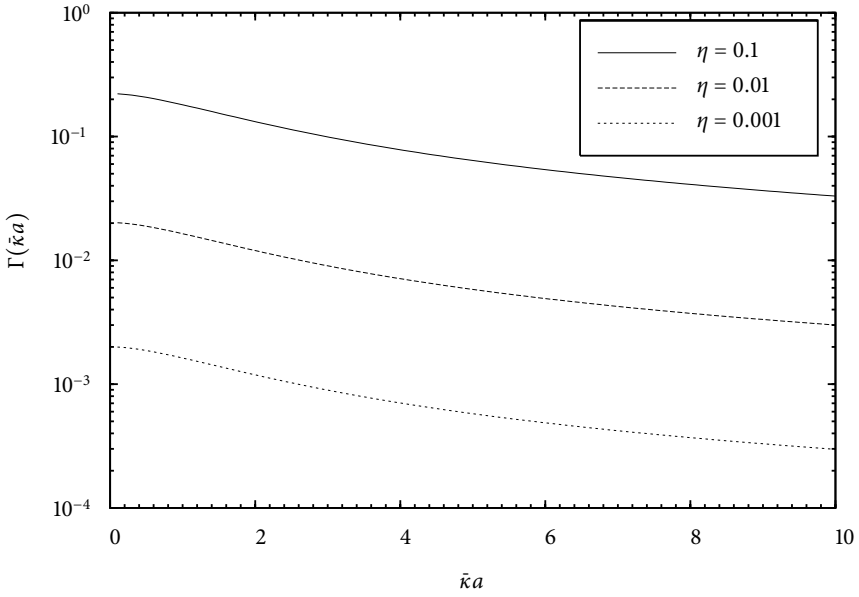

FIGURE 4.2 — The factor Γ of Eq. (4.27) as a function of $\bar{\kappa}a$ and η. For all parameters, $\Gamma \ll 1$, so it can safely be neglected in Eq. (4.26).

with the DLVO-charge given by $Z_> = Z\exp(\bar{\kappa}a)/(1+\bar{\kappa}a)$, and with the parameter Γ defined by

$$\Gamma = \frac{4\pi}{1-\eta}\frac{n}{\bar{\kappa}^3}\left((1+\bar{\kappa}a)^2 e^{-2\bar{\kappa}a} + (\bar{\kappa}a)^2 - 1\right), \tag{4.27}$$

The effective pair interaction $V_2'(r)$ is very similar to the traditional DLVO potential $V_2(r)$ of Eq. (2.16), but with two important differences. The first difference involves the screening parameter $\bar{\kappa}$, defined in Eq. (4.21), in $V_2'(r)$, which is to be contrasted with the reservoir screening parameter κ in $V_2(r)$. The second difference is that the amplitude of $V_2'(r)$ is enhanced compared to $V_2(r)$ by a factor $(1+\Gamma)$. This can be traced back to our particular choice of linear combinations of density profiles that we used to solve the Euler–Lagrange equations.

In Figure 4.2 we plot Γ as a function of the screening parameter $\bar{\kappa}a$ for several values of the packing fraction η. The plot shows that $\Gamma \ll 1$ for essentially all packing fractions of interest here. Moreover, one can also show that $\Gamma \equiv 0$ if the hard-core potentials are defined as $U(\mathbf{r}) = V(\mathbf{r}) + 2\bar{\rho}_\mp W(\mathbf{r})/(\bar{\rho}_+ + \bar{\rho}_-)$ instead of the definition used here. This latter choice does not affect any of the volume terms, but does involve another choice for v_0 and w_0, and does change the expression of $\bar{\phi}$ (see Appendix A.2). For these two reasons we set $\Gamma \equiv 0$ in the remainder of the chapter.

The so-called volume terms Φ_D and Φ_0 are very similar to their canonical counterparts that were derived in Ref. [72]. The main difference is that the present volume term includes the term $-\int d\mathbf{r}\left(\mu_+\rho_+(\mathbf{r}) + \mu_-\rho_-(\mathbf{r})\right)$ due to the grand-canonical character of our calculations. This leads to another difference, since one should now view the Hamiltonian H as a function of n and the reservoir salt concentrations c_s, i.e. one should take the dependence of Φ on $\bar{\rho}_\pm$ and $\bar{\kappa}$ as a dependence on c_s and n through Eqs. (4.21) and (4.12). It is the nontrivial (and nonlinear) dependence of $\beta\Phi_D/V$ and $\beta\Phi_0/V$ on the colloid density n, at fixed c_s, that is responsible for interesting thermodynamic effects, as we will see below.

4.3 Thermodynamics

4.3.1 Free energy

As we have now found the functional form (4.23) for the effective Hamiltonian of the colloids, we are ready to calculate the corresponding free energy $F(N, V, T, c_s)$ defined just below Eq. (2.8). From this the other thermodynamic quantities follow. Since the volume terms in (4.23) are independent of the coordinates of the colloids, we can factor out their Boltzmann weights and write

$$\exp(-\beta F) = \exp[-\beta\Phi]\,\mathrm{tr}_c \exp\left[-\beta \sum_{i<j}^{N} V(R_{ij})\right]. \tag{4.28}$$

This can be rewritten as

$$F = \Phi_D + \Phi_0 + F_{id} + F_{exc}, \tag{4.29}$$

with Φ_D and Φ_0 defined in Eq. (4.25), with the colloidal ideal-gas free energy

$$F_{id} = Nk_BT\big(\ln(n\mathcal{V}) - 1\big), \tag{4.30}$$

with $\mathcal{V}$ an irrelevant volume that account for the kinetic energy and the internal partition function of the colloidal particles. The term F_{exc} is the non-ideal (excess) free energy due to the colloid-colloid pair interactions (4.26). Here we calculate F_{exc} variationally, using the Gibbs–Bogoliubov inequality [108, 109, 110, 111]. Introducing the excess free energy $F_{exc}^{(ref)}$ of a so-called reference system of volume V that contains N particles with *any* pair interaction $V^{(ref)}(R_{ij})$, we approximate the excess free energy F_{exc} of our system of interest here with

$$F_{exc} \approx \min\left\{F_{exc}^{(ref)} + \left\langle \sum_{i<j}\left(V(R_{ij}) - V^{(ref)}(R_{ij})\right)\right\rangle_{ref}\right\}, \tag{4.31}$$

where $\langle\ldots\rangle_{ref}$ denotes a thermodynamic average that is to be evaluated in the reference system, and the minimum is to be performed over a suitably chosen free parameter of the reference system. This procedure is explained in more detail in Appendix C.

4.3.2 Osmotic pressure

The osmotic pressure $\Pi = P - 2c_s kT$ of the suspension under consideration follows from $P = -\partial F/\partial V$ at fixed N and c_s. We can therefore use our expression for F given in Eq. (4.29) to obtain $\Pi(n, c_s)$ explicitly as

$$\Pi = \Pi_D + \Pi_0 + \Pi_{id} + \Pi_{exc} \tag{4.32}$$

with $\Pi_D = -2c_s k_B T - (\partial \Phi_D/\partial V)$, the Van 't Hoff (ideal-gas) contribution $\Pi_{id} = -(\partial F_{id}/\partial V) = nk_B T$, the excess pressure $\Pi_{exc} = -(\partial F_{exc}/\partial V)$, and the remaining term $\Pi_0 = -(\partial \Phi_0/\partial V)$. Explicit general expressions for Π_D, Π_0, and Π_{exc} can of course be given on the basis of Eqs. (4.25), (4.24), and e.g. (4.31), respectively, but it turns out to be instructive to focus on these expressions in the limit of point-colloids with radius $a = 0$ (such that $\eta = 0$): this reduces the algebra and allows for an interesting illustration of cancellations of some of the electrostatic contributions to the osmotic pressure Π. We stress, however, that we used the full expressions in our numerical calculations presented below.

In the point-colloid limit we have

$$\begin{aligned}
\beta\Pi_D &= -2c_s + \bar{\rho}_+ + \bar{\rho}_- \\
&= -2c_s + \sqrt{(Zn)^2 + (2c_s)^2} \\
&= \begin{cases} \dfrac{(Zn)^2}{4c_s} + \mathcal{O}(n^4) & Zn \ll 2c_s \\ Zn - 2c_s + \mathcal{O}(c_s^2) & Zn \gg 2c_s, \end{cases}
\end{aligned} \tag{4.33}$$

and a little tedious but straightforward algebra yields

$$\beta\Pi_0 = \begin{cases} -\dfrac{(Zn)^2}{4c_s} + \mathcal{O}(n^3) & Zn \ll 2c_s \\ -bn^{3/2} + \mathcal{O}(c_s^2) & Zn \gg 2c_s, \end{cases} \tag{4.34}$$

with a coefficient $b = \sqrt{Z\pi\lambda_B} Z^2 \lambda_B/2$. We focus first on the low-density/high-salt regime $Zn \ll 2c_s$, and then on the opposite regime.

The expressions (4.33) and (4.34) show a cancellation of the dominant term in the regime $Zn \ll 2c_s$, such that in this regime $\Pi \simeq \Pi_{id} + \Pi_{exc}$, i.e. the pressure is actually the pressure of the effective one-component system described by the pair-wise screened-Coulomb Hamiltonian. Interestingly, however, one can also write the virial expansion $\beta F_{exc}/V = B_2(\bar{\kappa})n^2 + \mathcal{O}(n^3)$ in this regime, where the second virial coefficient [108] is

$$B_2(\bar{\kappa}) = \frac{1}{2} \int \mathrm{d}\mathbf{r} \left(1 - \exp[-\beta V_2'(r)]\right), \tag{4.35}$$

with the colloidal pair potential $V_2'(r)$ defined in Eq. (4.26). In the limit of weak interactions, the exponent in Eq. (4.35) can be linearized with the result that $B_2 =$

$Z^2/4c_s$ for point-colloids. This means that $\beta\Pi_{exc} \simeq (Zn)^2/4c_s \simeq \beta\Pi_D$, and hence that the pressure can also be approximated by the Donnan expression $\Pi \simeq \Pi_{id} + \Pi_D$. In other words, on the basis of this simple analysis one expects "reliable" results for the pressure (and hence for the thermodynamics) in the regime $Zn \ll 2c_s$ by taking either the full four-term expression (4.32) for Π, or the two two-term expressions $\Pi_{id} + \Pi_D$ and $\Pi_{id} + \Pi_{exc}$, but *not* any other combination. This will be confirmed by our numerical results below.

The situation is a bit more complicated in the opposite low-salt regime $2c_s \ll Zn$, since then (i) no cancellations take place and (ii) the virial expansion for F_{exc} breaks down because of the long-range character of the unscreened-Coulomb interactions.

As a simple approximation for highly charged particles (specifically, particles for which $Z^2\lambda_B/a \gg 1$), the pair correlation function $g_d(r)$ can be set to $g_d(r) = 1$ for $r \gtrsim n^{-1/3}/2$ and to 0 otherwise. One can then show that the lowest order contribution to the excess pressure takes the form $\beta\Pi_{exc} = -b'n^{4/3}$ with $b' = \pi Z^2\lambda_B/12$. Note that this contribution to the pressure is negative; this is caused by the counterions dominating the screening. In this regime, the screening length scales as $\propto n^{-1/2}$, while the inter-particle distance grows as $n^{-1/3}$, causing the repulsions to *decrease* with increasing density, accounting for the negative contribution to the pressure. We find the asymptotic low-salt result

$$\beta\Pi = (1+Z)n - b'n^{4/3} - bn^{3/2}, \tag{4.36}$$

which contains Donnan, colloidal pair, and Debye-Hückel-like contributions. The prefactors of the fractional powers would change if a proper Güntelberg charging process would have been performed [112], but the present analysis is good enough to capture the spinodal instability that is now well-known to be realistic for primitive model systems at sufficiently strong coupling (low enough temperature) [61, 76, 78, 113, 114, 115, 116]. On this basis one could expect that the present theory predicts phase-separation in low-salt colloidal suspensions. Within the full theory for F we indeed find this phenomenon in the next section.

We now illustrate our results for the osmotic pressure by numerically comparing the theoretically predicted values to experimental measurements in Figure 4.3. The experimental system is an ethanol suspension of colloidal silica-spheres, for which $\Pi(n)$ was determined by integration of the measured density profile in sedimentation equilibrium [31, 107]. The system parameters are $Z = 32$, $2c_s = 16\ \mu$M, $\lambda_B = 2.38$ nm and $a = 21.9$ nm. Since $Z\lambda_B/a \approx 3$ we do not expect too much charge renormalization, and as $Zn/2c_s \approx 0.7$ at the highest density considered here ($\eta = 0.01$), this experiment is expected to be in the high-salt regime where not only the full expression (4.32) for Π but also both the one-component expressions $\Pi \simeq \Pi_{id} + \Pi_{exc}$ and the Donnan expression $\Pi \simeq \Pi_{id} + \Pi_D$ are expected to "work" with reasonable accuracy.

This is to some extent confirmed by Fig. 4.3, where the measured osmotic pressure is in quantitative agreement with two of the three theoretical versions at low

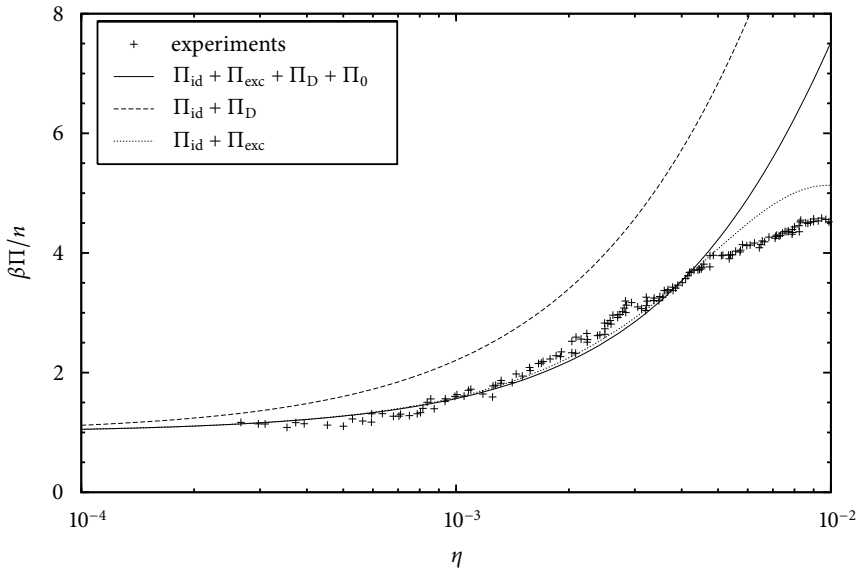

FIGURE 4.3 — Equation of state compared to the experiments of Raşa et al [31], described by the parameters $Z = 32$ for the colloidal charge, $a/\lambda_B = 96.7$ for the radius-to-Bjerrum length ratio, and $2c_s = 16\ \mu$M for the reservoir salt concentration. Shown are the experimental data (crosses), a one-component DLVO system (dotted), the Donnan theory (dashed), and our full linear theory (solid line). Two of the three theoretical curves describe the experimental curves accurately for $\eta \lesssim 0.003$, the Donnan theory is less accurate although still qualitatively reasonable in this regime.

packing fractions $\eta \lesssim 0.003$ or so; the Donnan pressure is less accurate. At higher densities the different theoretical curves deviate from each other (and from the experiment), with the one-component result $\Pi_{id} + \Pi_{exc}$ being closest to the actual experiment. A word of caution is appropriate here, however, since recent work by Biesheuvel indicates that charge regularization is relevant in the present system, i.e. the bare colloidal charge Z is *not* a constant but decreases with density, with significant deviations of the low-density charge being predicted for $\eta \gtrsim 0.002$ [117]. This is rather precisely the regime where the theories begin to deviate from the experiment.

From the fact that the one-component osmotic pressure $\Pi = \Pi_{id} + \Pi_{exc}$ describes the experimental data rather accurately, one may conclude that the experimentally found "inflated" profiles of Ref. [107] do not necessarily require theories such as those of Ref. [29], where a three-component mixture (cations, anions, and colloids) under gravity gives rise to an ion-entropy-induced self-consistent electric field that lifts the colloids to higher altitudes than expected on the basis of gravity alone. The equation of state (4.32)–(4.34) suggests that an alternative description

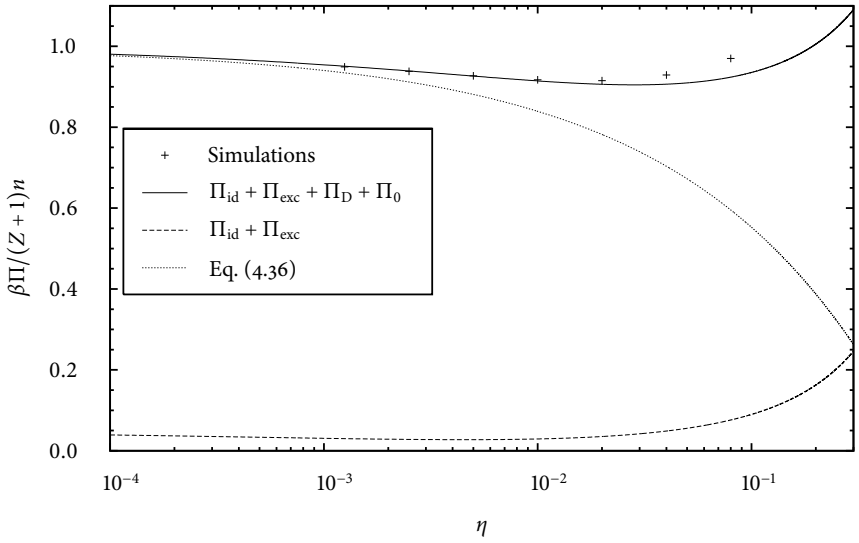

FIGURE 4.4 — Equation of state (compressibility factor) compared to the computer simulation of Ref. [118], where $Z = 40$ and $a/\lambda_B = 22.5$. Shown are the simulation data from [118] (crosses), the pressure Π from our full linear theory (solid line), the approximate low-salt expression (4.36) (dotted), and the pairwise one-component result $\Pi_{id} + \Pi_{exc}$ (dashed). The theoretical curves are based on the reservoir salt concentration $c_s = 10^{-15}$ M, which is low enough to ensure an essentially vanishing co-ion concentration in all state points shown here.

could be given, based on hydrostatic equilibrium of an effective one-component system of colloidal spheres with pairwise screened-Coulomb repulsions only. The latter picture is *not* in contradiction with the existence of the electric field, since the density variation with height implies a variation of the Donnan potential with height through Eq. (4.11). The two pictures are, in this sense, merely two sides of the same coin, at least on length scales beyond which the local density approximation that underlies the one-component theory is valid. On smaller length scales the *source* of this electric field involves deviations from local charge neutrality, which cannot be described by hydrostatic equilibrium and a bulk equation of state alone.

The other experimental system for which we calculate the osmotic pressure is one of the systems that Linse studied by Monte Carlo simulations in Ref. [118]. This system is free of added salt, contains colloids with a charge $Z = 40$ and a radius-to-Bjerrum length parameter of $a/\lambda_B = 22.5$ for monovalent ions (in the notation of Ref. [118] the coupling parameter is $\Gamma_\Pi = 0.0445$). The simulated results are shown in Figure 4.4, together with three versions of the present theory. It is clear that the major contribution to the osmotic compressibility factor originates from the pressure $\Pi_{id} + \Pi_D \approx (Z+1)n$, which, exceeds the one-component combination $\Pi_{id} + \Pi_{exc}$ by at least an order of magnitude for the given parameters and $\eta < 0.1$.

The decrease of $\beta\Pi/n$ for $\eta \lesssim 0.02$ is due to the contribution Π_0. Our calculated pressure describes the simulation data quite well, showing that volume terms may give a pronounced contribution to the thermodynamic properties of low-salt suspensions, while the pairwise DLVO-picture without volume terms breaks down qualitatively. We note, finally, that the expression (4.36) for the pressure in the limit of point-colloids can be seen to describe the low-density behavior of $\beta\Pi/n$ with n as predicted by the full theory and the simulations well.

4.4 Phase diagrams

From the free energy per unit volume $f(n) = F/V$ at fixed c_s, we calculate the chemical potential and the pressure, and we impose the usual conditions of thermodynamic equilibrium (2.9) to find a phase-equilibrium. We already mentioned that this is numerically much less involved than in the canonical calculations of e.g. Ref. [72]. We merely illustrate the feasibility of these calculations here by showing two phase diagrams, for a particular Z, a, and λ_B. In Chapter 5, we will fully exploit the relative simplicity of the grand-canonical formulation of the theory by "scanning" the full parameter space $(Z, \lambda_B/a)$, including a generalization of the present theory to include charge renormalization.

The first set of parameters that we consider is $Z = 7300$, $a = 326$ nm, and $\lambda_B = 0.72$ nm, which corresponds to the experiments of Ref. [51]. The phase diagram that follows from the present theory is displayed in Figure 4.5, and shows phase coexistence with a large density gap at $c_s \lesssim 20$ μM, and only a very small density gap at higher c_s. At a salt concentrations of about 23.8 μM, a liquid–solid–solid triple point occurs (denoted by $\times$ in Fig. 4.5), and at 26.2 μM a solid–solid critical point is located (denoted by $\square$ in the figure). Although somewhat difficult to see in this picture, there is no lower critical point.

The phase diagram of Fig. 4.5 is pretty similar to the one calculated in Ref. [72] using the canonical version of the theory, but with a few substantial differences. The canonical theory, for instance, does not find any solid–solid coexistence, nor does it find a triple point for these parameters. Also the canonical theory predicts a lower critical point, while the current grand-canonical version of the theory does not. Despite these differences the main phenomenon is shared that at low salinity $c_s \lesssim 20$ μM a density gap opens up.

The physical mechanism for these demixing transitions is identical to the ones explained in Refs. [72, 119, 120]: the self energy of the double layers, as represented by the third contribution to the volume term Φ_0 in Eq. (4.25), drives a spinodal instability at low enough c_s, even though the pair interactions are purely repulsive. The underlying physical mechanism is the cohesive energy stabilizing the dense phase, stemming from the decrease of the double layers thickness $\bar{\kappa}^{-1}$ upon increasing the colloid density: this effect brings the charge in the diffuse double layer closer to the oppositely charged colloidal surface. This mechanism is very simi-

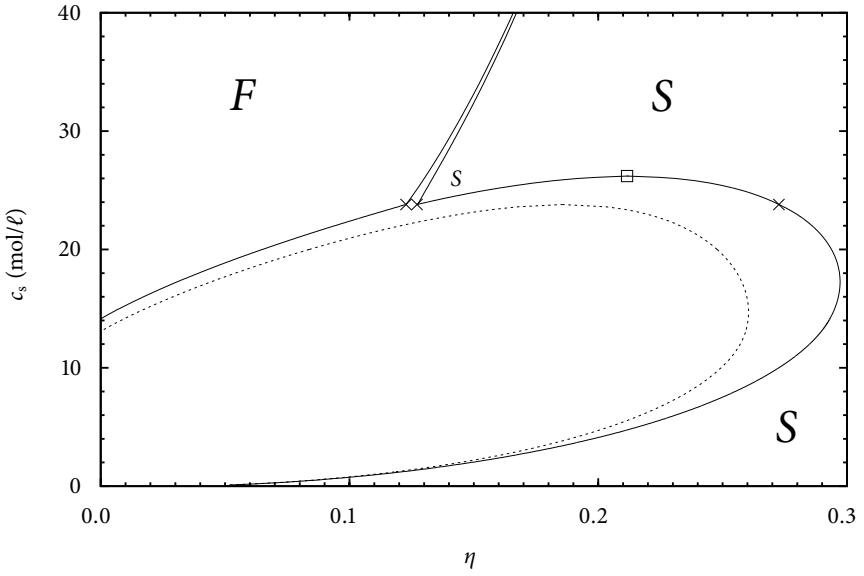

FIGURE 4.5 — Phase diagram for a colloidal suspension as a function of colloidal packing fraction η and reservoir salt concentration c_s. The colloidal radius and charge are $a = 326$ nm and $Z = 7300$, and the solvent is water at room temperature such that the Bjerrum length is $\lambda_B = 0.72$ nm. The solid lines denote fluid–solid and solid–solid binodals, and the dotted line shows the underlying metastable gas–liquid binodal. The fluid–solid–solid triple point is denoted by ×, and the solid–solid critical point by □.

lar to the one that causes gas–liquid demixing in the restrictive primitive model according to Debye–Hückel theory [76, 121].

A word of caution is appropriate here: given that $Z\lambda_B/a \simeq 16$, one expects a substantial renormalization of the charge within nonlinear Poisson–Boltzmann theory for this system, and hence a reduction of the tendency to demix. Whether or not this mechanism for phase separation remains strong enough to yield a large density gap in the phase diagram if charge renormalization is taken into account, will be investigated in Chapter 5.

The second phase diagram that we present here is for the parameters of the experiments of Monovoukas and Gast [122], where $Z = 1200$, $a = 66.7$ nm, and $\lambda_B = 0.72$ nm. We examine the parameters of this experiment, because the experiments reveal a significant density gap, by a factor of three, between the coexisting fluid and solid phases at salinity of the order of 10 μM. Such a large density gap cannot be explained by the DLVO pair potential alone, and hence we investigate here to what extent the volume terms may account for this effect.

The phase diagram, shown in η–$\bar{\rho}_-$ representation in Fig. 4.6, shows the experimental points and three fluid–solid binodals based on the present theory. As the re-

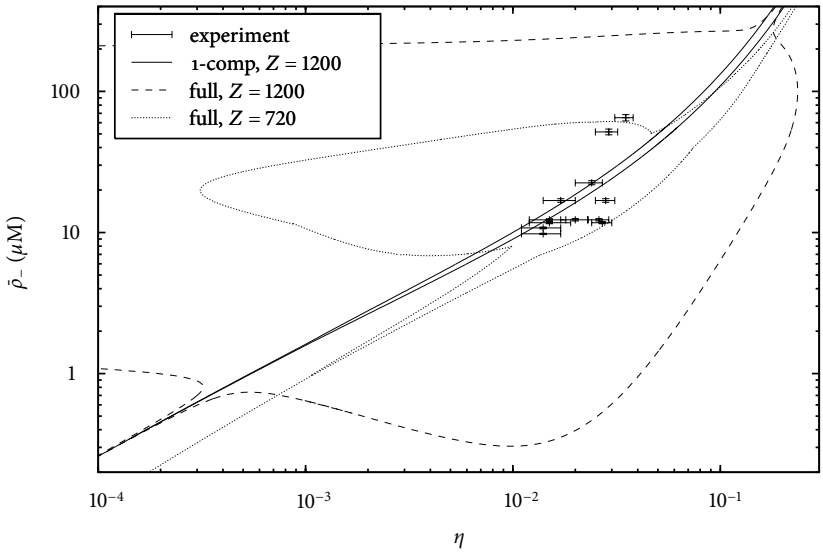

FIGURE 4.6 — Phase diagrams for the parameters of the experiment by Monovoukas and Gast [122]. The Bjerrum length for this system is $\lambda_B = 0.72$ nm and the particle radius is $a = 66.7$ nm. The data points plotted here correspond to the samples for which a fluid–solid phase separation was observed in Ref. [122]. The solid line is a binodal for a one-component DLVO system, the dashed line denotes the phase boundaries for our full linear theory for a charge of $Z = 1200$. The dotted line gives the phase boundary for the same full linear theory, but with a lower charge $Z = 720$.

sults of Ref. [122] seem to be independent of the concentration of added salt for salt concentration lower than approximately 8 μM, we assumed an extra background salt concentration of 8 μM for the experimental points. Note that this representation of the phase diagram, with the vertical axis representing the concentration of added salt instead of the reservoir concentration, is such that the tie-lines (which have been omitted for clarity) are no longer horizontal as in the η–c_s representation, but instead tilted to lower $\tilde{\rho}_-$ at higher η due to the Donnan effect (see also Fig. 4.1).

The first binodal in Fig. 4.6 is the one based on the ideal and excess part of F only, i.e. we assume that Φ_0 and Φ_D vanish (or more accurately: the volume terms are assumed to be merely linear in N and V and do therefore not affect the phase diagram). Although this binodal gives a fair representation of the experimental points (probably this is how $Z = 1200$ was chosen), it does not capture the large density gap. The second binodal is based on the full expression for F, including the volume terms, with $Z = 1200$. We find an enormous density gap that is much larger than experimentally observed, and that extends to unreasonably high salt concentrations. The third binodal is also based on our expression for F with vol-

ume terms, but now for a smaller charge $Z = 720$. Interestingly, this choice gives a density-gap at fluid–solid coexistence in the right salt concentration regime, but the magnitude of the gap is still much bigger than experimentally observed. The reduction of the charge from $Z = 1200$ to $Z = 720$ may give a rough idea of the effect of charge renormalization, and shows that this nonlinear effect reduces the tendency to demix considerably. Theories for charge renormalization [83, 92] show that the renormalized charge is actually not a constant but depends on the screening parameter and the density; the present value $Z = 720$ corresponds to the dilute limit value at $\kappa a \approx 0.8$, i.e. at $c_s \approx 10\ \mu$M, and is fixed here for simplicity. We expect this to be a reasonable lower limit for the renormalized charge in the region in which the phase-separation occurs. Also this system will be investigated within a nonlinear version of Poisson–Boltzmann theory in Chapter 5.

4.5 Conclusion

We have reformulated and re-derived the volume term theory for suspensions of charged colloids [71, 72]. Our present derivation should be more transparent than the original one, for instance because we can now avoid the extra parameter λ that regulates the Coulomb potential from $1/r$ to $\exp(-\lambda r)/r$ with $\lambda \to 0$ only at the end of the calculation. Moreover, the presently derived expressions should be easier to use in numerical calculations of thermodynamic properties and phase diagrams, because the ions are treated grand-canonically instead of canonically, thereby assuring uniform chemical potential of the ions from the outset. Moreover, a direct connection with Donnan theory is now made, with explicit expressions for the Donnan potential and the ion concentration in the system. In the next chapters we will fully exploit the computational advantages and extend the theory to include charge renormalization.

We derived analytic expressions for the osmotic pressure in the point-colloid limit for both the low-salinity and high-salinity limits. The low-salinity limit of the pressure was shown to correspond to the Donnan expression, while in the limit of high salt concentrations the traditional DLVO results are recovered. The present full theory interpolates between these results, and gives a good account of measured and simulated osmotic pressures in both regimes.

We also calculated two phase diagrams. The first one matches the parameters of Ref. [72], and shows a similarly large phase-instability at low salinity, although there are also a few substantial differences. The second phase diagram matches the parameters of the experiments by Monovoukas and Gast of Ref. [122], where an anomalously large density gap at fluid–solid coexistence was reported. Interestingly, the present theory does predict a density gap at fluid–solid coexistence, but its magnitude is much larger than experimentally observed. We stress, however, that these phase diagrams are calculated in a regime where charge renormalization cannot be ignored. The relative transparency of the present derivation allows to systematically include this nonlinear effect into the theory, as will be shown in

Chapter 5.

The linear theory described in this chapter already shows, however, that volume terms can affect the osmotic pressure of low-salt suspensions qualitatively, also in regimes where charge renormalization and other nonlinear effects are *not* expected to be important.

CHAPTER 5

Multi-centered non-linear Poisson–Boltzmann theory

Abstract

In this chapter, we calculate the effective Hamiltonian and the resulting phase behavior of highly charged colloidal spheres (valency Z and radius a) in a 1:1 electrolyte on the basis of a multi-centered nonlinear Poisson-Boltzmann theory. Our theory interpolates between the spherically symmetric cell model for a single colloid and the multi-centered many-body system, and it takes into account simultaneously the effects of charge-renormalization, screened-Coulomb colloid–colloid interactions, and volume terms due to many-body effects. For many values of (Z, a), we calculated phase diagrams as a function of the colloid- and salt-concentration, and we find a gas–liquid spinodal instability for $Z\lambda_B/a \gtrsim 25$, where λ_B is the Bjerrum length. This instability is connected to the undisputed gas–liquid instability of the primitive model with small valencies.

5.1 Introduction

The Poisson–Boltzmann cell model divides the system into Wigner–Seitz cells, each of which is approximated to be spherically symmetric and charge-neutral, such that it suffices to solve the problem in one single cell only [83, 102, 123]. This approximation was reviewed in Chapter 3. It has been very successful in describing phenomena such as charge renormalization and the non-linear screening of the colloid charges by counter-ions. Being a one-particle model, however, it does not take into account any multi-body interactions between the colloids explicitly.

Linear Poisson–Boltzmann theory (see Chapter 4), on the other hand, retains the multi-body geometry of the system, at the expense of disposing of any non-

linear behavior. Effects like charge renormalization [83, 92] and Manning condensation [124, 125] are therefore not described by the linear theories.

While both variations of Poisson–Boltzmann theory agree on the properties of colloidal suspensions at high temperatures and high concentrations of added salt (and thus high screening of the Coulomb-interactions between the colloids), they disagree in the opposite, low-screening parameter regime. The linear theories predict gas–liquid and gas–solid phase instabilities with large density differences between the coexisting phases (such as those in Figs. 4.5 and 4.6) [63, 68, 71, 72, 126]; cell models, on the other hand, predict that such suspensions should be stable [64, 94]. Resulting from these discrepancies, there is an ongoing debate on the question whether or not colloidal suspensions at low ionic strengths can phase separate into a low-density gas and a high-density fluid or solid phase. This debate has been fed by some tentative experimental observations of such broad gas–liquid or gas–solid coexistences [48, 50, 51, 52].

In this chapter, we present a new theory for colloidal suspensions, which behaves, in some way, as an interpolation between the Poisson–Boltzmann cell model and linear Poisson–Boltzmann theory. By changing the size of the cell, we are able to tune the model in a continuous fashion between a purely multi-body linear limit and the pure non-linear cell limit. We therefore capture the best features of both theories: nonlinear effects close to the colloidal surface and the effective interactions for separated colloids.

5.2 The model

We consider a suspension of N hard, spherical colloids of radius a, mass m, fixed charge $-Ze$ and density $n = N/V$ in a continuous background solvent, which is characterized by the Bjerrum length $\lambda_B = e^2/\epsilon k_B T$, with $-e$ the electron charge, ϵ the dielectric constant of the solvent, k_B Boltzmann's constant and T the temperature. The system is in diffusive equilibrium with a salt reservoir of inverse temperature $\beta = 1/k_B T$; the reservoir contains two species of oppositely charged, monovalent, point-like salt ions, each with with density c_s. This gives rise to (yet to be determined) concentrations $\rho_\pm(\mathbf{r})$ of positive and negative ions in the suspension.

We imagine each colloid $i = 1, \ldots, N$ inside a virtual cell of (arbitrary) radius $b > a$, consisting of the points satisfying the relation $|\mathbf{r} - \mathbf{R}_i| < b$ (see Fig. 5.1). We divide the system into two spatial subsets: the cells, and the areas outside the cells. In each of the two subsets, we employ a different approximation, leading to two separate types of solution solutions for the potential. The overall solution is made self-consistent by choosing boundary conditions such that the electric potential $\phi(\mathbf{r})$ and the electric field $\mathbf{E}(\mathbf{r}) = -\nabla\phi(\mathbf{r})$ are continuous throughout the entire system.

This scheme will allow us to describe the full, nonlinear behavior of the electric potential $\phi(\mathbf{r})$ and the ionic density profiles $\rho_\pm(\mathbf{r})$ near the (highly charged)

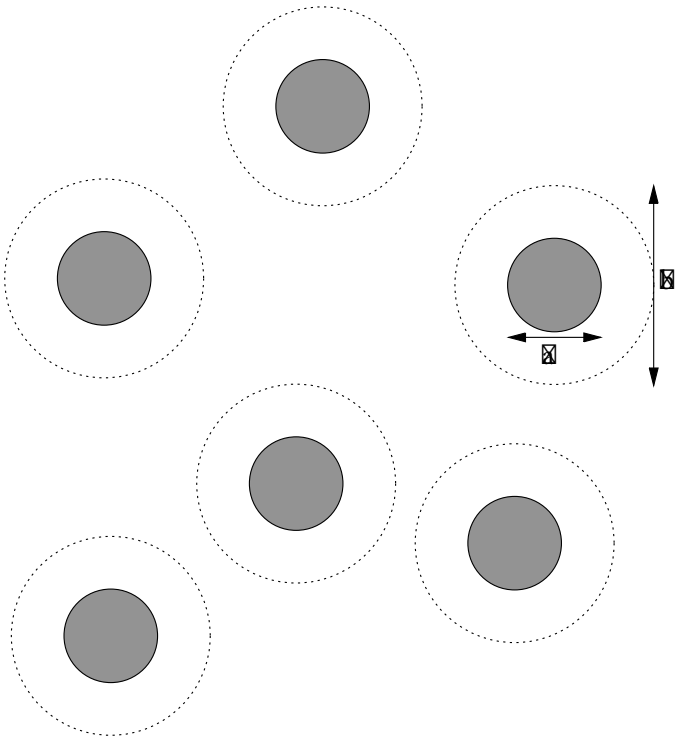

FIGURE 5.1 — Around the colloids, which have a radius a, we construct a virtual cell of (arbitrary) radius b and charge $-Qe$. Inside the cells, we solve the nonlinear, spherically symmetric Poisson–Boltzmann problem (5.1) numerically, while outside the cells we approximate it by the linear Poisson–Boltzmann equation (5.2).

colloids, while still explicitly taking into account interactions between particles through pair potentials and volume terms.

To calculate the electric potential inside the cells, we first approximate all cells to be equal and spherically symmetric. It is then sufficient to solve the problem in a single cell, and because of the spherical symmetry, the Poisson–Boltzmann equation (2.15a)–(2.15b) inside this cell reduces to a much simpler, one-dimensional boundary-value problem:

$$\begin{aligned} &\frac{1}{r^2}\frac{\mathrm{d}}{\mathrm{d}r}\left[r^2\frac{\mathrm{d}}{\mathrm{d}r}\phi_\mathrm{c}(r)\right] = \kappa^2 \sinh\left[\phi_\mathrm{c}(r)\right]; \\ &\phi_\mathrm{c}'(a) = \frac{Z\lambda_\mathrm{B}}{a^2}; \\ &\phi_\mathrm{c}'(b) = \frac{Q\lambda_\mathrm{B}}{b^2}. \end{aligned} \tag{5.1}$$

Here, $-Qe$ is the (yet undetermined) net charge of the cell, and $\phi_c(r)$ is the electric potential inside a cell, such that $\phi(\mathbf{r}) = \phi_c(|\mathbf{r} - \mathbf{R}_i|)$ for $\mathbf{r}$ inside the cell around colloid i. For given Q, Z, κ, λ_B, a and b, the boundary value system (5.1) is easy to solve on a grid on a PC.

In the region outside the cells, we retain the multi-centered character of $\phi(\mathbf{r})$. However, if the cell radius b is large enough (see below), we exploit the fact that the electric potential only varies weakly about some spatial constant $\bar{\phi}$. Therefore, it is allowed to linearize the Poisson–Boltzmann equation around $\bar{\phi}$ in this region, which leads to the so-called linear Poisson–Boltzmann equation:

$$\nabla^2 \left[\phi_\ell(\mathbf{r}) - \bar{\phi}\right] = \bar{\kappa}^2 \left[\tanh\bar{\phi} + \phi_\ell(\mathbf{r}) - \bar{\phi}\right] - \frac{Z^\star \lambda_B}{a^2} \sum_{i=1}^{N} \delta(|\mathbf{r} - \mathbf{R}_i| - a), \tag{5.2}$$

where we have denoted the linear solution as $\phi_\ell(\mathbf{r})$, and the effective screening parameter is defined as $\bar{\kappa}^2 = \kappa^2 \cosh\bar{\phi}$. Note that the source term here is expressed in terms of a yet undetermined *effective* charge $Z^\star$, which is similar to Alexander's concept of a renormalized charged (see Chapter 3).

Following the linear theory that was described in Chapter 4, we take the spatial constant $\bar{\phi}$ equal to the Donnan potential *of the effective system* (i.e. the system with particles of charge $Z^\star$), such that

$$\sinh\bar{\phi} = -\frac{Z^\star n}{2c_s} e^{\eta/(1-\eta)}, \tag{5.3}$$

(cmp. Eq. (4.11)). The effective screening parameter (see Eq. (4.21)) is given by $\bar{\kappa}^2 = 4\pi\lambda_B(\bar{\rho}_+ + \bar{\rho}_-)$, with $\bar{\rho}_\pm$ the spatially averaged concentrations of positive and negative micro-ions in the effective system. The screening in the effective system is hence determined by the total salt concentration, rather than by the salt concentration of the reservoir. The spatially averaged salt concentrations are given by

$$\bar{\rho}_\pm = \frac{1}{2}\left(\sqrt{\left(2c_s e^{-\eta/(1-\eta)}\right)^2 + (Z^\star n)^2} \pm Z^\star n\right), \tag{5.4}$$

as derived in Eq. (4.12). The solution of the linear Poisson–Boltzmann equation (5.2) was derived in Chapter 4, and is of the multi-centered form

$$\phi_\ell(\mathbf{r}) = \bar{\phi} - \tanh\bar{\phi} + \sum_{i=1}^{N} \phi_1(|\mathbf{r} - \mathbf{R}_i|) \tag{5.5}$$

where the DLVO-like orbitals $\phi_1(r)$ are given by

$$\phi_1(r) = -\lambda_B \frac{Z^\star e^{\bar{\kappa}a}}{1 + \bar{\kappa}a} \frac{e^{-\bar{\kappa}r}}{r}. \tag{5.6}$$

Note that with $b = a\eta^{-1/3}$ and $Q = 0$, the standard cell model is retained (with $Z^\star$ the renormalized charge in the Alexander sense [83]), while for $b = a$ and

$Z^\star = Q = Z$, the present theory reduces to the linear theory of Chapter 4. In this chapter, we interpolate between these two extreme cases, and determine, for a fixed value of b, the charges Q and $Z^\star$ by imposing that the potential and the electric field at the boundaries of the cell be equal to the thermodynamical averages of the potential and the electric field outside the cells, respectively. Choosing the origin at $\mathbf{R}_1$, this implies that we impose the conditions

$$\begin{cases} \phi_c(b) = \langle \phi_\ell(b\hat{\mathbf{r}}) \rangle \\ \phi_c'(b) = \langle \hat{\mathbf{r}} \cdot \nabla \phi_\ell(b\hat{\mathbf{r}}) \rangle \end{cases} \tag{5.7}$$

where we introduced the short-hand notation $\hat{\mathbf{r}} = \mathbf{r}/r$ for the radial unit vector. The left hand sides of these equations are known from the numerical solution of Eq. (5.1). The right hand sides of the equations can be expanded using Eqs. (5.5) and (5.6) to

$$\phi_\ell(b) = \bar{\phi} - \tanh\bar{\phi} + \phi_1(b) + \sum_{i=2}^{N} \phi_1(|b\hat{\mathbf{r}} - \mathbf{R}_i|), \tag{5.8a}$$

$$\nabla\phi_\ell(b) = \phi_1'(b)\hat{\mathbf{r}} + \sum_{i=2}^{N} \nabla\phi_1(|b\hat{\mathbf{r}} - \mathbf{R}_i|), \tag{5.8b}$$

where we again have put colloid $i = 1$ in the origin. The thermodynamic averages of the summations over the colloid coordinates in the right hand side of these equations can be expressed in terms of the colloid–colloid pair distribution function $g_2(|\mathbf{R}|)$ as

$$\left\langle \sum_{i=2}^{N} \phi_1(|\mathbf{r} - \mathbf{R}_i|) \right\rangle \approx n \int \mathrm{d}\mathbf{R}\, g_2(|\mathbf{R}|)\phi_1(|\mathbf{r} - \mathbf{R}|) \tag{5.9a}$$

and

$$\left\langle \sum_{i=2}^{N} \nabla\phi_1(|\mathbf{r} - \mathbf{R}_i|) \right\rangle \approx n \int \mathrm{d}\mathbf{R}\, g_2(|\mathbf{R}|)\phi_1'(|\mathbf{r} - \mathbf{R}|)\frac{\mathbf{r} - \mathbf{R}}{|\mathbf{r} - \mathbf{R}|}. \tag{5.9b}$$

In principle, the pair-distribution function $g_2(r)$ that we use here to calculate the thermodynamic average needs to be calculated self-consistently from the same effective Hamiltonian (5.17)–(5.19) that we are trying to calculate here. For simplicity, however, we will use a very simplified pair-distribution function, given by

$$g_2(r) = \begin{cases} 0 & r < 2b; \\ 1 & r > 2b. \end{cases} \tag{5.10}$$

This pair distribution function is such that the colloids are randomly distributed, but the cells cannot overlap. An advantage of this particular form of $g_2(r)$ is that the integrals on the right hand sides of Eqs. (5.9a) and (5.9b) can be calculated

analytically, which greatly reduces the complexity of the numerical work. After tedious but straightforward calculations, we find that the analytic expressions for the integrals (5.9a) and (5.9b) are given by

$$\left\langle \sum_{i=2}^{N} \phi_1(|\mathbf{r}-\mathbf{R}_i|) \right\rangle \approx -Z^\star \frac{4\pi\lambda_B n}{\bar{\kappa}^2} \frac{1+2\bar{\kappa}b}{1+\bar{\kappa}a} e^{-\bar{\kappa}(b-a)} \frac{1-e^{-2\bar{\kappa}b}}{2\bar{\kappa}b} \tag{5.11a}$$

and

$$\left\langle \sum_{i=2}^{N} \nabla\phi_1(|\mathbf{r}-\mathbf{R}_i|) \right\rangle \approx -Z^\star \frac{4\pi\lambda_B n}{\bar{\kappa}} \frac{1+2\bar{\kappa}b}{1+\bar{\kappa}a} e^{-\bar{\kappa}(b-a)} \frac{e^{-2\bar{\kappa}b}(1+\bar{\kappa}b)+\bar{\kappa}b-1}{2(\bar{\kappa}b)^2} \hat{\mathbf{r}}. \tag{5.11b}$$

Combining all these results, we find that the continuity conditions (5.7) reduce to the following expressions for the electric potential

$$\phi_\ell(b) = \bar{\phi} - \tanh\frac{\bar{\phi}}{4} - \frac{\lambda_B}{b} \frac{Z^\star e^{\bar{\kappa}a}}{1+\bar{\kappa}a} e^{-\bar{\kappa}a} \left[1+\eta_c\zeta(\bar{\kappa}b)\right] \tag{5.12a}$$

and for the electric field

$$\nabla\phi_\ell(b) = \frac{\lambda_B}{b^2} \frac{Z^\star e^{\bar{\kappa}a}}{1+\bar{\kappa}a} \frac{1+\bar{\kappa}b}{e^{\bar{\kappa}b}} \left[1-\eta_c\xi(\bar{\kappa}b)\right] \hat{\mathbf{r}} \tag{5.12b}$$

at the boundary of the cell, where we denoted the effective packing fraction of the cells by $\eta_c = (b/a)^3\eta$. For convenience, we have defined the two auxiliary functions $\xi(x)$ and $\zeta(x)$ as

$$\zeta(x) = \frac{3}{2}(1+2x)\frac{1-e^{-2x}}{x^3} \tag{5.13a}$$

$$\xi(x) = \frac{3}{2}\frac{1+2x}{1+x}\frac{(1+x)e^{-2x}+x-1}{x^3}. \tag{5.13b}$$

With the linear solution $\{\phi_\ell(b), \nabla\phi_\ell(b)\}$ at the cell boundary now explicitly known in terms of $Z^\star$, the two equations Eq. (5.7) for the two unknowns $\{Z^\star, Q\}$ can now be solved, fixing the charges $Z^\star$ and Q for any value of the cell radius b. Note specifically that the continuity of the electric field leads to an explicit relation between the net cell charge Q and the effective charge $Z^\star$:

$$\frac{Q}{Z^\star} = \frac{e^{\bar{\kappa}a}}{1+\bar{\kappa}a}\frac{1+\bar{\kappa}b}{e^{\bar{\kappa}b}}\left[1-\eta_c\xi(\bar{\kappa}b)\right]. \tag{5.14}$$

In the low density limit $\eta \to 0$, the last factor on the right hand side of this equation reduces to 1, and the relation reads

$$Q\frac{e^{\bar{\kappa}b}}{1+\bar{\kappa}b} = Z^\star\frac{e^{\bar{\kappa}a}}{1+\bar{\kappa}a}. \tag{5.15}$$

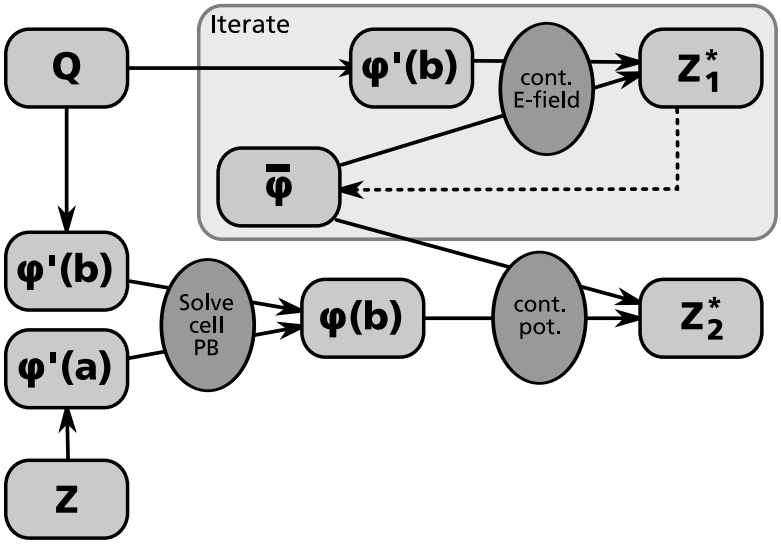

FIGURE 5.2 — Computational scheme how to solve the set of equations (5.7).

Therefore, at low densities, the system can be equivalently viewed as a system of particles of size a and charge $Z^\star$, as we do in the current chapter, or as a system of particles of size b and charge Q. The latter approach fails at higher densities, because the cells are likely to overlap, in that case.

A scheme to solve the set of equations (5.7) at fixed Z, κ, η, λ_B and b, is depicted in Fig. 5.2. We pick a starting value for the charge Q of the cells and the effective charge $Z^\star$ of the colloids. From these, we calculate the electric field at the cell boundary and the Donnan potential $\bar{\phi}$ and screening constant $\bar{\kappa}$ as outlined above Eq. (5.4). These quantities then allow us to find a first value for the DLVO charge $Z_1^\star$ from Equation (5.12b). However, as the value of the Donnan potential $\bar{\phi}$ and the screening constant $\bar{\kappa}$ depends on the effective charge $Z_1^\star$ that we just calculated, we we need to iterate this process until the charge $Z_1^\star$ converges to its final value.

On the other hand, after we have picked a cell charge Q, both boundary conditions of the nonlinear cell problem (5.1) are fixed. Hence, the boundary value problem (5.1) can be solved numerically, resulting in a value for the potential $\phi(b)$ at the cell surface. We then exploit Eq. (5.12a) to calculate a second value $Z_2^\star$ for the effective charge of the cell. For simplicity, we use the value of the Donnan potential $\bar{\phi}$ that we calculated before, and which depends on $Z_1^\star$ rather than $Z_2^\star$; as we will eventually demand that $Z_1^\star = Z_2^\star$, this is not a problem.

For the equations (5.7) to be satisfied, the two DLVO charges $Z_1^\star$ and $Z_2^\star$ must be equal. It thus suffices to solve the one-dimensional problem $Z_1^\star(Q) - Z_2^\star(Q) = 0$.

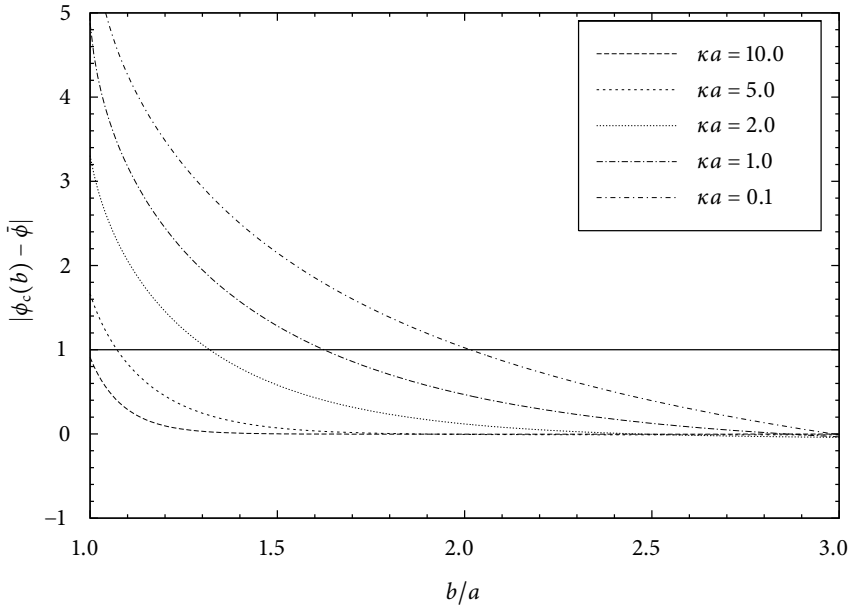

FIGURE 5.3 — The figure shows the values of $|\phi_c(b) - \bar{\phi}|$ as a function of b/a for a typical colloidal system with charge $Z = 1000$, colloid radius $a = 100\lambda_B$ and density $\eta = 0.01$ for several values of the screening parameter κa. The optimal value for the cell radius b is chosen such that $|\phi_c(b) - \bar{\phi}| \sim 1$. Note that for high screening $\kappa a = 10$, the condition $|\phi_c(b) - \bar{\phi}| < 1$ holds already for the smallest possible cell radius $b = a$. In that case, we simply make the choice $b = a$ and the theory reduces to the linear theory of Chapter 4.

5.3 Choosing an optimal cell radius

Except for the cell radius b, all parameters in our model are now fixed. The parameter b can, in principle, still be chosen freely; it should be in the range $1 \leq b/a \leq \eta^{-1/3}$. There are, however, some considerations to take into account with regards to its choice. In order to ensure that the linear approximation outside the cells of Eq. (5.2) is valid, the cell radius b should be chosen such that it is large enough for all the non-linear behavior to be contained inside the cells. On the other hand, it be chosen as small as possible, in order to minimize any overlaps between cells.

The first condition can be satisfied by demanding that the condition

$$|\phi_c(b) - \bar{\phi}| \approx 1 \tag{5.16}$$

holds. An example is shown in Fig. 5.3, where, for different screening parameters and a fixed density, the values of $|\phi_c(b) - \bar{\phi}|$ have been plotted as a function of the cell radius. It is clear from the figure, that with decreasing salt concentration and screening, the cell radius needs to be chosen larger and larger. For high screening, on the other hand, the cell radius can be chosen close or equal to the colloid radius.

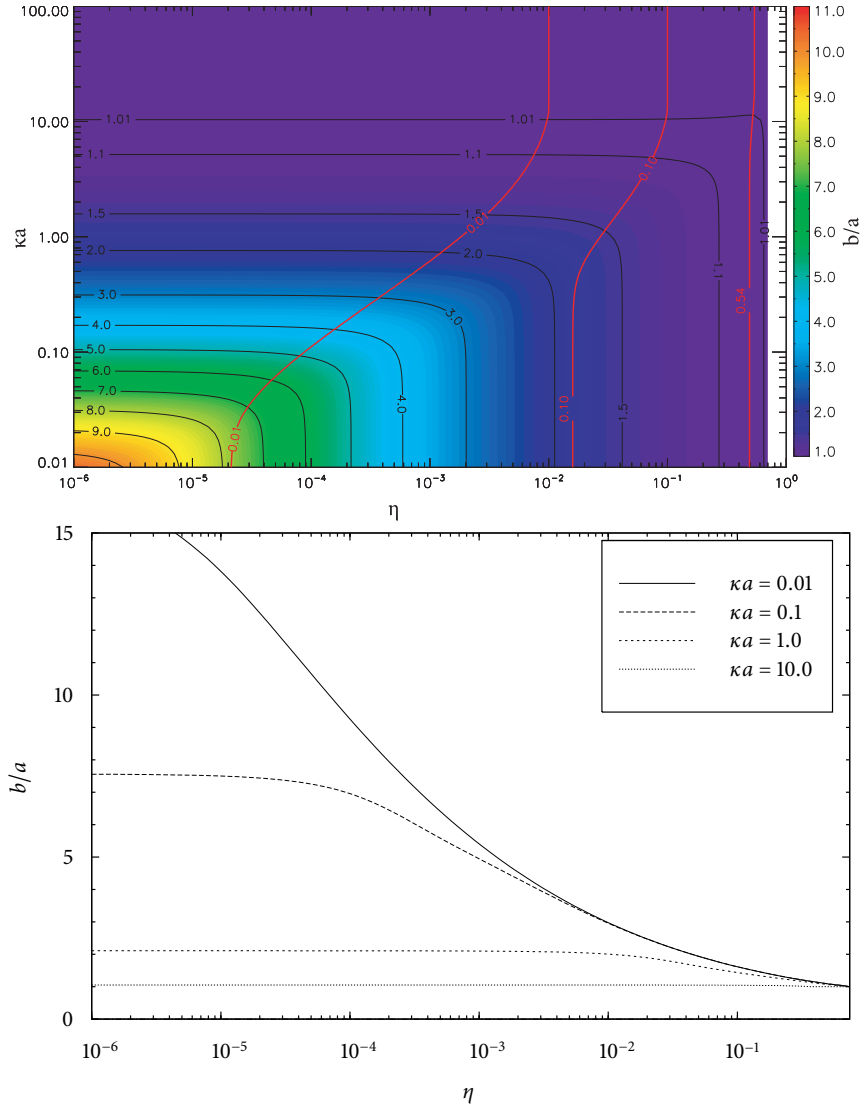

FIGURE 5.4 — The figure shows the optimal cell radius b/a (as determined from Eq. (5.16)) for a system with charge $Z = 1200$ and colloidal size $a/\lambda_B = 92.6$. The top figure shows the entire η–κa plane, while the lower figure shows some horizontal cuts through this plane at constant κa. In the top figure, lines of equal b/a are drawn in black, while lines of equal cell packing fractions $\eta_c = \eta(b/a)^3$ are drawn in red. It can be clearly seen that the cells are closely packed only in very high density regimes.

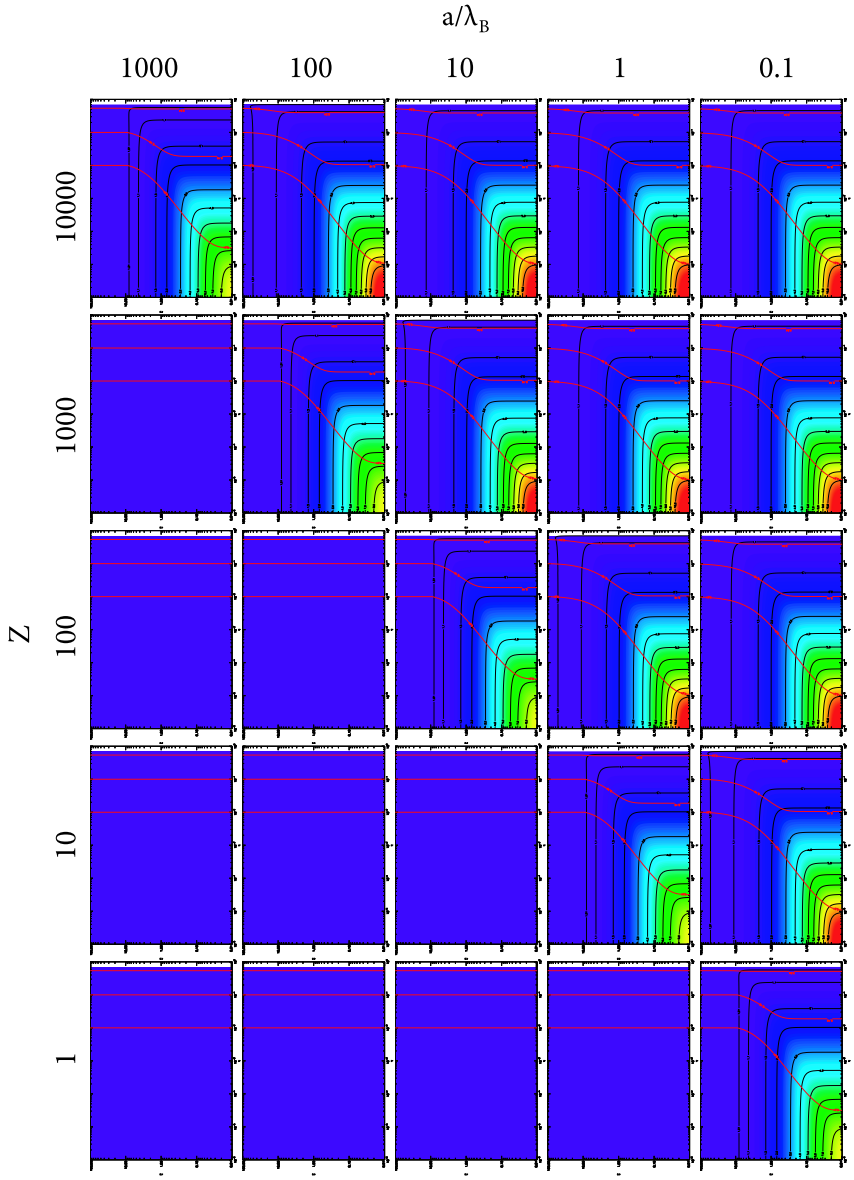

FIGURE 5.5 — The optimal cell radius b/a in the meta-plane Z–a/λ_B. Each of the small figures is a diagram similar to the top figure of Fig. 5.4, i.e., showing b/a as a function of $10^{-6} < \eta < 1$ and $0.01 < \kappa a < 100$. The color coding is identical to that of Fig. 5.4. Note that for $Z\lambda_B/a < 1$, we find that $b \approx a$ for all η and κ while for $Z\lambda_B/a > 10$, the cells are significantly larger than the colloids for low densities and screenings.

The second condition translates into the requirement that the colloid–colloid pair potential at contact of the cells (i.e. $|\mathbf{R}_{ij}| = 2b$) must be much larger than $k_\mathrm{B}T$, or $nb^3 \ll 1$. For the colloidal parameters of interest here ($Z > 10$, $Z\lambda_\mathrm{B}/a > 0.1$) and the choice of b as outlined in Eq. (5.16), this requirement is easily met; only in extreme parameter regimes, such as $Z \sim 1$ and $a/\lambda_\mathrm{B} > 10$, it fails.

The criterion (5.16) leads to values of b/a that change monotonically from $b/a \to 1$ in both the high-screening $\kappa a > 5$ and the high-packing limit $\eta > 0.5$ to cell radii of well larger than $b/a = 10$ in the low-density ($\eta < 10^{-3}$), low-screening ($\kappa a < 0.1$) regime. This is clearly visible in Figure 5.4, where the values for b/a, as determined from Eq. (5.16), are plotted for a typical colloidal system with $Z = 1000$, $a/\lambda_\mathrm{B} = 100$ and $\eta = 0.01$, for several values of the screening parameter κa. Note that indeed the cell radii increase as the screening decreases. For low κa, the system is dominated by counter-ions, and the values of the cell radii only depend on the density; in the highly-screened regime, on the other hand, the system is salt-dominated, and the optimal cell radii only depend on the screening parameter κa.

In the top figure of Fig. 5.4, also the effective packing fractions of the cells are shown (in red). It can clearly be observed that the effective packing fraction of the cells stays well below the freezing limit $\eta_\mathrm{c} \approx 0.5$ for almost the entire region of interest.

In Figure 5.5, we show the optimal cell radius b/a as a function of η and κa for many different values of the colloidal charge Z and the colloidal radius a/λ_B. For couplings lower than $Z\lambda_\mathrm{B}/a = 1$ (i.e., diagrams *above* the line $Z\lambda_\mathrm{B}/a = 1$), the cells are all very small, and almost no non-linear effects occur. For $Z\lambda_\mathrm{B}/a > 10$, on the other hand, there are significantly large cells; this is exactly the parameter regime where the linear theory of Chapter 4 fails. It is thus to be expected that the present model will give better results for these large couplings, because the non-linear behavior will be taken into account correctly.

5.4 The Hamiltonian and the free energy

With the cell radius determined by the condition of Eq. (5.16) and the charges Q and $Z^\star$ determined from the continuity of the potential and the electric field, as described by Eq. (5.7), the electric potential $\phi(\mathbf{r})$, and hence, from Boltzmann's relation Eq. (2.14), the ionic density profiles $\rho_\pm(\mathbf{r})$, are known explicitly, both inside and outside the cells. The grand potential, as given by Eq. (2.10), and the Hamiltonian (2.8) can thus be evaluated explicitly.

The effective Hamiltonian (2.10) can be formally split into three terms, such that $\beta H = \beta\Omega_\mathrm{c} + \beta\Omega_\ell - \beta\,\delta\Omega$, with the individual terms given by

$$\begin{aligned}\beta\Omega_\mathrm{c} = \sum_{\alpha=\pm}\int_\mathrm{cells} \mathrm{d}\mathbf{r}\,\rho_\alpha(\mathbf{r})\left[\ln\frac{\rho_\alpha(\mathbf{r})}{c_\mathrm{s}} - 1\right] \\ + \frac{1}{2}\int_\mathrm{cells}\mathrm{d}\mathbf{r}\,[\rho(\mathbf{r}) + q(\mathbf{r})]\phi(\mathbf{r});\end{aligned} \tag{5.17}$$

$$\beta\Omega_\ell = \sum_{\alpha=\pm}\int \mathrm{d}\mathbf{r}\left\{\bar\rho_\alpha\left[\ln\frac{\bar\rho_\alpha}{c_\mathrm{s}}-1\right]+\frac{(\rho_{\ell,\alpha}(\mathbf{r})-\bar\rho_\alpha)^2}{2\bar\rho_\alpha}\right\} \tag{5.18}$$
$$+\frac{1}{2}\int \mathrm{d}\mathbf{r}\,[\rho_\ell(\mathbf{r})+q^\star(\mathbf{r})]\phi_\ell(\mathbf{r})$$
$$\beta\,\delta\Omega = \sum_{\alpha=\pm}\int_{\text{cells}} \mathrm{d}\mathbf{r}\left\{\bar\rho_\alpha\left[\ln\frac{\bar\rho_\alpha}{c_\mathrm{s}}-1\right]+\frac{(\rho_{\ell,\alpha}(\mathbf{r})-\bar\rho_\alpha)^2}{2\bar\rho_\alpha}\right\} \tag{5.19}$$
$$+\frac{1}{2}\int_{\text{cells}} \mathrm{d}\mathbf{r}\,[\rho_\ell(\mathbf{r})+q^\star(\mathbf{r})]\phi_\ell(\mathbf{r}).$$

Here, $\rho_{\ell,\pm}(\mathbf{r})$ denotes the density of the positive and negative micro-ions in the effective (linear) system, respectively, $\rho_\ell(\mathbf{r}) = \rho_{\ell,+}(\mathbf{r}) - \rho_{\ell,-}(\mathbf{r})$ is the charge distribution in the effective system, and $q^\star(\mathbf{r}) = -(Z^\star/4\pi a^2)\sum_{i=1}^N \delta(|\mathbf{r}-\mathbf{R}_i|-a)$ denotes the colloidal charge distribution of the effective system. Note that the integrations in Ω_c and $\delta\Omega$ are taken over the cell interiors (i.e. $a \le |\mathbf{r}-\mathbf{R}_i| \le b$ for all i), while the integration in Ω_ℓ is over the entire system volume.

The first term of the effective Hamiltonian H, Eq. (5.17), describes the cell-part of the system. Using that all the cells are equivalent, and that the charge distribution $\rho_\mathrm{c}(\mathbf{r})$ and the electric potential $\phi_\mathrm{c}(\mathbf{r})$ inside the cells satisfy Boltzmann's relation (2.14) and the non-linear Poisson–Boltzmann equation (5.1), the internal thermodynamic potential of each of the cells can be written in the form

$$\frac{\beta\Omega_\mathrm{c}}{N} = -\frac{Z}{2}\phi_\mathrm{c}(a) + 4\pi c_\mathrm{s}\int_a^b \mathrm{d}r\, r^2\big[\phi_\mathrm{c}(r)\sinh\phi_\mathrm{c}(r) - 2\cosh\phi_\mathrm{c}(r)\big]. \tag{5.20}$$

This quantity can be easily calculated from the electric potential $\phi_\mathrm{c}(r)$ in the cells, which is (numerically) known,

The second term, (5.18), is the grand potential of the effective system. Note, that we integrate over the entire system volume excluded the colloidal hard cores, and that hence the cells have been doubly counted, as they have been both taken into account in $\beta\Omega_\mathrm{c}$ and in Ω_ℓ. Because we have made sure by our choice of b that the electric potential is close to the effective Donnan potential $\bar\phi$, it is a good approximation here to expand the logarithms of the entropic part of the free energy around the Donnan potential, as has been done in Eq. (5.18). The resulting grand potential $\beta\Omega_\ell$ then exactly matches the linear theory of Chapter 4. Therefore, after the tedious work of substituting the linear solution (5.5)–(5.6) for the electric potential, and carrying out the multi-centered integrals, we find that the grand potential of the effective system can be written as

$$\Omega_\ell = \Phi_\mathrm{D}(Z^\star,\bar\kappa,\eta) + \Phi_0(Z^\star,\bar\kappa,\eta) + \sum_{i<j}^N V_2(R_{ij};Z^\star,\bar\kappa). \tag{5.21}$$

In this expression, the DLVO-like pair potential $v(R_{ij};Z^\star,\bar\kappa)$ was defined in (2.16) and $\Phi_\mathrm{D}(Z^\star,\bar\kappa,\eta)$ and $\Phi_0(Z^\star,\bar\kappa,\eta)$ are volume terms, given by

$$\frac{\beta\Phi_\mathrm{D}}{V} = \sum_{\alpha=\pm}\bar\rho_\alpha\left(\ln\frac{\bar\rho_\alpha}{c_\mathrm{s}}-1\right), \tag{5.22}$$

which describes the salt equilibrium between system and reservoir, and

$$\frac{\beta\Phi_0}{V} = -\frac{1}{2}\frac{(Z^\star n)^2}{\bar{\rho}_+ + \bar{\rho}_-} + \frac{\eta}{1-\eta}\frac{2\bar{\rho}_+\bar{\rho}_-}{\bar{\rho}_+ + \bar{\rho}_-} + \frac{n}{2a}\frac{Z^{\star 2}\lambda_B}{1+\bar{\kappa}a}, \tag{5.23}$$

which contains self-energy terms, such as those describing a colloid in its own cloud of counter-ions.

The third term of the Hamiltonian, (5.19), is a correction term, which we subtract from the Hamiltonian in order to correct for the double counting of the cells, which have both been counted in Ω_c and in Ω_ℓ.

In the next section, we will explicitly calculate this third term by substituting the effective potential $\phi_\ell(\mathbf{r})$ into the expression (5.19). In Appendix B, we calculate the same correction term in an alternative way, by additionally approximating the potential $\phi_\ell(\mathbf{r})$ and the ionic density profiles $\rho_{\ell,\pm}(\mathbf{r})$ in the correction term (5.19) to be spherically symmetric. This extra approximation leads to quantitatively different thermodynamic properties compared to the correction term as calculated in the next section (see below).

5.4.1 The correction term $\beta\,\delta\Omega$

To calculate the correction term $\delta\Omega$, we need to evaluate the expression (5.19) with the multi-centered expression of Eqs. (5.5) and (5.6), extrapolated to the cell interiors.

We start by calculating the minimum of the functional (5.19) with regards to the ionic density profiles $\rho_\pm(\mathbf{r})$. The minimum conditions for this functional are given by

$$\ln\frac{\bar{\rho}_\pm}{c_s} + \frac{\rho_{\ell_\pm}(\mathbf{r}) - \bar{\rho}_\pm}{\bar{\rho}_\pm} \pm \phi_\ell(\mathbf{r}) = 0. \tag{5.24}$$

Substituting this into (5.19), the correction term can be written in the form

$$\beta\,\delta\Omega = \sum_{\alpha=\pm} N V_{\text{cell}}\bar{\rho}_\alpha\left[\ln\frac{\bar{\rho}_\alpha}{c_s} - 1\right] + \frac{NV_{\text{cell}}}{2}Z^\star n\bar{\phi}_\ell + \frac{1}{2}\int_{\text{cells}} \mathrm{d}\mathbf{r}\, q^\star(\mathbf{r})\phi_\ell(\mathbf{r}), \tag{5.25}$$

where $\phi_\ell(\mathbf{r})$ is the solution of the linear Poisson–Boltzmann equation, given by Eqs. (5.5) and (5.6), and the integration is over the interior $a < |\mathbf{r} - \mathbf{R}_i| < b$ of all cells. Here $V_{\text{cell}} = \frac{4}{3}\pi(b^3 - a^3)$ is the volume of the cell interior.

The integration over the cell interiors can be carried out explicitly by substituting the multi-centered expressions for $q^\star(\mathbf{r})$ and $\phi_\ell(\mathbf{r})$, converting the integral to momentum space and using Parseval's identity. After tedious calculation, we then

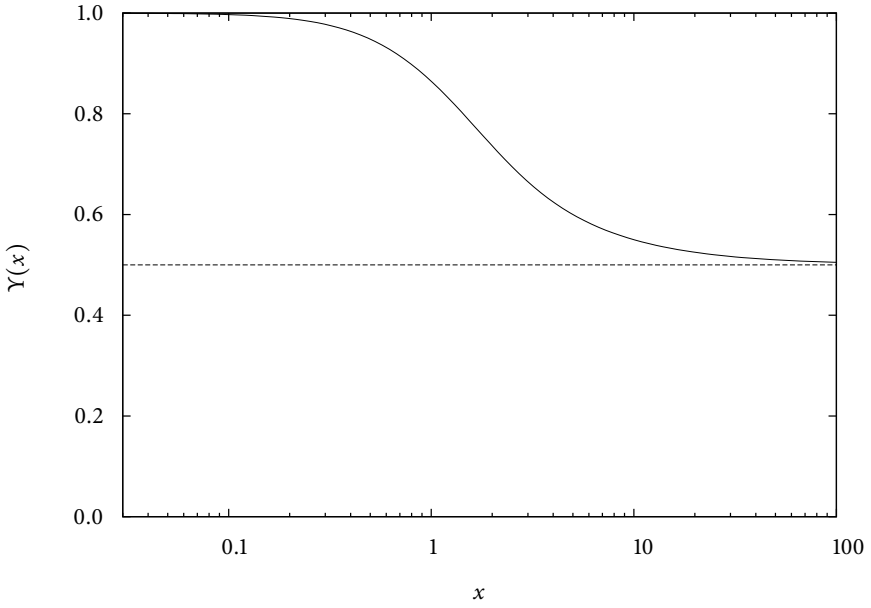

FIGURE 5.6 — The factor $\Upsilon(x)$ of Eq. (5.27). The factor $1-\Upsilon(\bar{\kappa}a)$ describes the deviation of the colloid–colloid pair-interactions as a function of the effective screening, if the correction term $\delta\Omega$ is calculated in a multi-centered fashion. Note that thus the colloidal pair interactions would disappear totally at low screenings, and in the high salt limit, would be a factor 2 smaller than the usual DLVO theory predicts.

find the following final expression for the multi-centered correction:

$$\begin{aligned}\frac{\beta\,\delta\Omega}{N} =& V_{\text{cell}}\sum_{\alpha=\pm}\bar{\rho}_\alpha\left[\ln\frac{\bar{\rho}_\alpha}{c_s}-1\right]+\Upsilon(\bar{\kappa}a)\left(\frac{Z^\star e^{\bar{\kappa}a}}{1+\bar{\kappa}a}\right)^2\frac{1}{N}\sum_{i<j}\lambda_B\frac{e^{-\bar{\kappa}R_{ij}}}{R_{ij}}\\ &+\frac{1}{2}V_{\text{cell}}\bar{\rho}\bar{\phi}+\frac{\lambda_B}{2a}\frac{Z^{\star 2}}{1+\bar{\kappa}a}-\frac{1}{2}Z^\star\left\{\bar{\phi}+\frac{1}{1-\eta}\frac{Z^\star n}{\bar{\rho}_+ +\bar{\rho}_-}\right\}.\end{aligned} \tag{5.26}$$

The factor $\Upsilon(x)$ describes the deviation of this interaction from a purely DLVO type. It is explicitly given by

$$\Upsilon(x)=\frac{1+x}{x}\frac{1-e^{-2x}}{2}, \tag{5.27}$$

and is plotted in Fig. 5.6.

Gathering the results from Eqs. (5.20), (5.21)–(5.23), and (5.26), we find that the

effective Hamiltonian is given by

$$\begin{aligned}\beta H =&\beta\Phi_{\rm c} + \beta\Phi_{\rm D} + \beta\Phi_0' \\ &+ \left\{1 - \Upsilon(\bar{\kappa}a)\right\} \sum_{i<j} V_2(R_{ij}; Z^\star, \bar{\kappa})\end{aligned} \tag{5.28}$$

where the effective colloid–colloid pair potential $V_2(R_{ij})$ was defined in Eq. (2.16) and where the cell self-energy is in this case given by

$$\begin{aligned}\frac{\beta\Phi_{\rm c}}{N} =&4\pi c_{\rm s} \int_a^b {\rm d}r\, r^2 \left\{\phi_{\rm c}(r)\sinh\phi_{\rm c}(r) - 2\cosh\phi_{\rm c}(r)\right\} \\ &- \frac{Z}{2}\phi_{\rm c}(a) - V_{\rm cell}\sum_{\alpha=\pm}\bar{\rho}_\alpha\left[\ln\frac{\bar{\rho}_\alpha}{c_{\rm s}} - 1\right],\end{aligned} \tag{5.29}$$

the Donnan contribution is defined in Eq. (5.22), and the final volume term is

$$\frac{\beta\Phi_0'}{V} = \left\{1 - \eta\left(\tfrac{b^3-a^3}{a^3}\right)\right\}\frac{Z^\star n}{2}\bar{\phi} + \frac{\eta}{1-\eta}\frac{2\bar{\rho}_+\bar{\rho}_-}{\bar{\rho}_+ + \bar{\rho}_-}. \tag{5.30}$$

Note that in the limit $b \to a$, the cell self-energy (5.29) reduces to $\beta\Phi_{\rm c} \to -ZN\phi_{\rm c}(a)/2$. Furthermore, in this limit, $Z^\star \to Z$, and $\phi_{\rm c}(a) \to \bar{\phi} - \tanh\bar{\phi} + \phi_1(a) + \sum_{i=2}^N \phi_1(|a\hat{\mathbf{r}} - \mathbf{R}_i|)$, from which we find that

$$\begin{aligned}\left.\frac{\beta(\Phi_{\rm c} + \Phi_{\rm D} + \Phi_0')}{V}\right|_{b\to a} =& \sum_{\alpha=\pm}\bar{\rho}_\alpha\left[\ln\frac{\bar{\rho}_\alpha}{c_{\rm s}} - 1\right] - \frac{n}{2a}\frac{Z^2\lambda_{\rm B}}{1+\bar{\kappa}a} - \frac{(Zn)^2}{2(\bar{\rho}_+ + \bar{\rho}_-)} \\ &+ \frac{\eta}{1-\eta}\frac{2\bar{\rho}_+\bar{\rho}_-}{\bar{\rho}_+ + \bar{\rho}_-} - \frac{Zn}{2}\sum_{i=2}^N \phi_1(|b\mathbf{n}_1 - \mathbf{R}_i|),\end{aligned} \tag{5.31}$$

where the first four terms correspond to the volume terms of the linear theory that was presented in Chapter 4. The final term cancels, on average, the factor $\Upsilon(\bar{\kappa}a)$ in Eq.(5.28); these terms do not cancel exactly because the multi-centered geometry was replaced by one cell interacting with $N-1$ others for the for the calculation of Eq.(5.29), while the full multi-centered geometry was retained in the calculation of pair-interactions of Eq.(5.28).

Note that the second term of Eq.(5.31) is the main cohesive term responsible for spinodal instabilities in the linear theory of Chapter 4, and, in the current theory, this term is contained in the second term of Eq.(5.29).

5.5 Results

Using the procedure outlined in Section 5.2, and using the values for the cell radius as derived in Sections 5.3, we have calculated the effective charge. In Figure 5.7, the charge $Z^\star$ of the effective system effective system is shown as a function of packing fraction and screening for typical parameters for a colloidal system of $Z = 1000$ and $a/\lambda_{\rm B} = 100$.

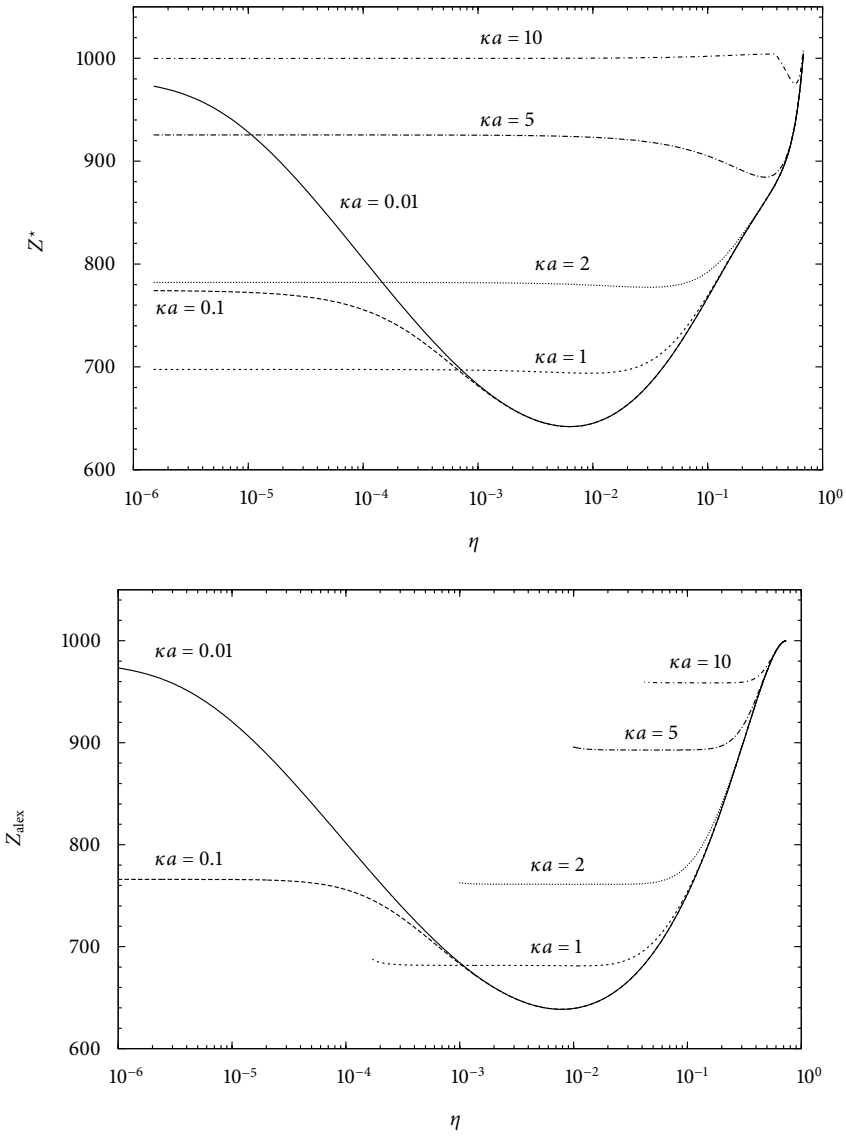

FIGURE 5.7 — The top figure shows the effective charge $Z^\star$ of the presented model as a function of the packing fraction η for several different screening constants κa. The bottom figure shows the Alexander effective charge for the same parameters. All calculations were done for a system with a bare charge $Z = 1000$ and colloidal radius $a = 100\lambda_B$. Note that for low salt concentrations $\kappa a \leq 2$, the agreement between the two models is very good. For higher salt concentrations, the two models agree somewhat less satisfactory, with Alexander's cell model predicting a monotonic increase of the effective charge as a function of the density and out model predicting a shallow minimum.

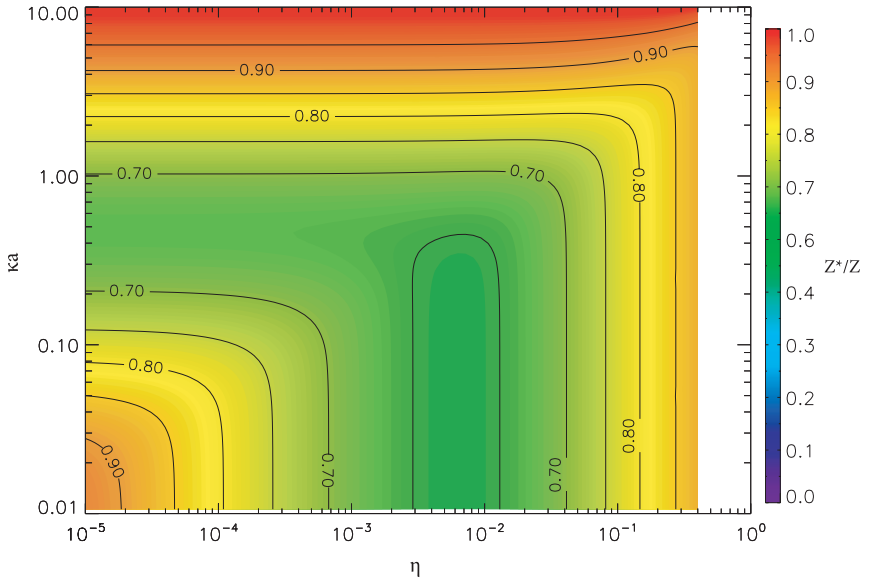

FIGURE 5.8 — The effective charge for a typical colloidal system with charge $Z = 1000$ and radius $a = 100\lambda_B$ as a function of the packing fraction η and the screening parameter κa. The colors and the contours indicate the effective charge $Z^\star/Z$. Note the recharging as a function of η at low κa, as also displayed in Fig. 5.7.

For comparison, Alexander's effective charge for the same system [83, 92] is displayed in the bottom part of the figure; this was calculated in a spherically symmetric, charge neutral cell. Note that for $\kappa a > 1$, we did not calculate the renormalized charge at low packing fractions in Alexander's cell model, as the precision required to solve the nonlinear Poisson–Boltzmann equation for cells with radii of more than a few Debye lengths is exceedingly time consuming on modern-day PCs.

The top figure shows that both in the limit $\kappa a \gg 1$ of high screening and in the limit $\eta \to 0.74$ of close packing of the colloids, the charge $Z^\star$ is equal to the bare charge Z of the colloid. This corresponds to the limits in which the cell radii b become equal to the colloid sizes a (see for example Figure 5.4, where the optimal cell radii are plotted for a system with very similar parameter as the one we are considering here), and thus the model reduces to the linear Poisson–Boltzmann theory of Chapter 4. Notable is also, that for low screening ($\kappa a \ll 1$), the effective charge shows a clear minimum of $Z^\star \approx 640$ at $\eta \approx 0.01$, independent of κa. This feature is not specific to our model, but is also present in more traditional, Wigner–Seitz-cell theories, such as Alexander's cell model [83, 92], which we reviewed in Chapter 3, and for which the renormalized charge is plotted in the bottom of Fig. 5.8.

The results for the effective charge as shown in the top figure are quite con-

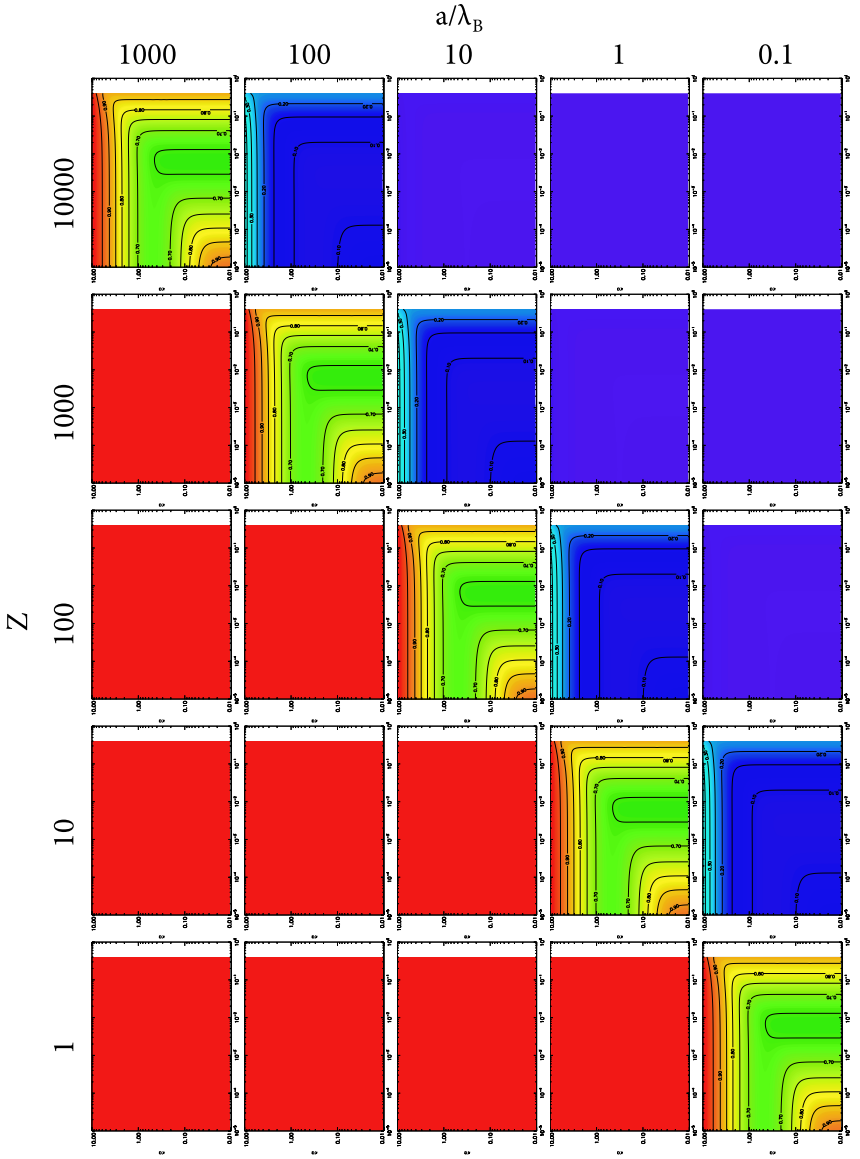

FIGURE 5.9 — The effective charge $Z^\star/Z$ in the Z–a/λ_B plane. The scale and color-coding of each of the diagrams is identical to those of Fig. 5.8, but each diagram shows data for for a different charge Z and radius a/λ_B. It is very clear from this figure that for $Z\lambda_B/a \leq 1$ the effective charge is equal to the bare charge, while for $Z\lambda_B/a \geq 10$, the effective charge is much lower than the bare charge, i.e., $Z^\star \ll Z$.

sistent with the results for the Alexander renormalized charge as displayed in the bottom figure. The agreement between the two figures is very good for low screening $\kappa a < 2$. For somewhat higher screenings, the two charges are still in reasonable agreement; in the low density limit at $\kappa a = 5$, for example, our model predicts $Z^\star = 915$, while the cell modes gives $Z^\star = 890$. The qualitative behavior at high screening shows a somewhat different behavior between the two models, with our new model still displaying a weak minimum, and the cell model predicting a monotonically increasing renormalized charge as the density increases.

The charge of the effective system is shown in a larger context in Figure 5.9. There, we have plotted the effective charge as a function of the packing fraction η and the screening κa for a large number of different values of the colloidal charge Z and radius a/λ_B. For easy comparison between the different figures, the effective charge has been normalized on the colloid charge, so the plotted quantity is $Z^\star/Z$. We notice immediately the huge decay of the effective charge in the diagonal direction: in the top-left (where $Z \sim 1$ and $a/\lambda_B \sim 10^4$), the effective charge is simply equal to the physical charge of the colloid; in the colloidal regime, where $Z\lambda_B/a \sim 1$, some renormalization starts to take place, and when $Z\lambda_B/a > 100$, the effective charge is almost negligible compared to the bare charge of the colloids.

We calculate the free energy of our system from the Hamiltonian (5.17)–(5.19) and (5.28) by exploiting the Gibbs–Bogoliubov inequality (see Appendix C). Because of its extensive character, the free energy can be written as $F(N, V, c_s) = Vf(n, V, c_s)$, with $f(n, V, c_s)$ the free energy per unit volume. The chemical potential $\mu = (\partial F/\partial N) = (\partial f/\partial n)$ and the pressure $P = -(\partial F/\partial V) = n\mu - f$ then follow easily, and the inverse compressibility is given by $\chi^{-1} = (\partial \beta P)/(\partial n) = n(\partial^2 f)/(\partial n^2)$. We exploit the usual conditions for chemical and mechanical equilibrium

$$\begin{cases} \mu(n^{(1)}) = \mu(n^{(2)}) \\ P(n^{(1)}) = P(n^{(2)}) \end{cases} \tag{5.32}$$

to find densities $n^{(1)}$ and $n^{(2)}$ of two phases in equilibrium. This allows us to calculate phase diagrams.

The phase-behavior of the presented theory is shown in the meta-phase diagram Fig. 5.10. In that figure, the instability regions (i.e. the regions where the compressibility is negative) are shown in blue. Additionally, in red, the instability regions are drawn if instead of the correction term as calculated in Section 5.4.1, the additional spherical approximation of Appendix B is used. Note that both versions of the theory indeed give rise to large spinodal instabilities, but that the area where instabilities occur shifts to lower couplings (higher temperatures) if the extra spherical approximation of Appendix B is used. This is most probably an artifact of the approximation; we will therefore, in the remainder of this chapter, focus on the Hamiltonian as calculated in Section 5.4.1.

Using the procedure outlined above, we also calculate full phase diagrams. The insets of Fig.5.11 show two typical examples, where the upper left corner (small Z,

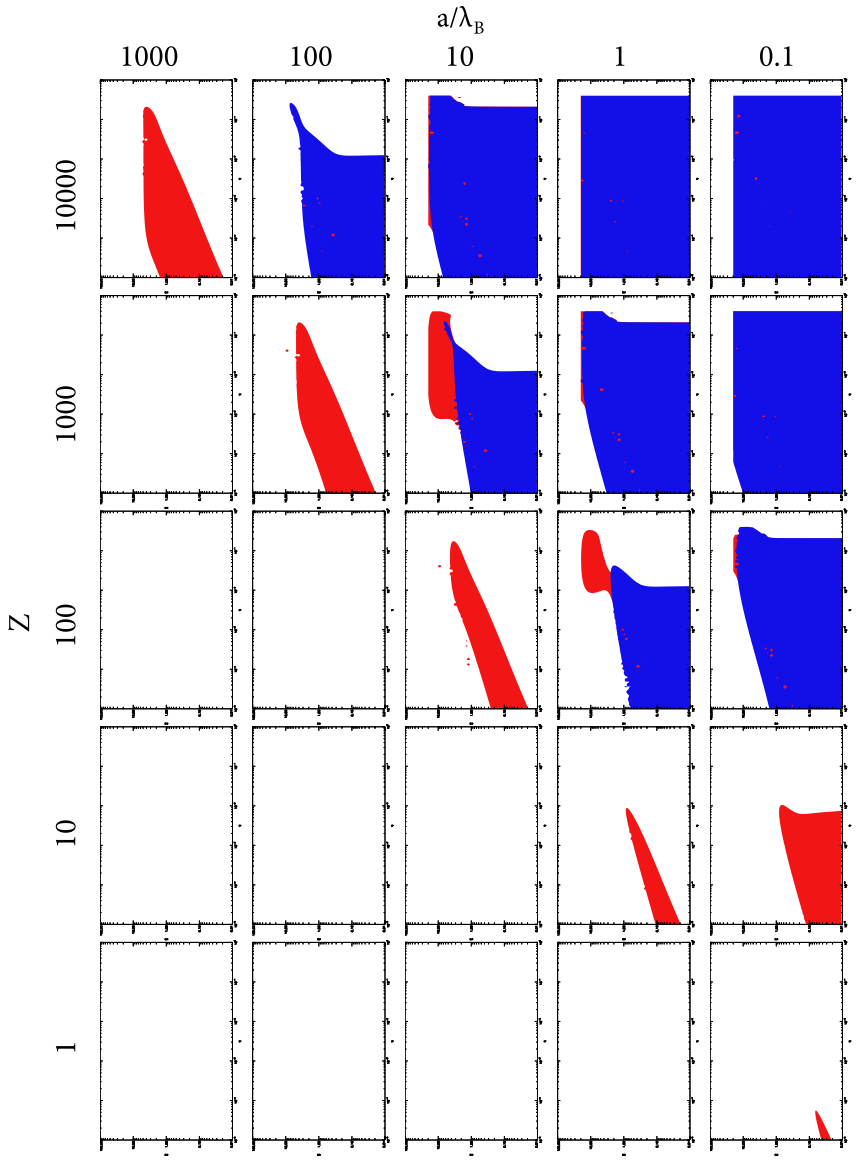

FIGURE 5.10 — Each of the figures shows, for a different value of Z and a/λ_B, the regions of spinodal instabilities (i.e. the regions where $\chi^{-1} < 0$) in blue. The red colors denote the instability regions of the theory where we use an additional spherical approximation for the correction term $\delta\Omega$, as calculated in Appendix B. It is clear that instabilities are present in a large part of parameter space. The instabilities are stronger, and are present for lower couplings (higher temperatures) if the additional spherical approximation is used. Note that in the lower-right part diagram, the blue and red regions overlap almost completely.

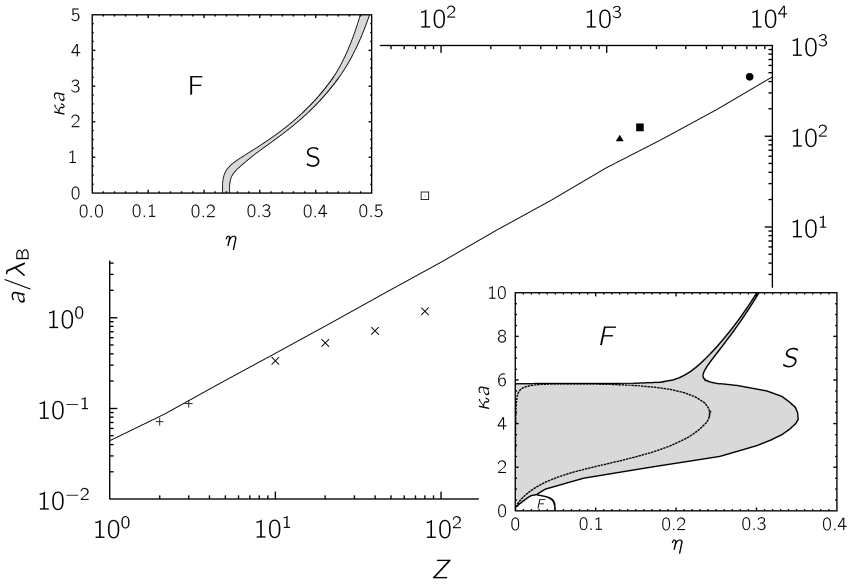

FIGURE 5.11 — Typical $\eta - \kappa a$ phase diagrams (insets) and critical line $Z\lambda_B/a \sim 25$ (main figure), as determined over many decades of the parameters by the present theory, for suspensions of charged colloids (charge $-Ze$, radius a, packing fraction η) in osmotic contact with a 1:1 electrolyte of reservoir screening constant κ and Bjerrum length λ_B. The critical line separates the strong-coupling regime (lower right) *with* a spinodal gas–liquid instability (dashed line) and a large density gap (grey area) at fluid–solid coexistence for low κa from the low-coupling regime (upper left part) *without* spinodal instability and with only a narrow density gap at fluid–solid coexistence. Criticality as found in the primitive model simulations of Refs. [118] and [78] are indicated by × and +, respectively, the simulated state point of Ref. [127] without an instability is indicated by □, and the experimental systems in which evidence for large density gaps at gas-liquid and gas-crystal coexistence was found are indicated by ▲ [122], ■ [49], and ● [51].

large a/λ_B) only shows crystallization with a narrow density gap, and the opposite corner (large Z, small a/λ_B) exhibits a spinodal instability at low κa and hence a large density gap between the coexisting phases. From many such phase diagrams, we constructed the curve in the Z–a/λ_B plane of Fig.5.11, below which a spinodal instability is present in the η–κa plane. This curve is well approximated by $Z\lambda_B/a = 25$ over many decades.

The parameters of several experiments in which alleged phase-instabilities are denoted by the filled symbols in Fig. 5.11. Not that these parameters are reasonably close to, yet above, our predicted critical line. The system that was studied by Monte-Carlo simulations by Hynninen [127], and which did not display any instabilities in the computer experiments, is shown as the open square.

Our critical line also shows good agreement with the salt-free primitive model

simulations of Refs. [118] (×) and [78] (+). That our critical line is at slightly weaker coupling than predicted by the salt-free simulations of Ref.[118] is consistent with the lower-right inset of Fig.5.11, where the instability is found for $1 \lesssim \kappa a \lesssim 6$, and not for the salt-free case $\kappa a = 0$.

Note furthermore that for $Z = 1$, our model predicts a critical point at $a/\lambda_B \approx 0.06$. This value is close to the well-known critical point of the symmetric 1:1-electrolyte at $T^* = 2a/\lambda_B = 0.057$ [75, 76], as discussed in Section 1.6. Given that we have employed many approximation techniques that are more appropriate for colloidal mixtures than for the Restricted Primitive Model (RPM), it is not surprising that the critical point of the 1:1-electrolyte is not exactly reproduced. However, the fact that we find the right order of magnitude for the critical point, suggests that the phase-instabilities of the colloidal systems are of the same physical origin as the well-established instabilities found in Debye–Hückel theory. While those are only found at low temperatures, it seems that in colloidal systems, through the much larger charge and sizes, these instabilities can be lifted to much higher temperatures, possibly even room temperature.

5.6 Conclusion

We have constructed a novel theory for colloidal suspensions, which interpolates between two widely used approximations: the linear Poisson–Boltzmann theories and Wigner–Seitz-type cell theories. We have shown that the effective charge of the presented theory are in good agreement with those predicted by Alexander's cell model of Ref. [83]. Also, we find that, for high enough charges and low enough temperatures ($Z\lambda_B/a \gtrsim 25$), the proposed theory results in spinodal instabilities, that can possibly explain phase-instabilities that have been observed in experiments. The theory also gives the critical point of the 1:1-electrolyte in good approximating, connecting explicitly DLVO-like theories with the Debye–Hückel theory.

CHAPTER 6

Charge regulation in the Poisson–Boltzmann cell model

Abstract

By combining Poisson–Boltzmann theory for colloidal suspensions with a chemical equilibrium between ions at the surface of the colloidal particles and free ions in the solvent, we study charge regulation in the Poisson–Boltzmann cell model. This chapter extends similar studies [128, 129], which confined themselves to small portions of the parameter space. We derive the bare charge of the colloid as a function of the colloidal packing fraction, the Debye length, the density of ionizable sites on the colloid surface and the particle size, and we study the effective charge as a function of the total number of ionizable sites.

6.1 Introduction

In an aqueous environment, macroscopic particles, for example silica particles or poly(*n*-butyl methacrylaat) (PBMA) core-shell latex particles, acquire a charge because of the chemical equilibrium between ions bound to the colloid's surface and free ions in solution. Although there has been much attention lately for these systems of charged colloidal particles, most theoretical models focus on particles with a fixed charge.

Although some studies of charge regulation effects exist [128, 129], the main focus of those was on the dependence of the charge and effective charge on the total number of ionizable groups on the colloid surface. The dependence of the charge on other system parameters is underexposed in those studies.

Suspensions of particles with a *fixed* charge are often described by Poisson–Boltzmann theory. The system is assumed to be at constant temperature T and to

be in diffusive equilibrium with a reservoir containing a concentration c_s of ionic salt pairs. The main quantity that needs to be found to describe the Hamiltonian and the free energy is the (dimensionless) electric potential $\phi(\mathbf{r})$; it is determined by the Poisson–Boltzmann equation (as derived in Chapter 2)

$$\nabla^2\phi(\mathbf{r}) = 8\pi\lambda_B c_s \sinh\phi(\mathbf{r}) \tag{6.1a}$$

$$\mathbf{n}_i \cdot \nabla\phi(\mathbf{r}) = Z\lambda_B/a^2, \tag{6.1b}$$

where $\lambda_B = e^2/\epsilon k_B T$ is the Bjerrum length, with $-e$ the electron charge, ϵ the electric permittivity of the solvent and k_B Boltzmann's constant. Here, $\mathbf{n}_i$ denotes the normal vector on the surface of colloid i.

In Chapter 5, we solved this multi-centered, non-linear Poisson–Boltzmann equation for fixed charges, and in Chapter 7 we will study the multi-centered non-linear problem under charge regulation conditions as described above. For now, we focus on the charge regulation in an Alexander-type cell model [83]. The Poisson–Boltzmann equation is solved by dividing the system into Wigner–Seitz cells and approximating each cell as a charge-neutral sphere of radius $R = a(\eta_{\max}/\eta)^{1/3}$, where a is the colloid radius, η the packing fraction of the system, and $\eta_{\max} \approx 0.74$ is the packing fraction of a close-packed crystal [97]. In this approximation, the problem (6.1a)–(6.1b) becomes one-dimensional and can be conveniently solved on a computer. The electric potential far away from the colloidal surface is then, in very good approximation, of Yukawa form, and by fitting this approximated potential to match the real potential at the cell boundary and extrapolating this Yukawa potential to the colloid surface, the effective charge and screening length can be defined (see Section 3.2). The same effective charge is also assumed to govern the pair-interaction between two particle; because of the charge-neutral nature of the cells, this pair potential can, however, not be calculated explicitly within the cell model.

Although this Alexander-type cell model has been very successful in describing such phenomena as the effective charge and the non-linear screening of colloids by counter-ions (see Chapter 3), it does not describe the chemical equilibrium between the colloid surface and the suspended ions, and the resulting dependency of the colloidal charge on system parameters such as the particle densities or the concentration of added salt.

Typically, colloidal particle have ionizable groups at the surface, which can dissolve in the background solvent (water, ethanol, etc.), causing the colloidal surfaces to become charged. These groups can, for example, be organic acid groups, (i.e., ionization through the reaction $-\mathrm{COOH} \rightleftharpoons -\mathrm{COO}^- + \mathrm{H}^+$), but any other type of binding or dissociation is in principle allowed. We do assume here, however, that there is only a single species of positive ions is our system, i.e., that the positive salt ions are the only species binding to, or being released from, the colloidal surfaces.

There have been some studies of this dynamical colloidal charge: Nimham and Parsegain calculated the equilibrium between charged plates and a salt reservoir in Ref. [130]. However, they did not generalize their model to a system of spherical

particles. Von Grünberg in Ref. [128] describes a numerical method to find the charge, but does not describe the dependence of the charge on system parameters like salt concentration and packing fraction.

In the current chapter, we try to give a clear and simple derivation of the dynamical colloid charge from microscopic first principles. We then make a connection with chemical and experimental quantities such as the dissociation constant; we continue to calculate the grand potential and in the final section present results for the bare and effective charges of the colloids, as well as the chemical potential, pressure, and compressibility of the systems as functions of the system parameters.

6.2 The model

We consider a system volume V, containing N colloidal particles with density $n = N/V$ in a continuous background solvent, which is characterized by its Bjerrum length λ_B. The system is in chemical equilibrium with a salt reservoir of temperature T, containing oppositely charged, monovalent, point-like salt ions, each of concentration c_s. We assume that the colloidal particles are spherically symmetric and that each particle has M ionizable groups, which are homogeneously distributed over the surface. One of the problems at hand is to determine the (average) number Z of ionized groups (and the number of associated groups $M - Z$).

Following the approach of Chapter 3, we write the functional $\Omega[\rho_\pm(r), Z]$ for the grand potential of a single cell as

$$\begin{aligned}\beta\Omega[\rho_\pm(r), Z] = &\sum_\pm \int \mathrm{d}\mathbf{r}\, \rho_\pm(r) \left[\ln \frac{\rho_\pm(r)}{c_s} - 1\right] + \beta F_s(M, Z) \\ &+ \frac{1}{2} \int \mathrm{d}\mathbf{r}\, [\rho_+(r) - \rho_-(r) + q(r)]\, \phi(r),\end{aligned} \tag{6.2}$$

This first term, denoting the entropy of the micro-ions in the cell, and the last term, denoting the electrostatic interactions between the constituents of the cell, are identical to the two terms of the functional (3.9) for the Poisson–Boltzmann model with a fixed charge, with $q(r) = (-Z/4\pi a^2)\delta(r - a)$. The electrostatic potential $\phi(r)$ was defined in Eq. (2.12). The second term of Eq. (6.2) is new here, compared to the grand potential (3.9) of the fixed-charge cell model, and describes the non-electrostatic part of the free energy of the surface of the colloids. It is given by the simple expression

$$\beta F_s(M, Z) = -\ln \binom{M}{Z} + Z\beta E, \tag{6.3}$$

where the first term is the entropy of Z sites out of a total of M being ionized, and E denotes the ionization free energy of each of the M sites on the colloidal surface.

The minimum conditions for the functional (6.2) with respect to the ion densities are

$$0 \equiv \frac{\delta\beta\Omega}{\delta\rho_\pm(r)} = \ln\frac{\rho_\pm(r)}{c_s} \pm \phi(r), \tag{6.4}$$

which directly leads to the usual Boltzmann relation $\rho_\pm(r) = c_s \exp[\mp\phi(r)]$. Combining this with Poisson's equation (2.13), gives the Poisson–Boltzmann equation in the cell

$$\frac{1}{r^2}\frac{\partial}{\partial r}\left[r^2\frac{\partial}{\partial r}\phi(r)\right] = \kappa^2 \sinh[\phi(r)] \tag{6.5a}$$

$$\phi'(a) = Z\frac{\lambda_B}{a^2}; \quad \phi'(R) = 0. \tag{6.5b}$$

Note that the first boundary condition here still depends on the unknown charge Z.

By substituting the minimum conditions (6.4) back into the functional (6.2), we find the equilibrium grand potential functional (cf. Eq. (3.10))

$$\begin{aligned}\beta\Omega'[Z] =& 4\pi c_s \int_a^R \mathrm{d}r\, r^2 \{\phi(r)\sinh\phi(r) - 2\cosh\phi(r)\} \\ &- \frac{Z}{2}\phi(a) + \beta F_s(M,Z).\end{aligned} \tag{6.6}$$

which is still a function of the colloid charge Z through the surface term βF_s. The first term of this expression includes the electrostatic and entropic contributions of the micro-ions; the second term is the electrostatic energy of the colloidal surfaces (due to both its self-interaction and to the interactions with the micro-ions in solution); the third term is the surface's entropy and binding free energy.

To find the equilibrium value for the net charge, we have to minimize $\Omega'[Z]$ with respect to Z. The associated minimum condition is given by

$$\begin{aligned}0 \equiv \frac{\mathrm{d}\beta\Omega'}{\mathrm{d}Z} = \frac{\partial\beta\Omega'}{\partial Z} + \int \mathrm{d}\mathbf{r}\Bigg\{&\frac{\delta\beta\Omega'}{\delta q(\mathbf{r})}\frac{\mathrm{d}q(\mathbf{r})}{\mathrm{d}Z} \\ &+ \frac{\delta\beta\Omega'}{\delta\rho_+(\mathbf{r})}\frac{\mathrm{d}\rho_+(\mathbf{r})}{\mathrm{d}Z} + \frac{\delta\beta\Omega'}{\delta\rho_-(\mathbf{r})}\frac{\mathrm{d}\rho_-(\mathbf{r})}{\mathrm{d}Z}\Bigg\},\end{aligned} \tag{6.7}$$

By definition of $\Omega'[Z]$ as the minimum of $\Omega[\rho_\pm(r), Z]$ with respect to the densities $\rho_\pm(r)$, the derivatives of $\Omega'[Z]$ with respect to the ion densities are zero, and therefore the last two terms in the integrand on the right hand side of expression (6.7) vanish. Using that $\mathrm{d}q(r)/\mathrm{d}Z = -\delta(r-a)/4\pi a^2$, and Stirling's approximation for the logarithmic binomial in $F_s(M,Z)$, we thus find that

$$\ln\frac{Z}{M-Z} = \phi(a) - \beta E \qquad \text{or} \qquad Z = \frac{M}{1+\exp[\beta E]\exp[-\phi(a)]}. \tag{6.8}$$

Note that the colloidal net charge thus depends on the value of the electric potential at the surface, and that hence the coupled set of equations (6.5a), (6.5b), and (6.8) has to be solved to find the electric potential $\phi(r)$ and the charge Z for fixed M, λ_B, κ, a and R.

6.3 Chemical equilibrium

We have now expressed the charge Z in terms of the binding free energy βE. Unfortunately, this binding free energy is not a convenient experimental parameter, and generally depends on the system parameters such as the solvent characteristics, the nature of the chemical groups and the reservoir salt concentration.

Therefore, we will now approach the problem of the dynamical charge from a slightly different viewpoint, and try to connect the binding free energy βE to the dissociation constant K, which is tabulated for many reactions.

For convenience, we denote the ionized surface groups by A^-, the positive ions that can bind to the surface by H^+, and the bound surface complex by AH. The dissociation constant K for the reaction $AH \rightleftharpoons A^- + H^+$ is then defined as

$$K = \frac{[A^-][H^+]}{[AH]} = \frac{\alpha}{1-\alpha}\rho_+(a), \tag{6.9}$$

where $[A^-]$, $[H^+]$ and $[AH]$ denote the concentrations at the colloidal surface of the ionized complexes, the positive salt ions, and the bound surface complexes, respectively. The variable $\alpha = Z/M$ is the fraction of binding positions that is ionized, and $\rho_+(a)$ is the concentration of positive ions at the colloidal surface. Typically in experimental setups, the dissociation constant K and the total titrated charge M are known.

Combining Eq. (6.9) and Boltzmann's relation $\rho_+(a) = c_s \exp[-\phi(a)]$ at the colloid surface, we find the net colloidal charge as a function of K and $\phi(a)$:

$$Z = \frac{M}{1 + (c_s/K)\exp[-\phi(a)]}. \tag{6.10}$$

Comparing this expression with Eq. (6.8), it is directly clear that the dissociation constant can be expressed in term of the dissociation free energy E and the salt concentrations as

$$K = c_s \exp[-\beta E] \tag{6.11}$$

or

$$\beta E = \ln \frac{c_s}{K} \tag{6.12}$$

This relation is plotted in Fig. 6.1 for PBMA ($K = 16\mu$M) [131] and silica particles ($K = 32$nM) [82] in water.

6.4 Free energy

According to the derivation in Section 3.3, the free energy of the system is given by

$$\frac{\beta F}{N} = \ln[n\mathcal{V}] - 1 + \Omega_c, \tag{6.13}$$

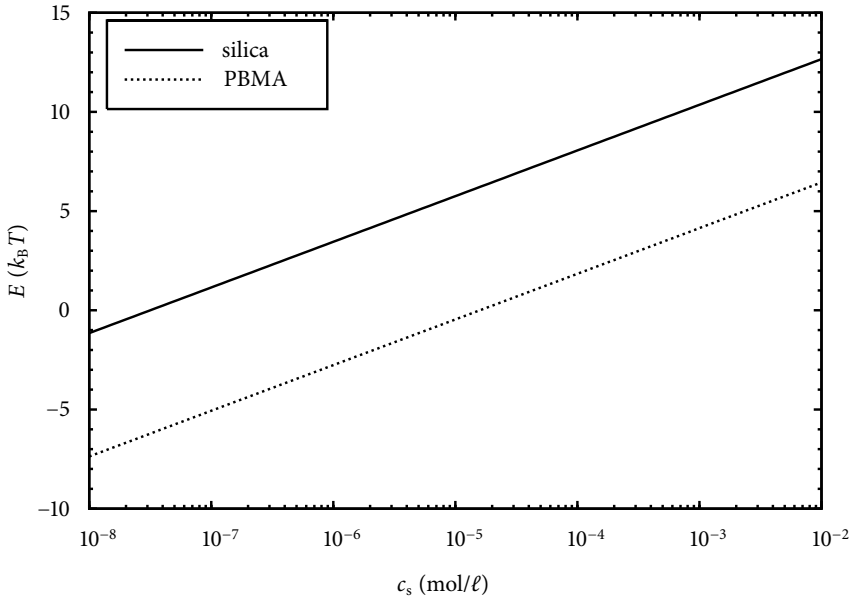

FIGURE 6.1 — The binding free energy of relation (6.11) plotted for the protonation reaction of silica and PBMA particles in water.

where Ω_c denotes the internal grand potential of a single cell, and is given by the minimum of $\Omega'[Z]$ as a function of Z. Combining Eqs. (6.6), (6.8) and (6.11), it can be written as

$$\begin{aligned}\beta\Omega_c =& 4\pi c_s \int_a^R \mathrm{d}r\, r^2 \big\{\phi(r)\sinh\phi(r) - 2\cosh\phi(r)\big\} \\ &+ \frac{Z}{2}\phi(a) - M\ln\left[1 + \frac{K}{c_s}\exp[\phi(a)]\right],\end{aligned} \tag{6.14}$$

where the charge Z is given by Eq. (6.10) and the electric potential $\phi(r)$ is the solution of the boundary value problem

$$\frac{1}{r^2}\frac{\partial}{\partial r}\left[r^2\frac{\partial}{\partial r}\phi(r)\right] = \kappa^2\sinh[\phi(r)]; \tag{6.15a}$$

$$\phi'(a) = \frac{\lambda_B}{a^2}\frac{M}{1 + (c_s/K)\exp[-\phi(a)]}; \tag{6.15b}$$

$$\phi'(R) = 0, \tag{6.15c}$$

which can be solved by numerical integration and a shooting method (see, e.g., Ref. [132]).

6.5 Results

6.5.1 The net charge Z

In Fig. 6.2, we show the charge Z as a function of the total number of binding positions at the surface for a fixed particle size $a = 100\lambda_B$ (top) and also for a variable particle size with a fixed (high) binding site density $\sigma = M/4\pi a^2 = 0.1\text{Å}^{-2}$ (bottom). For each curve, the colloidal packing fraction $\eta = 0.1$, the screening constant κa, and the dissociation constant K are fixed. From the top figure we notice that, at high screenings, the charge starts out increasing linearly with the total number of binding positions. For higher values of the surface charge density σ, the charge Z grows much slower as a function of σ. Note furthermore that, for low σ and low screening, we find that all positions at the colloid surface are ionized, i.e., $Z \to M$. In contrast, for high σ or high κa only a fraction $< 1\%$ of the surface sites is ionized. The behavior as a function of particle size at fixed σ, on the other hand, shows mainly a linear relation between Z and M (i.e., $Z \propto a^2$). The proportionality factor in this regime is mainly dependent on the particle density (which is not shown in this figure, see below), and, only for low packing fractions, also on the screening. For small particle sizes, this linear relation breaks down, and the charge is lower than expected. This is due to the non-linear relation (6.15b) between $\phi(a)$ and $\phi'(a)$, which becomes more pronounced for small a and large c_s.

In Fig. 6.3, the colloid charge Z is shown as a function of the dissociation constant K for different values of the screening constant κa, and at fixed packing fraction $\eta = 0.1$, colloid size $a = 100\lambda_B$ and $M = 10^6$. Note that the dependence of the charge on the screening constant κa becomes much more pronounced as the dissociation constant is lower. This will be quantified below, where we will compare the dependence of Z on κa and η for silica particles ($K = 32\text{nM}$) and PBMA particles ($K = 20\mu\text{M}$).

In Fig. 6.4, the charge for PBMA particles (top figure) and silica particle (bottom figure) is plotted as a function of the colloid packing fraction η and the screening constant κa. Note that the color coding in the two figures is different. In both figures, the transition from salt-dominated systems at low packing fractions and high reservoir salt concentrations to counter-ion dominated systems at high densities and low screening is clearly visible. Note, though, that the PBMA particles in the top figure tend to remain charged at much higher densities and salt concentrations than the silica particles: while, for a screening constant $\kappa a = 0.01$, the PBMA particles still only have discharged from $Z \approx 1600$ at low densities to $Z \approx 1200$ at $\eta = 0.1$ (i.e., a discharging of approximately 25%), the silica particles have discharged from $Z \approx 800$ to $Z \approx 100$ (i.e., a discharging of 88%).

In Fig. 6.5, we show "slices" through the top diagram of Fig. 6.4, i.e., we have plotted the charge for PBMA particles as a function of the packing fraction η at fixed κa (top) and as a function of the screening κa at fixed packing fraction (bottom). Similar diagrams for silica particles, corresponding to the bottom figure of Fig. 6.4, are shown in Fig. 6.6. Note that, in the top diagrams of Figs. 6.5 and 6.6, some of the

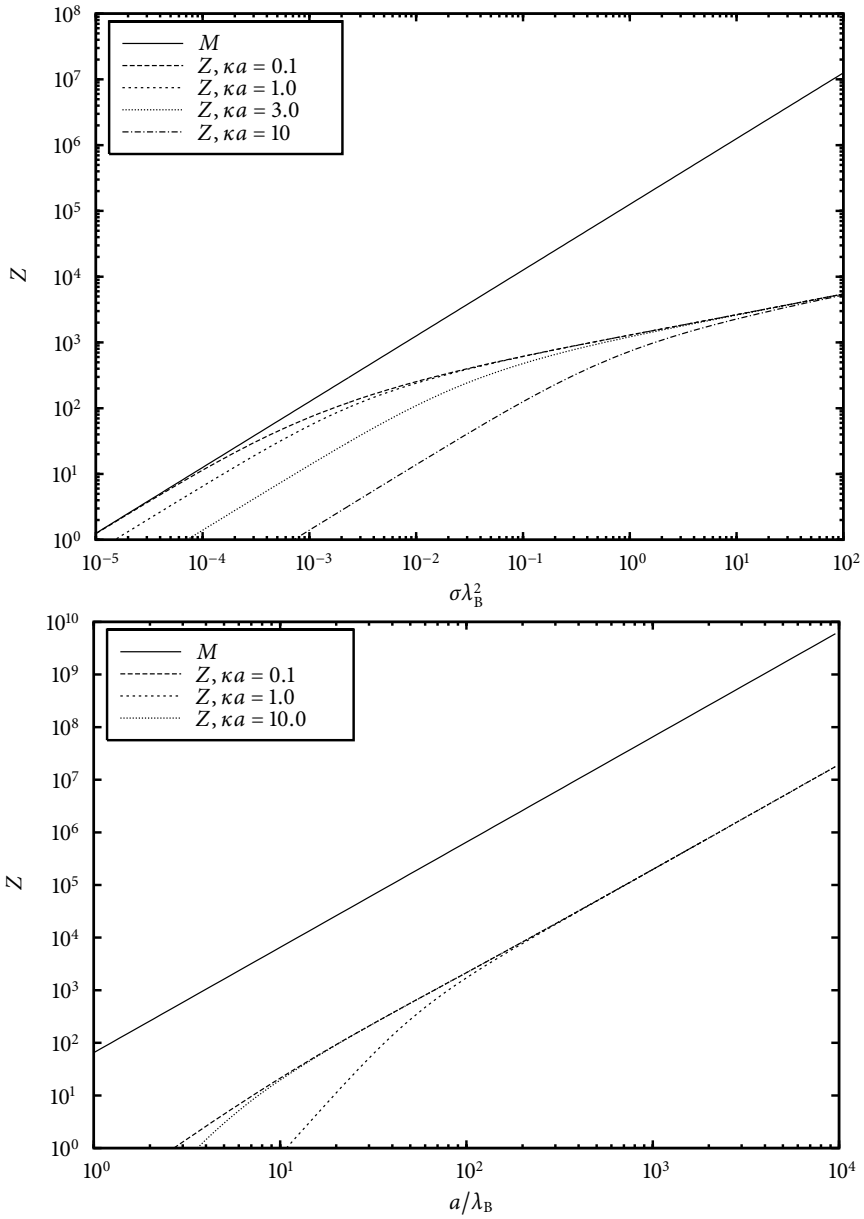

FIGURE 6.2 — Physical charge Z for PBMA particles as a function of the number of binding positions on the colloid at fixed packing fraction and screening constant. In the top figure, the particle size is kept constant at $a = 100\lambda_B$, while the density of binding positions on its surface $\sigma = M/4\pi a^2$ is varied, while in the bottom figure, the surface density is kept constant at 0.1Å^{-2} and the particle size is varied. In both figures, the packing fraction is $\eta = 0.1$. Note that the maximum physical surface charge density is of the order of $\sigma\lambda_B^2 \sim 1$; in the top figure, the charges have been plotted for charges densities up to $\sigma\lambda_B^2 = 100$ to show to convergence of the curves for different screening constants κa.

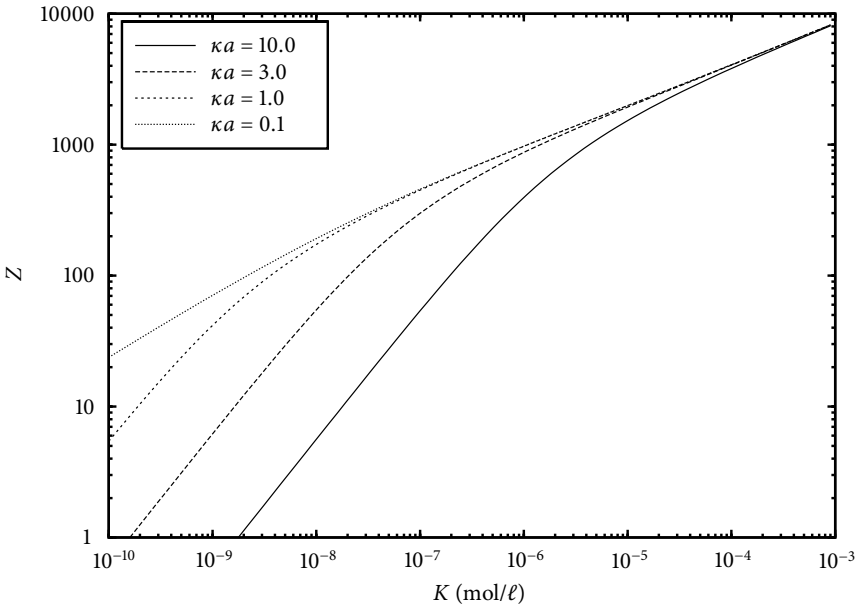

FIGURE 6.3 — The colloid charge Z as a function of the dissociation constant K, calculated at fixed particle size $a = 100\lambda_B$, number of binding positions $M = 10^6$ and colloidal packing fraction $\eta = 0.1$, for different values of the screening constant κa. Note the dissociation constant can vary greatly between different systems; for silica particles it is equal to $K_{\text{silica}} = 32\text{nM}$, while for PBMA particles, it is $K_{\text{PBMA}} = 20\mu\text{M}$.

curves are cut off at low packing fractions (i.e., large cells). This is because for large screening lengths and low densities, it is not possible to calculate the solution to the Poisson–Boltzmann cell problem: the precision needed is exceedingly large. To generate Figure 6.4, we have extrapolated the constant values of Z to low densities.

The top diagrams of Figs. 6.5 and 6.6 show that the charge of the particles depends very much on the packing fraction. Note however, that for PBMA particles, with a relatively high dissociation constant $K = 20\mu\text{M}$, the η-dependence of the charge is mainly relevant in the regime of relatively high packing $\eta > 0.1$, while for the silica particles (with a lower dissociation constant $K = 32\text{nM}$), the density-dependence of the charge is relevant in a much larger part of parameter space, especially for low salt concentrations.

The bottom diagrams of Figs. 6.5 and 6.6 show the dependence of the charge as a function of the screening κa for several fixed packing fractions. At low screening (very low salt concentration), the charge is constant as a function of κa, while for high salt concentrations, it drops off to zero, reducing the particles essentially to hard spheres without any Coulomb interactions. Note that the transition region where the charge starts to drop to zero, depends on the value of the dissociation

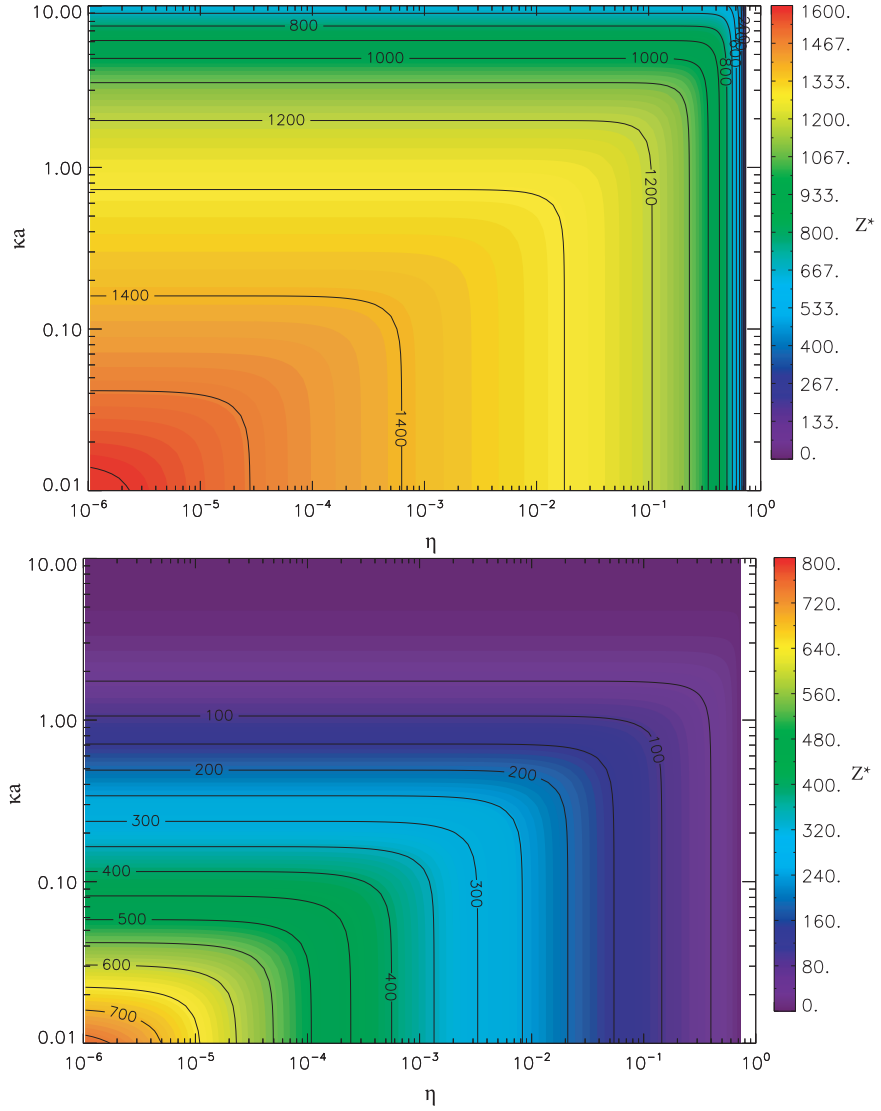

FIGURE 6.4 — The colloid charge Z as a function of the packing fraction and the screening constant for PBMA particles (top) and silica particles (bottom). In both figures, the particle sizes are fixed at $a = 100\lambda_B$, and the total number of ionizable sites per particle is $M = 10^5$. Note that the color codings in the two figures is different. The values for the charge at low densities and high salt concentrations were extrapolated from the values at the lowest densities (i.e., largest cells) we could calculate (see also the top figures of Figs. 6.5 and 6.6).

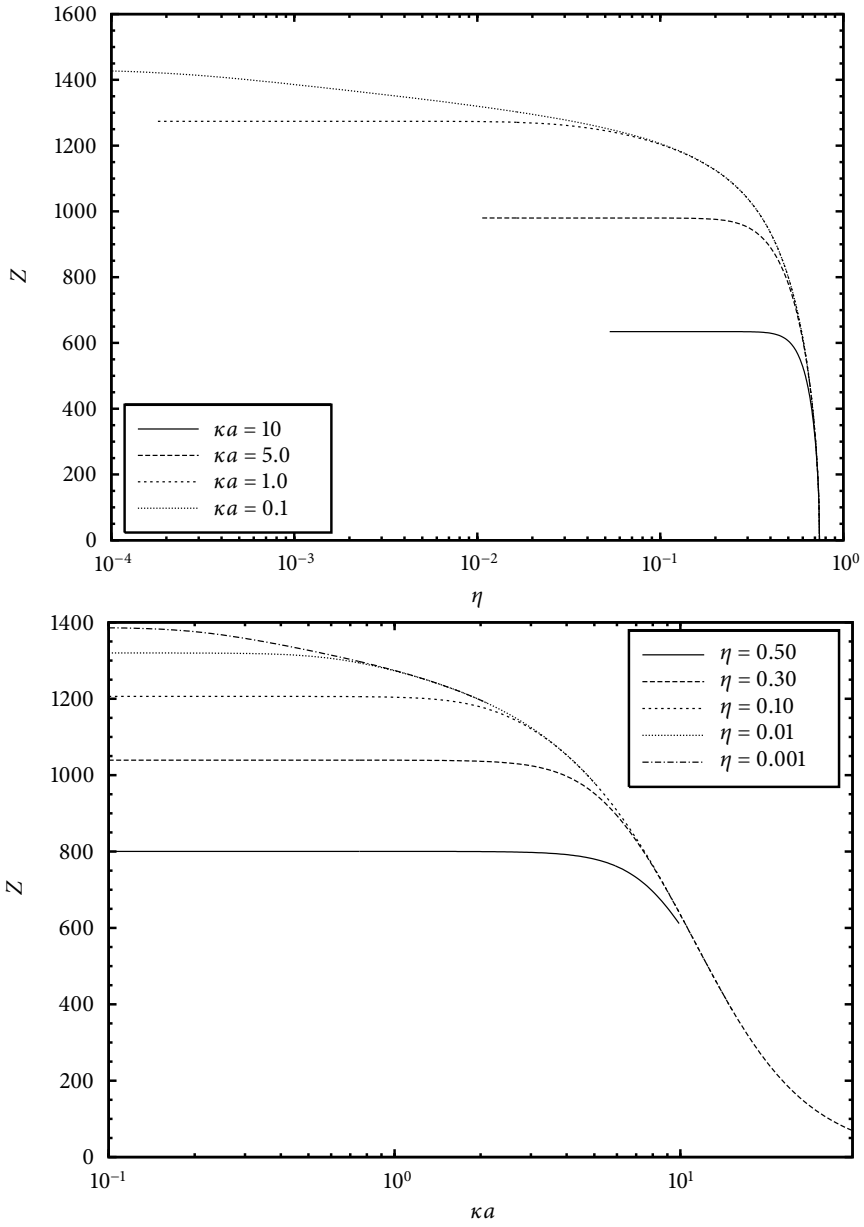

FIGURE 6.5 — The colloid charge for PBMA particles as a function of the packing fraction (top) and the screening constant (bottom). The colloid size is $a = 100\lambda_B$ and the maximum ionization number is $M = 10^5$. These figures correspond to the top diagram of Fig. 6.5.

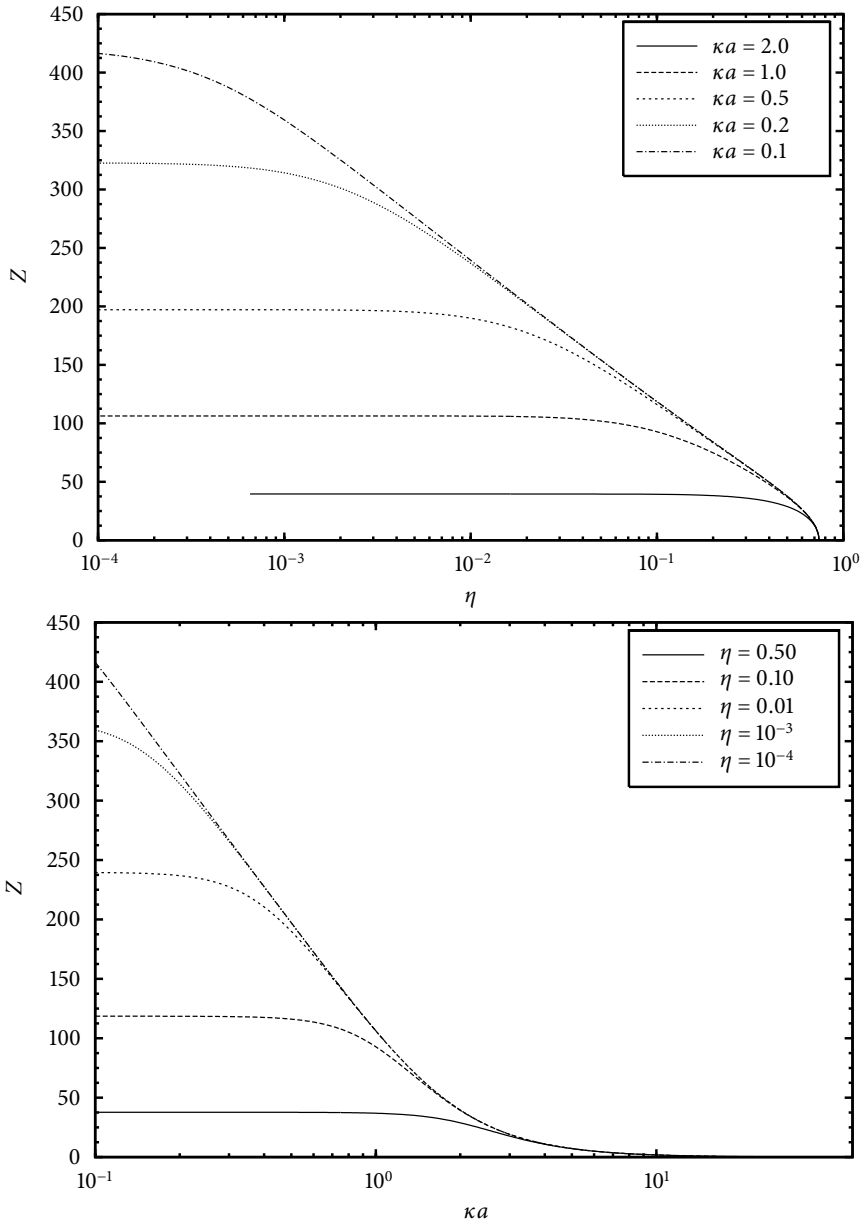

FIGURE 6.6 — The colloid charge for silica particles as a function of the packing fraction (top) and the screening constant (bottom). The colloid size is $a = 100\lambda_B$ and the maximum ionization number is $M = 10^5$. These figures correspond to the bottom diagram of Fig. 6.5.

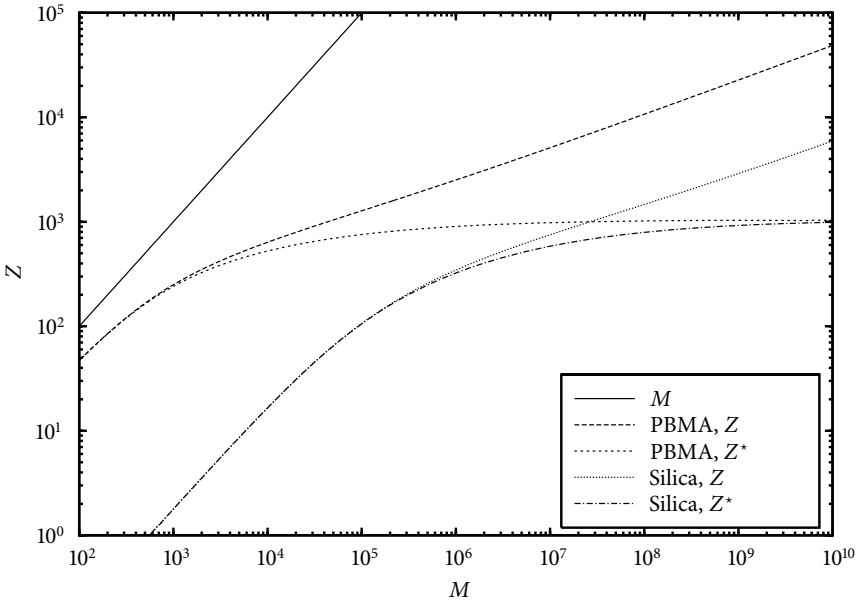

FIGURE 6.7 — The bare charge Z and the renormalized charge $Z^\star$ as a function of the number of ionizable sites M for PBMA and silica particles with a size $a = 100\lambda_B$, a fixed packing fraction $\eta = 0.1$ and $\kappa a = 1.0$. Note that the physical maximum charge for these particles is of the order of $M \sim 10^7$; the entire range up to $M = 10^{10}$ is shown here for a clearer view on the convergence of the renormalized charges for the two systems.

constant: for the PBMA particles, the steepest decay takes place for $\kappa a > 5$, while for the silica particles, the decay starts at much lower κa, and at $\kappa a = 10$, the particles are practically charge-neutral for any η.

6.5.2 The renormalized charge $Z^\star$

Far away from the colloidal surface, near the cell boundary, the electric potential $\phi(r)$ is also a solution of the linearized Poisson–Boltzmann equation, provided that the linearization point is chosen to be the potential $\phi(R)$ at the cell boundary. The potential $\phi(r)$ thus takes a Yukawa form, of which the prefactor can be utilized to define a renormalized (or 'effective') charge $Z^\star$ (see also Section 3.2). This effective charge is the charge that is observed when looking at the colloid from far away, and that is assumed to govern the pair interaction between two colloids at sufficient distance from each other. This procedure for charge renormalization is well established for a fixed bare charge Z (see Chapter 3 and Refs. [83, 92]). Here it is studied within a charge regulation scheme.

In Fig. 6.7, we plot this renormalized charge together with the bare charge for both PBMA and silica particles. The particles have a fixed size of $a = 100\lambda_B$, the

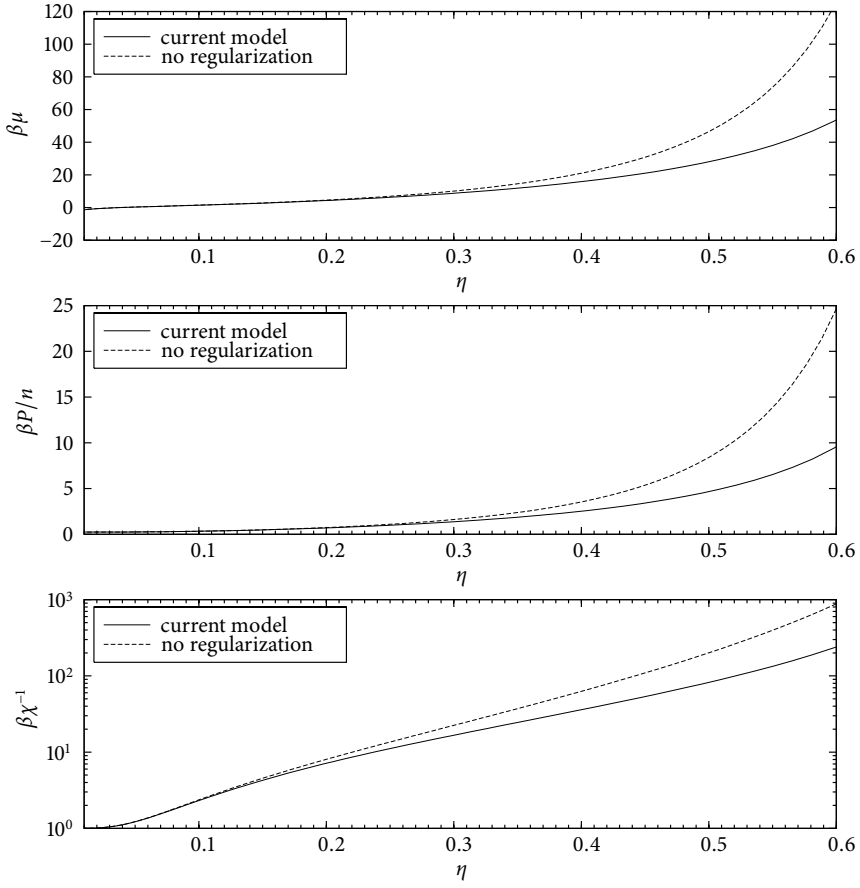

FIGURE 6.8 — The chemical potential (top), osmotic pressure (middle) and inverse compressibility (bottom) for the renormalized model (solid line) compared to that of the traditional cell model with a fixed charge (dashed line). The charge of the fixed system $Z = 39$ was chosen such, that in the low density limit $\eta \to 0$, it matches the charge of the regularized model. The other parameter in the system are $M = 10^5$, $a/\lambda_B = 100$, $\kappa a = 2.0$ and $K = 32$nM (silica).

colloidal packing fraction is $\eta = 0.10$ and the screening constant is $\kappa a = 1.0$. Note that, while the bare charges keep increasing as the total number of ionizable sites M increases, the effective charges saturate both to the same value of about $Z^\star \approx 1000$. Specifically, we observe that this saturated charge is independent of the dissociation constant K. This is consistent with recent articles by Trizac and Bocquet [95, 96].

In Fig. 6.8, we show the chemical potential (top figure), pressure (middle) and inverse compressibility of a system of silica particles of size $a = 100\lambda_B$, with $M = 10^5$ and $\kappa a = 2.0$. The solid lines shows these quantities for the current

charge-regulation model, while the dashed lines show a corresponding traditional Poisson–Boltzmann cell model with a fixed charge $Z = 39.85$, which was chosen such that it matches the charge of the current model in the low density limit $\eta \to 0$. The figure clearly shows, that for low densities (i.e., the region where the charges of the two systems match), the chemical potential, the pressure and the compressibility are (almost) equal. For larger densities, however, the charge of the regularized system drops, as depicted in Fig. 6.6, and the pressure, chemical potential and inverse compressibility for the regularized system are smaller than in the system with a fixed charge. This is consistent with recent findings by Biesheuvel [117].

6.6 Conclusion

We have studied a model to calculate charge regulation in the Poisson–Boltzmann cell model, and connected the surface binding free energy with the dissociation constant. Within this model, we have calculated the bare charge of the colloids as a function of a number of parameters, specifically the packing fraction, the screening parameter κa, the density of binding positions at the colloid surface and the particle sizes. The effect of charge regulation turns out to be quite significant. We also calculated effective charges and the chemical potential, osmotic pressure and compressibility of the model.

In principle, one could imagine a mechanism involving a trade-off between entropy on the colloid surfaces and electrostatic energy, resulting in spinodal instabilities. We have scanned large regions of parameter space, $0.01 < \kappa a < 10$, $10^{-6} < \eta < 0.7$, $0.1 < a/\lambda_B < 10^5$, and $1 < M < 10^7$, but found no such instabilities within the cell model approach.

However, in the context of multi-centered Poisson–Boltzmann theory, as derived in Chapter 5, where already significant spinodal instabilities are found, charge regulation, as described in this chapter, may be important. On the one hand, a decreasing charge as a function of the density, as we found here, corresponds to reduced repulsions or effective attractions and might therefore increase the instabilities found in the theory of Chapter 5. On the other hand, we have seen here, that the charge of the colloids is typically much less than the total number of ionizable sites on the colloids, and it might therefore be hard to find a regime in parameter space where the colloid charge is high enough to drive phase separations. This will be further investigated in Chapter 7.

CHAPTER 7

Charge regulation in multi-centered non-linear Poisson–Boltzmann theory

Abstract

We extend the multi-centered non-linear Poisson–Boltzmann model of Chapter 5 with the concept of charge regulation, which explicitly takes into account the chemical equilibrium between ions at the colloidal surface and free ions in solution.

7.1 Introduction

In Chapter 5, we have studied a model which contains both the non-linear charge-renormalization behavior of the Poisson–Boltzmann cell model of Chapter 3 and the multi-centered character of the linear theory of Chapter 4. This model seems to work rather well, and describes the phase-behavior of suspensions of charged colloids for a very large range of charges and colloid sizes, even down to the restrictive primitive model at $Z = 1$ and $a < \lambda_B$. It predicts spinodal instabilities for systems with $Z\lambda_B/a \gtrsim 10$–100 (see Fig. 5.11).

One major feature that is still missing from this multi-centered non-linear theory, is the concept of charge regulation. In Chapter 6, we described this effect, caused by a chemical equilibrium between ions bound to the colloidal surfaces and free ions in solution. In that chapter, we have shown that the charge of colloidal particles in suspension can vary greatly with system parameters such as the screening length and the colloid density.

In the current chapter, we will expand the multi-centered, non-linear Poisson–Boltzmann theory of Chapter 5 with the concept of charge regulation. We expect that this effect will be important for the phase behavior of colloidal suspensions: the charge regulation mechanism causes the colloidal particles to discharge as the density increases, thereby decreasing the repulsions between the colloids. This phenomenon could be interpreted as an effective attraction, reducing the spinodal stability of the suspension. On the other hand, the question is if the net charge of the colloids can remain high enough (i.e., $Z\lambda_B/a \gtrsim 25$) for the (spinodal) instabilities to occur in a charge regulation model. To check which one of these effects is dominant, we calculate the charge and the effective Hamiltonian for the multi-centered, non-linear Poisson–Boltzmann theory with charge regulation, and study the stability of colloidal suspensions by calculating the free energy and the compressibility.

We will base our theory on the multi-centered non-linear theory of Chapter 5, combine it with the charge regulation expressions derived in Chapter 6. This extension is not very hard: we only need to introduce extra surface terms in the effective Hamiltonian. These surface terms are very localized and do therefore not interfere with the general structure of the model of Chapter 5. Moreover, the non-regulated model, already involves solving a spherically-symmetric Poisson–Boltzmann equation, which we have seen in Chapter 6 to be exactly what is needed to include charge regulation in a Poisson–Boltzmann type theory.

7.2 The model

Like in Chapter 5, we consider a suspension of N hard, spherical colloids of radius a, mass m, density $n = N/V$ in a continuous background solvent, which is characterized by the Bjerrum length $\lambda_B = e^2/\epsilon k_B T$, with $-e$ the electron charge, k_B Boltzmann's constant and T the temperature. The charge of the colloid is denoted by Z, but, unlike the charge in Chapter 5, is now no longer fixed, but rather a dynamical variable. The system is assumed to be in diffusive equilibrium with a salt reservoir, which contains oppositely charged, monovalent, point-like salt ions, each with density c_s. This gives rise to (yet to be determined) concentrations $\rho_\pm(\mathbf{r})$ of positive and negative ions in the suspension.

Like in the Wigner–Seitz cell charge regulation theory of Chapter 6, we assume that each particle has M homogeneously distributed ionizable groups on its surface, Z of which are assumed to be ionized. Due to the ionization of the colloidal surface, each colloidal surface gains an energy $F_s(M,Z)$, given by

$$\beta F_s(M,Z) = -\ln\binom{M}{Z} + \beta E, \tag{7.1}$$

where the first term denotes the entropy of occupying Z out of M binding positions and E is the binding free energy of each ion. In Chapter 6, we derived that this binding free energy is related to the dissociation constant K of the ionization process as $\exp[\beta\epsilon] = c_s/K$.

The effective interaction Hamiltonian, as defined in Eq. (2.8), now takes the form (cf. Eq. (2.10))

$$\begin{aligned}\beta H(\{\mathbf{R}_i\};) = &\sum_{\alpha=\pm}\int \mathrm{d}\mathbf{r}\,\rho_\alpha(\mathbf{r})\left[\ln\frac{\rho_\alpha(\mathbf{r})}{c_\mathrm{s}}-1\right]\\ &+\frac{1}{2}\int \mathrm{d}\mathbf{r}\,\left[\rho_+(\mathbf{r})-\rho_-(\mathbf{r})+q(\mathbf{r})\right]\phi(\mathbf{r})\\ &+\sum_{\alpha=\pm}\int \mathrm{d}\mathbf{r}\,\rho_\alpha(\mathbf{r})\beta U_\alpha^{\mathrm{HC}}(\mathbf{r})+N\beta F_\mathrm{s}(M,Z),\end{aligned} \tag{7.2}$$

where $q(\mathbf{r})$ denotes the charge distribution of the colloids as defined by Eq. (2.11), $\phi(\mathbf{r})$ is the dimensionless electric potential, as defined in Eq. (2.12), and $\beta U_\pm^{\mathrm{HC}}(\mathbf{r})$ describes the hard-core interaction between the colloids and the micro-ions. In Eq. (7.2), we have neglected any fluctuations in the colloid charge Z and we have assumed that all colloids carry exactly the same charge. Note that the Hamiltonian (7.2) is a functional of the ionic profiles $\rho_\pm(\mathbf{r})$ and a function of the colloid charge Z.

Following the procedure outlined in Chapter 5, we construct virtual cells of radius $b > a$ and (yet unknown) net charge Q around each colloid. Inside the cell, we solve a non-linear Poisson–Boltzmann cell equation, while in the regions outside the cell, we assume the system is well described as particles of radius a and effective charge $Z^\star$, and use a linear, multi-centered approximation to the electric potential.

Because the surface free energy of the system (7.1) does not depend explicitly on the micro-ion profiles $\rho_\pm(\mathbf{r})$, the minimization procedure of the effective Hamiltonian (7.2) with regard to the salt concentrations, carries though exactly as the minimization procedure in Section 5.4. We thus find that outside the cells, the electric potential, which we denote by $\phi_\ell(\mathbf{r})$, is the solution of the linear Poisson–Boltzmann equation (5.2), and is given by

$$\phi_\ell(\mathbf{r}) = \bar{\phi} - \tanh\bar{\phi} + \sum_{i=1}^{N}\phi_1(|\mathbf{r}-\mathbf{R}_i|) \tag{7.3}$$

where the DLVO-like orbitals $\phi_1(r)$ are given by

$$\phi_1(r) = -\lambda_\mathrm{B}\frac{Z^\star e^{\bar{\kappa}a}}{1+\bar{\kappa}a}\frac{e^{-\bar{\kappa}r}}{r}. \tag{7.4}$$

where $\bar{\kappa}^2 = \kappa^2\cosh\bar{\phi}$, and $\bar{\phi}$ is the Donnan potential of the effective system, which is defined through the relation

$$\sinh\bar{\phi} = \frac{Z^\star n}{2c_\mathrm{s}}e^{\eta/(1-\eta)}. \tag{7.5}$$

Inside the cell around colloid i, the electric potential is denoted by $\phi_c(|\mathbf{r}-\mathbf{R}_i|) \equiv \phi(\mathbf{r})$, where $\phi_c(r)$ is determined by the boundary value problem

$$\frac{1}{r^2}\frac{\partial}{\partial r}\left[r^2\frac{\partial}{\partial r}\phi_c(r)\right] = \kappa^2 \sinh\left[\phi_c(r)\right]; \tag{7.6a}$$

$$\phi_c'(a) = \frac{Z\lambda_B}{a^2}; \tag{7.6b}$$

$$\phi_c'(b) = \frac{Q\lambda_B}{b^2}. \tag{7.6c}$$

Note that the first boundary condition (7.6b) still depends on the unknown charge Z.

The charge Z is determined by the minimum of the effective Hamiltonian (7.2) with respect to Z. Using partial differentiation similar to Eq. (6.7), we find

$$\ln\frac{Z}{M-Z} = \phi_c(a) - \beta E \quad \text{or} \quad Z = \frac{M}{1+(c_s/K)\exp[-\phi_c(a)]} \tag{7.7}$$

where $\mathbf{R}_i$ denotes the position of the center of colloid i. For the regions inside the cells, we thus need to solve the coupled set of equations (7.6a)–(7.7) rather than the simple boundary value problem (5.1). Numerically, however, it does not really pose any problem.

To completely determine the electric potential $\phi(\mathbf{r})$ and the charges Z of the colloid and Q of the cell, we need to demand that the potential and the electric field are continuous at the cell boundaries. This translates into the relations

$$\begin{cases} \phi_c(b) = \phi_\ell(b\hat{\mathbf{r}}); \\ \phi_c'(b) = \hat{\mathbf{r}}\cdot\nabla\phi_\ell(b\hat{\mathbf{r}}), \end{cases} \tag{7.8}$$

where $\phi_c(b)$ is determined by Eqs. (7.6a)–(7.7), and $\phi_\ell(b\hat{\mathbf{r}})$ and $\nabla\phi_\ell(b\hat{\mathbf{r}})$ are given by Eqs. (5.12a) and (5.12b). This set of equations can for example be solved by the procedure outlined in Fig. 5.2 and described in Section 5.2.

This procedure fixes the potential $\phi(\mathbf{r})$ and the charges Q and Z for given values of M, λ_B, η, κ, K, a and b. The cell radius b is still a free parameter. It is fixed in the same way as already discussed in Section 5.3: we determine the cell radius b from the condition

$$|\phi_c(b) - \tilde{\phi}| \approx 1, \tag{7.9}$$

or $b = a$ if $|\phi_c(a) - \tilde{\phi}| < 1$.

The effective Hamiltonian of the multi-centered non-linear charge-regulated theory, finally, is given by

$$\beta H = \beta\Phi_c^{(\text{regul})} + \beta\Phi_D + \beta\Phi_0' + \left\{1 - \Upsilon(\bar{\kappa}a)\right\}\sum_{i<j} V_2(R_{ij}; Z^\star, \bar{\kappa}), \tag{7.10}$$

which is identical to the effective Hamiltonian of the theory with fixed charges, as given by Eq. (5.28), except for the cell contribution $\Phi_c^{(\mathrm{regul})}$. The Donnan contribution Φ_D was defined in Eq. (5.23) and the volume term Φ_0' in Eq. (5.30). The factor $\Upsilon(x)$ is given by Eq. (5.27), and the pair potential $V_2(R_{ij})$ was defined in Eq. (2.16). The cell contribution is simply equal to $\Phi_c^{(\mathrm{regul})} = \Phi_c + F_s(M, Z)$, where Φ_c is the cell contribution (5.29) of the fixed-charge theory, and F_s is the charge regulation contribution of Eq. (7.1). The cell contribution thus becomes

$$\begin{aligned}\frac{\beta\Phi_c^{(\mathrm{regul})}}{N} =& 4\pi c_s \int_{\mathrm{cell}} \mathrm{d}r\, r^2 \left\{\phi_c(r)\sinh\phi_c(r) - 2\cosh\phi_c(r)\right\} \\ &+ \frac{Z}{2}\phi_c(a) - M\ln\left[1 + \frac{K}{c_s}\exp[\phi(a)]\right] - V_{\mathrm{cell}}\sum_{\alpha=\pm}\tilde{\rho}_\alpha\left[\ln\frac{\tilde{\rho}_\alpha}{c_s} - 1\right],\end{aligned} \tag{7.11}$$

where $V_{\mathrm{cell}} = \frac{4}{3}\pi(b^3 - a^3)$ is the volume of a cell interior.

With the effective Hamiltonian H given by Eq. (7.10), we calculate the free energy (2.5) that follows from H by exploiting the Gibbs–Bogoliubov inequality as outlined in Appendix C.

7.3 Results

In Fig. 7.1, we show the colloid charge Z as a function of the packing fraction η and the screening constant κa for a system with $M = 10^5$, $a/\lambda_B = 100$ and $K = 32\mu$M (silica). It is clear that the charge decreases with both increasing packing fraction and stronger screening.

Figure 7.1 should be compared to Fig. 6.6, which shows the charge in the regulated *cell* Poisson–Boltzmann theory for the same system parameters. Note that in the current figure 7.1 the range of κa and η is larger than in Fig. 6.6. The data for the charge Z in the current multi-centered non-linear charge-regulated Poisson–Boltzmann model matches the data for the regulated cell model very well.

In Fig. 7.2, we plot the charge for the same system in a slightly different format: we show the colloid charge–size ratio $Z\lambda_B/a$ as a function of the packing fraction η and the screening constant κa for a system with fixed $a/\lambda_B = 100$, $M = 10^5$ and $K = 32\mu$M. The dimensionless quantity $Z\lambda_B/a$ is interesting here, because we have shown in Chapter 5 that in the multi-centered non-linear model with *fixed* charges, spinodal instabilities occur only for systems where $Z\lambda_B/a \gtrsim 100$ (or slightly lower for the spherically symmetric approach described in Section B); see Fig. 5.11. Note that for this particular system in the charge-regulated model, the maximum value of $Z\lambda_B/a$ attained, is $Z\lambda_B/a \approx 7.5$.

In Fig. 7.3, we show the quantity $Z\lambda_B/a$ as a function of the packing fraction η and the screening constant κa for many different values of the number M of ionizable surface sites and the particle size a/λ_B. Each of the small diagrams in this figure is identical to Fig. 7.2, with the packing fraction $10^{-6} < \eta < 1$ on the horizontal axes and the screening constant $0.01 < \kappa a < 10$ on the vertical axes. Note that

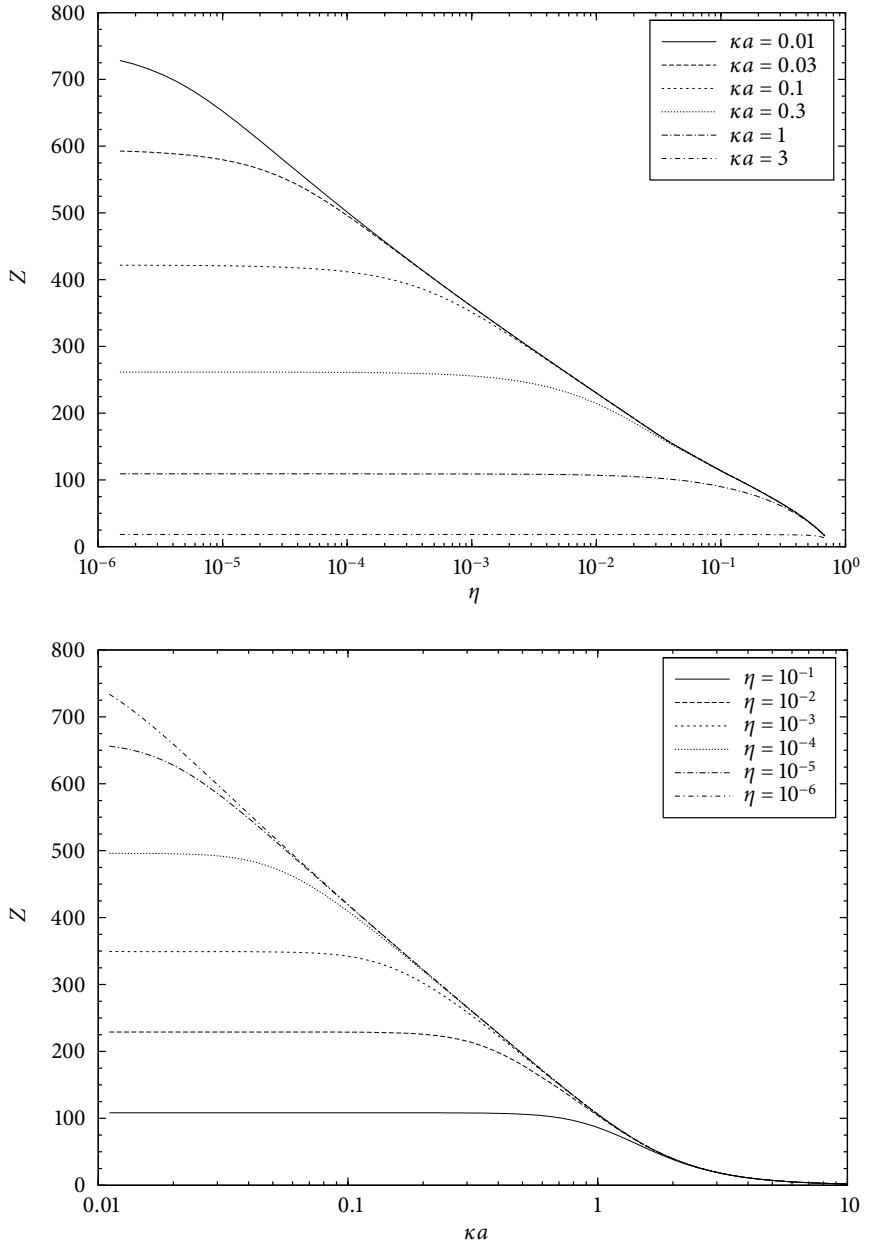

FIGURE 7.1 — The colloid charge Z for a typical colloidal system with fixed $a/\lambda_B = 100$, $M = 10^5$ and $K = 32\mu$M (i.e., silica particles). The top figure shows the charge Z as a function of the colloidal packing fraction η for several values of the screening constant κa. The bottom figure show the charge as a function of the screening κa for several values of the packing fraction. This can be seen to agree well with the charges calculated in the Poisson–Boltzmann cell approximation, as displayed in Fig. 6.6.

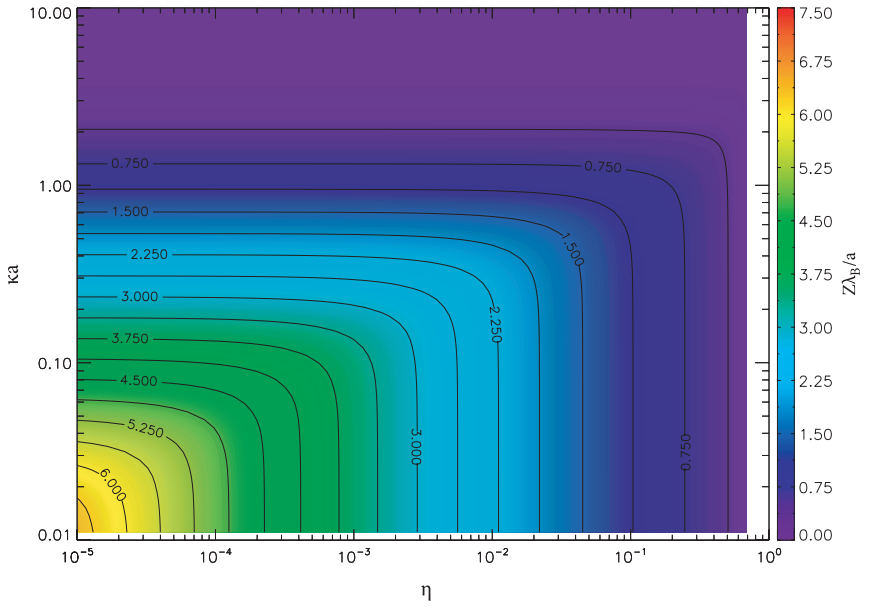

FIGURE 7.2 — The colloid charge $Z\lambda_B/a$ as a function of the packing fraction η and the screening constant κa for a typical colloidal system with fixed $a/\lambda_B = 100$, $M = 10^5$ and $K = 32\mu$M. Observe that the charge is lower than $Z\lambda_B/a \approx 7.5$ in the entire parameter regime $0.01 < \kappa a < 10$ and $10^{-6} < \eta < 0.74$ shown here. The charge is thus too low to result in spinodal instabilities, for which $Z\lambda_B/a \gtrsim 10$–100 is needed in a constant-Z model (see Chapter 5).

for most of these parameters, the quantity $Z\lambda_B/a$ is smaller than 10, and that only in the case of $M = 10^6$ and $a/\lambda_B = 1000$ and $a/\lambda_B = 10^4$, this value is exceeded, but even then the maximum value attained is $Z\lambda_B/a \approx 16$. These values are all too small to induce any spinodal instabilities in the fixed-charge model.

By calculating the free energy F from the effective Hamiltonian (7.10) using the procedure outlined in Appendix C, we calculated the pressure $P = -(\mathrm{d}F)/(\mathrm{d}V)$ and the inverse compressibility $\chi^{-1} = (\mathrm{d}\beta P)/(\mathrm{d}n)$ for the systems of Fig. 7.3. The compressibility is always positive for the systems studied, and thus no spinodal instabilities are present. We therefore conclude that the values of $Z\lambda_B/a$ are indeed too small to give instabilities, and that the density-dependent Z, which in principle could have caused instabilities in the phase-behavior even for low values of $Z\lambda_B/a$, does not affect the stability significantly.

It is not hard to understand why the charge cannot become very large: if Z is large, on the one hand that means, by Gauss's theorem, that the derivative $\phi_c'(a)$ at the colloid surface must be large. A large $\phi_c'(a)$ induces also a large negative value for the electric potential $\phi_c(a)$ at the colloid surface by the non-linear coupling through the Poisson–Boltzmann equation (7.6a). If $\phi(a) \ll -1$, however, the

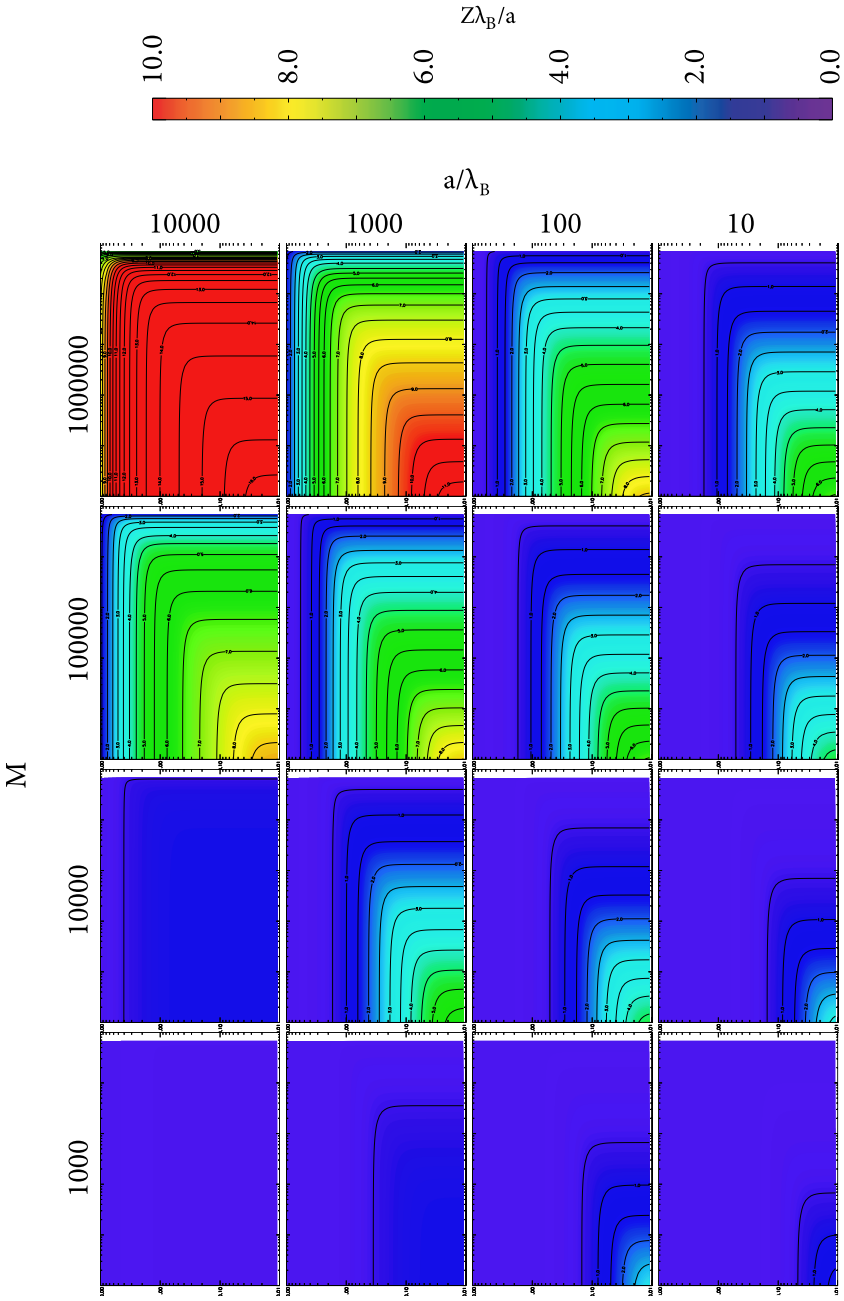

FIGURE 7.3 — The colloid charge $Z\lambda_B/a$ as a function of the packing fraction η and the screening constant κa for a many different colloidal system with varying M (columns) and a/λ_B (rows). The scales of the axes of each of the individual figures are similar to Fig. 7.1, with on the horizontal axes the colloidal packing fraction ranging from $\eta = 10^{-5}$ to $\eta = 0.74$ and on the vertical axes the screening constant κa ranging from $\kappa a = 0.01$ to $\kappa a = 10$. Observe that the highest value for $Z\lambda_B/a$ that is attained in this entire parameter regime is $Z\lambda_B/a \approx 16$ for $M = 10^6$ and $a/\lambda_B = 10^4$ in the low screening and low density regime.

charge Z must be small because of the relation (7.7). This suggests that indeed large values of Z are hard to attain.

The significant computational effort required to generate the phase-diagram Fig. 7.3 has prevented us from studying lower values of a/λ_B, where gas–liquid instabilities may yet be possible. This is work in progress.

7.4 Conclusion

We have extended the multi-centered nonlinear Poisson–Boltzmann theory that was derived in Chapter 5 with a simple charge regulation mechanism, which was first introduced in Chapter 6 in a cell model. We calculated the charges for a large number of systems, and found that for almost all systems $Z\lambda_B/a < 10$. We calculated the effective Hamiltonian and the free energy; the compressibility resulting from the free energy is always positive for the systems studied and no spinodal instabilities were found. We thus conclude that the value of $Z\lambda_B/a$ is too small to induce any spinodal instabilities and the density-dependence of the charge does not induce any instabilities either, at least for the parameter regime investigated so far. The spinodal instabilities that were found in the multi-centered nonlinear Poisson–Boltzmann theory of Chapter 5 are therefore probably very hard to reach in experimental systems.

The charge regulation mechanism that we employed here, was very simple. A more sophisticated model, or use of a different material than silica, might perhaps allow for more highly charged systems in which the broad gas–liquid and gas–crystalline phase coexistences of Chapters 4 and 5 may be experimentally achieved. Also this should be investigated in more detail.

CHAPTER 8

Conclusions and Outlook

In this thesis we studied colloidal suspensions by means of Poisson–Boltzmann theory. The main goal was to explain observations suggesting the presence of cohesive energy in colloidal suspensions at low salinity (see Section 1.5), which cannot be explained by traditional DLVO theory.

The main result of this thesis consists of a new theory for the effective Hamiltonian of suspensions of highly charged colloids at low ionic strengths. This theory, which we constructed in Chapter 5, is based on (mean-field) Poisson–Boltzmann theory and describes non-linear effects such as charge renormalization and quasi-condensation of counter-ions on the colloidal surfaces, while still explicitly taking into account the multi-centered character of the system. The effective Hamiltonian is found to consist of pairwise screened-Coulomb interactions and so-called volume terms; all parameters and quantities can be obtained explicitly, either analytically, or from relatively simple and straightforward numerical computations. Existing theories were either computationally very expensive, or would only take into account either the non-linearity or the multi-centered geometry, reducing the problem either to a non-linear cell-type model, or to a *linear* multi-centered problem.

Using the multi-centered, non-linear theory, we have calculated the phase-behavior of colloidal suspensions for a large range of salt concentrations and colloidal charges, densities, and radii. The results (see Fig. 5.11) show that spinodal instabilities can occur, if the colloidal particles have sufficiently high charges or sufficiently small radii. The cohesion that causes these spinodal instabilities resides in the volume terms. Furthermore, the theory extends in parameter space from (very) highly charged colloids (with charge $Z = 10^3$–10^4) to the 1:1 electrolyte ($Z = 1$), and we have shown that the spinodal instabilities of highly asymmetric

colloidal systems are directly related to the well-established instabilities in the restrictive primitive model.

Additionally, we have included a charge regulation mechanism in this multi-centered nonlinear theory. The resulting model, which is described in Chapter 7, includes the multi-centered nature of the system, the non-linear behavior close to the colloidal surfaces, and additionally, the chemical equilibrium between the micro-ions in solution and those bound to the colloidal surfaces. This extended model shows that it is very hard to experimentally reach the parameter regime where the colloids have sufficiently high net charge to induce a spinodal instability, at least for silica particles.

In Fig. 5.11, we have given a clear overview of the region in parameter space where, at low ionic strength, spinodal instabilities are found on the basis of the theory of Chapter 5; this region is well approximated by the relation $Z\lambda_B/a \geq 25$, where a is the particle radius, and λ_B is the Bjerrum length. This might be an incentive to try and reach these parameters in experimental setups; we have shown in Chapter 7, however, that such high charges are probably hard to obtain. Another area of experimental study might be to measure the net and the effective charges of colloids as a function of the salt concentration and the colloid density for different colloid radii and charges, in order to compare these to the theoretical predictions of Chapters 6 and 7. Although some work has been done on this subject [129, 133, 134], not many quantitative data are available at the moment.

In Monte-Carlo simulations, the highest charges that can be achieved with current techniques do not exceed a few hundred electron charges. Although also the parameter range between $Z = 1$ and $Z = 100$ is interesting, it is fair to say that primitive model simulations have not yet closed the gap to highly charge colloidal systems (with, say, $Z \sim 10^3$–10^4) with added salt. However, progress in this area is fast, and, with increasing computer power becoming available, it is likely that it will become possible to simulate systems with much higher charge in the near future. This should allow for further quantitative tests of the present theory.

Another direction for further research might be the extension of the multi-centered non-linear model of Chapter 5 to other potentials than the simple hard-core Coulomb systems that were studied in this thesis. By adjusting the interactions inside the cells, it should be relatively easy to add specific short-ranged interactions to the model, including for example stickiness, or to make the colloidal core soft, like, for example, in star polymer systems [19]. We therefore expect that the theory developed here will have many more applications and could be a useful tool to study all kinds of colloidal and soft matter systems in the future.

APPENDIX A

Linear Poisson–Boltzmann theory: additional calculations

This Appendix contains some technical calculations that are used in the linear Poisson–Boltzmann theory of Chapter 4

A.1 The grand potential

In this Appendix, we calculate the equilibrium grand potential Ω for the linear Poisson–Boltzmann theory that is described in Chapter 4. We show that upon insertion of this grand potential into Eq. (4.2), the effective Hamiltonian (2.8) can be cast into the form specified by Eqs. (4.23)–(4.26).

In the framework of Density Functional Theory, the equilibrium grand potential is given by the minimum of the functional $\Omega[\rho_+, \rho_-]$ of Eq. (4.7). This minimum is found by inserting the Euler–Lagrange equations (4.13a) and (4.13b) into the functional. This leads to the following expression for the grand potential:

$$\begin{aligned}\frac{\beta\Omega}{V} = &\sum_{\pm} \bar{\rho}_{\pm}\left(\ln\left[\frac{\bar{\rho}_{\pm}}{c_s}\right] - 1\right) + \frac{Zn}{2}\bar{\phi} \\ &+ \eta\beta w_0 \frac{\bar{\rho}_+ + \bar{\rho}_-}{2} + \frac{1}{2V}\int \mathrm{d}\mathbf{r}\, \rho(\mathbf{r})\beta V(\mathbf{r}) \\ &+ \frac{1}{2V}\int \mathrm{d}\mathbf{r}\, \beta W(\mathbf{r})\big(\rho_+(\mathbf{r}) + \bar{\rho}_-(\mathbf{r})\big).\end{aligned} \tag{A.1}$$

The "electrostatic" integral can be evaluated as

$$\begin{aligned}\frac{1}{2V}\int \mathrm{d}\mathbf{r}\,\rho(\mathbf{r})\beta V(\mathbf{r}) =& \frac{1}{2V}\frac{1}{(2\pi)^3}\int \mathrm{d}\mathbf{k}\,\beta V_{\mathbf{k}}\rho_{-\mathbf{k}} \\ =& -\frac{1}{2}\frac{1}{1-\eta}\frac{(\bar{\rho}_+-\bar{\rho}_-)^2}{\bar{\rho}_++\bar{\rho}_-} - \frac{Zn}{2}\bar{\phi} - \frac{n}{2}\frac{Z^2\bar{\kappa}\lambda_{\mathrm{B}}}{1+\bar{\kappa}a} \\ &+ \frac{1}{V}\sum_{i<j}\left\{(1+\frac{\Gamma}{2})\left(\frac{Ze^{\bar{\kappa}a}}{1+\bar{\kappa}a}\right)^2\frac{\lambda_{\mathrm{B}}e^{-\bar{\kappa}R_{ij}}}{R_{ij}}\right\} \\ &- \frac{1}{V}\sum_{i<j}\left\{-Z^2\frac{\lambda_{\mathrm{B}}}{R_{ij}}\right\},\end{aligned} \tag{A.2}$$

where we inserted the Fourier transform $\rho_{\mathbf{k}}$ of $\rho(\mathbf{r})$ from (4.20), and the Fourier transform $V_{\mathbf{k}}$ of $V(\mathbf{r})$, which is given by

$$\beta V_{\mathbf{k}} = -\frac{4\pi}{k^3}\left\{\left(\beta v_0 + Z\frac{\lambda_{\mathrm{B}}}{a}\right)ka\cos ka - \beta v_0 \sin ka\right\}\sum_j e^{i\mathbf{k}\cdot\mathbf{R}_j}. \tag{A.3}$$

The factor $\Gamma/2$ in the fourth term on the right hand side of Eq. (A.2) is caused by the expulsion of micro-ionic charges from the colloid cores, and is given by Eq. (4.27). Note that the first and second term of Eq. (A.2) result from the $\propto k^2\delta(\mathbf{k})$ term in equation (4.20) that did not contribute to the charge density.

In a similar way, the "hard-core" part of the grand potential (A.1) is evaluated as

$$\begin{aligned}\frac{1}{2V}\int \mathrm{d}\mathbf{r}\,\beta W(\mathbf{r})\left(\rho_+(\mathbf{r})+\rho_-(\mathbf{r})\right) =& \frac{1}{2V}\frac{1}{(2\pi)^3}\frac{\bar{\rho}_+-\bar{\rho}_-}{\bar{\rho}_++\bar{\rho}_-}\int \mathrm{d}\mathbf{k}\,\beta W_{\mathbf{k}}\rho_{-\mathbf{k}} \\ =& \frac{1}{V}\frac{\Gamma}{2}\left(\frac{Ze^{\bar{\kappa}a}}{1+\bar{\kappa}a}\right)^2\sum_{i<j}\frac{\lambda_{\mathrm{B}}e^{-\bar{\kappa}R_{ij}}}{R_{ij}},\end{aligned} \tag{A.4}$$

where the Fourier transform of $W(\mathbf{r})$ is given by Eq. (4.17) and where we used that $W(\mathbf{r})[\rho_+(\mathbf{r})/\bar{\rho}_+ + \rho_-(\mathbf{r})/\bar{\rho}_-] \equiv 0$.

Substitution of Eqs. (A.2) and (A.4) into the grand potential (A.1) leads to

$$\beta\Omega = (1+\Gamma)\left(\frac{Ze^{\bar{\kappa}a}}{1+\bar{\kappa}a}\right)^2\sum_{i<j}\lambda_{\mathrm{B}}\frac{e^{-\bar{\kappa}R_{ij}}}{R_{ij}} - Z^2\sum_{i<j}\frac{\lambda_{\mathrm{B}}}{R_{ij}} + \beta\Phi, \tag{A.5}$$

where the "volume term" $\Phi = \Phi_{\mathrm{D}} + \Phi_0$ is given by Eqs. (4.24) and (4.25).

Gathering Eqs. (2.8), (2.2) and (A.5), we find that the effective Hamiltonian can be cast into the form given by Eqs. (4.23)–(4.26).

A.2 Alternative hard-core terms

We have already mentioned that, in Chapter 4, we have used a slightly different definition of the hard-core parameters βv_0 and βw_0 than were used by Van Roij

and Hansen in Refs. [71, 72]. In this Appendix we make this statement explicit and calculate, within the grand-canonical linear Poisson–Boltzmann theory of Chapter 4, the effective Hamiltonian using the definition of the hard-core potentials of Refs. [71, 72].

In contrast to the definition $U_{\pm}(\mathbf{r}) = \pm V(\mathbf{r}) + W(\mathbf{r})$ for the micro-ion–colloid interactions, which we used in Chapter 4, as outlined just above Eq. (4.6a), Van Roij and Hansen used the definition

$$U_{\pm}(\mathbf{r}) = \pm V(\mathbf{r}) + \frac{2\bar{\rho}_{\mp}}{\bar{\rho}_{+} + \bar{\rho}_{-}} W(\mathbf{r}), \tag{A.6}$$

where the potentials $V(\mathbf{r})$ and $W(\mathbf{r})$ are defined in Eqs. (4.6a) and (4.6b). With this definition, the grand potential becomes

$$\begin{aligned}\Omega[\rho_{+}, \rho_{-}] =& \Omega'_{\mathrm{id}}[\rho_{+}] + \Omega'_{\mathrm{id}}[\rho_{-}] + k_{\mathrm{B}}T\lambda_{\mathrm{B}} \int \mathrm{d}\mathbf{r}\, \mathrm{d}\mathbf{r}'\, \frac{\rho(\mathbf{r})\rho(\mathbf{r}')}{|\mathbf{r} - \mathbf{r}'|} \\ &+ \int \mathrm{d}\mathbf{r}\, \rho(\mathbf{r}) V(\mathbf{r}) + \frac{2\bar{\rho}_{+}\bar{\rho}_{-}}{\bar{\rho}_{+} + \bar{\rho}_{-}} \int \mathrm{d}\mathbf{r} \left(\frac{\rho_{+}(\mathbf{r})}{\bar{\rho}_{+}} + \frac{\rho_{-}(\mathbf{r})}{\bar{\rho}_{-}} \right) W(\mathbf{r}),\end{aligned} \tag{A.7}$$

where the ideal-gas functionals $\beta\Omega_{\mathrm{id}}[\rho_{\pm}]$ are defined in Eq. (4.5).

The corresponding Euler–Lagrange equations are then given by

$$\ln \frac{\bar{\rho}_{\pm}}{c_{\mathrm{s}}} + \frac{\rho_{\pm}(\mathbf{r}) - \bar{\rho}_{\pm}}{\bar{\rho}_{\pm}} \pm \phi(\mathbf{r}) + \frac{2\bar{\rho}_{\mp}\beta W(\mathbf{r})}{\bar{\rho}_{+} + \bar{\rho}_{-}} = 0. \tag{A.8}$$

By integrating these equations over the system volume, and using the condition for global charge neutrality, we find that the average densities $\bar{\rho}_{\pm}$ are identical to those given in Eq. (4.12). The Donnan potential $\bar{\phi}$, however, is not given by Eq. (4.11) anymore, but by

$$\bar{\phi} = -\sinh^{-1}\left[\frac{Zn}{2cs} e^{\eta\beta w_0} \right] + \eta\beta w_0 \frac{Zn}{\bar{\rho}_{+} + \bar{\rho}_{-}} \tag{A.9}$$

instead. Although this expression also reduces to the usual Donnan expression in the limit $n \to 0$, it is physically less satisfactory than the result we found in Eq. (4.11), as at high η its sign can become different from that of the colloidal charge $-Ze$.

To calculate the density profiles, we take the following linear combination of the Euler–Lagrange equations (A.8):

$$\frac{\rho_{+}(\mathbf{r})}{\bar{\rho}_{+}} + \frac{\rho_{-}(\mathbf{r})}{\bar{\rho}_{-}} = 2\left(1 - \beta W(\mathbf{r}) + \eta\beta w_0\right); \tag{A.10a}$$

$$\frac{\rho(\mathbf{r}) - \bar{\rho}}{\bar{\rho}_{+} + \bar{\rho}_{-}} = -\left(\phi(\mathbf{r}) - \bar{\phi}\right). \tag{A.10b}$$

Note that, due to the different definition of $U_{\pm}(\mathbf{r})$, the hard-core potential $W(\mathbf{r})$ is now totally decoupled from the charge density $\rho(\mathbf{r})$.

Eq. (A.10a) is identical to Eq. (4.13a), so its solution is again 0 inside the hard cores of the colloids, and given by Eq. (4.15) outside the hard cores, provided that we fix $\beta w_0 = 1/(1-\eta)$.

The second equation (A.10b) is *not* identical to its counterpart Eq. (4.13b). The solution is quite similar though: we need to fix the hard core parameter βv_0 to

$$\beta v_0 = -Z\frac{\bar{\kappa}\lambda_B}{1+\bar{\kappa}a}, \tag{A.11}$$

in order to make sure that the charge density $\rho(\mathbf{r})$ is a multi-centered sum of DLVO profiles. The solution (in $\mathbf{k}$-space) is then given by

$$\begin{aligned}\rho_{\mathbf{k}} =& (2\pi)^3\left\{\bar{\rho}+(\bar{\rho}_+ + \bar{\rho}_-)\bar{\phi}\right\}\frac{k^2}{k^2+\bar{\kappa}^2}\delta(\mathbf{k}) \\ &+ \frac{Z}{1+\bar{\kappa}a}\frac{\cos ka + \frac{\bar{\kappa}}{k}\sin ka}{1+k^2/\bar{\kappa}^2}\sum_j e^{i\mathbf{k}\cdot\mathbf{R}_j},\end{aligned} \tag{A.12}$$

which, in real space, is indeed a multi-centered sum $\rho(\mathbf{r}) = \sum_i \rho_1(|\mathbf{r}-\mathbf{R}_i|)$ with the individual profiles given by Eq. (4.22). Note that Eq. (4.20) and (A.12) only differ in the $\propto k^2\delta(\mathbf{k})$ term. As a consequence, the profiles $\rho(\mathbf{r})$ resulting from those two equations, are identical, but the minimum of the functional differs.

Upon insertion of the equilibrium density profiles into the functional (A.7), we immediately notice that the last term on the right hand side vanishes. The grand potential then becomes

$$\frac{\beta\Omega}{V} = \sum_{\pm}\bar{\rho}_{\pm}\left(\ln\left[\frac{\bar{\rho}_{\pm}}{c_s}\right]-1\right) + \frac{Zn}{2}\bar{\phi} + \frac{\eta}{1-\eta}\frac{2\bar{\rho}_+\bar{\rho}_-}{\bar{\rho}_+ + \bar{\rho}_-} + \frac{1}{2V}\int \mathrm{d}\mathbf{r}\,\rho(\mathbf{r})\beta V(\mathbf{r}).$$

The integral in this expression can now be calculated using Parseval's theorem and the expression (A.3) for the Fourier transform of $V(\mathbf{r})$. The result is

$$\begin{aligned}\frac{1}{2V}\int \mathrm{d}\mathbf{r}\,\rho(\mathbf{r})\beta V(\mathbf{r}) =& \frac{1}{V}\sum_{i<j}\left\{\left(\frac{Ze^{\bar{\kappa}a}}{1+\bar{\kappa}a}\right)^2\frac{\lambda_B e^{-\bar{\kappa}R_{ij}}}{R_{ij}} - Z^2\frac{\lambda_B}{R_{ij}}\right\} \\ &- \frac{n}{2}\frac{Z^2\bar{\kappa}\lambda_B}{1+\bar{\kappa}a} - \frac{1}{2}\frac{(\bar{\rho}_+-\bar{\rho}_-)^2}{\bar{\rho}_+ + \bar{\rho}_-} - \frac{Zn}{2}\bar{\phi},\end{aligned} \tag{A.13}$$

so that the grand potential eventually becomes

$$\beta\Omega = \left(\frac{Ze^{\bar{\kappa}a}}{1+\bar{\kappa}a}\right)^2\sum_{i<j}\lambda_B\frac{e^{-\bar{\kappa}R_{ij}}}{R_{ij}} - Z^2\sum_{i<j}\frac{\lambda_B}{R_{ij}} + \beta\Phi. \tag{A.14}$$

The volume term $\beta\Phi$ is exactly equal to the one that was found previously in Eqs. (4.24) and (4.25); the colloidal pair interaction, however, reduces to a purely DLVO interaction, i.e. the factor Γ we found before, is now equal to 0.

APPENDIX B

Spherically symmetric corrections

As an additional approximation to the calculation of the correction term $\delta\Omega$ of Eq. (5.19) in Chapter 5, we calculate this correction term within a spherically symmetric cell in a spherically symmetric cell in this Appendix. For clarity, this alternative version of the correction term will be denoted by $\delta\Omega'$, and the resulting effective Hamiltonian by H'.

Starting out by calculating the spherically symmetric linear solution of the Poisson–Boltzmann equation (5.2) inside the cell, we find

$$\phi_\ell^{\text{cell}}(r) = \bar{\phi} - \tanh\bar{\phi} + \sum_{\pm} \nu_\pm \frac{\lambda_B}{r} e^{\pm\bar{\kappa}(b-a)} \tag{B.1}$$

where the two constants $\nu_\pm$ are found from the boundary conditions $\phi_\ell^{\text{cell}}(b) = \phi_c(b)$ and $\phi_\ell^{\text{cell}\prime}(b) = \phi_c'(b)$, and are given by

$$\nu_\pm = \frac{(\bar{\kappa}b \pm 1)(\phi_c(b) - \bar{\phi} + \tanh\bar{\phi}) \pm b\phi_c'(b)}{2\bar{\kappa}\lambda_B}. \tag{B.2}$$

By inserting this solution (B.1) into the correction (5.19) to the grand potential, we find

$$\begin{aligned}\frac{\beta\,\delta\Omega'}{N} = &\sum_{\pm} V_{\text{cell}}\bar{\rho}_\pm\left[\ln\frac{\bar{\rho}_\pm}{c_s} - 1\right] + \frac{\bar{\rho}\bar{\phi}}{2}V_{\text{cell}} \\ &- \frac{Z^\star}{2}\left\{\bar{\phi} - \tanh\bar{\phi} + \sum_{\pm}\nu_\pm\frac{\lambda_B}{a}e^{\pm\bar{\kappa}(b-a)}\right\}\end{aligned} \tag{B.3}$$

where $V_{\text{cell}} = \frac{4}{3}\pi(b^3 - a^3)$ is the volume of the cell interior.

Gathering the results (5.17), (5.18) and (B.3), we find that the effective Hamiltonian is given by

$$H' = \Phi_0(Z^\star, \bar{\kappa}, \eta) + \Phi_{\text{D}}(Z^\star, \bar{\kappa}) + \Phi'_{\text{c}}(Z^\star, \kappa) + \sum_{i<j}^{N} V_2(R_{ij}; Z^\star, \bar{\kappa}), \tag{B.4}$$

where $v(R_{ij}; Z^\star, \bar{\kappa})$ is the pair interaction as defined in Eq. (2.16). The first volume term Φ_0 describes the self-energies in the effective system, and is given by Eq. (5.23). The second volume term Φ_{D} describes the Donnan equilibrium, and is given by Eq. (5.22). Finally, the volume term Φ'_{c} describes the excess self-energy of each (nonlinear) cell over the effective system, and is equal to

$$\begin{aligned}\frac{\beta\Phi'_{\text{c}}}{N} =& 4\pi c_{\text{s}} \int_a^b \mathrm{d}r\, r^2 \left\{\phi_{\text{c}}(r)\sinh\phi_{\text{c}}(r) - 2\cosh\phi_{\text{c}}(r)\right\} \\ &+ \frac{Z^\star}{2}\left\{\bar{\phi} - \tanh\bar{\phi} + \sum_{\pm} \nu_{\pm}\frac{\lambda_{\text{B}}}{a} e^{\pm\bar{\kappa}(b-a)}\right\} \\ &- \frac{Z}{2}\phi_{\text{c}}(a) - \frac{\bar{\rho}\bar{\phi}}{2}V_{\text{cell}} - V_{\text{cell}}\sum_{\pm}\bar{\rho}_{\pm}\left[\ln\frac{\bar{\rho}_{\pm}}{c_{\text{s}}} - 1\right],\end{aligned} \tag{B.5}$$

with the $\nu_{\pm}$ given by Eq. (B.2).

Observe that, in the limit $b \to a$, the second term of Eq. (B.5) reduces to $Z^\star\phi(a)/2$ and thus exactly cancels the third term $-Z\phi(a)/2$. Therefore, $\beta\Phi'_{\text{c}} \to 0$ in this limit, and the grand potential explicitly reduces to the expression we found for the linear theory of Chapter 4.

APPENDIX C

Mathematical and numerical methods and techniques

Abstract

We review some of the numerical methods and techniques that were used in the this thesis to calculate the free energy for systems of which the pair potential is known.

C.1 Introduction

The numerical work employed for this thesis is not always completely standard. In this Appendix, we provide an overview of the techniques and the numerical methods that were used to calculate the free energy if the Hamiltonian is known.

Most of this Appendix deals with the use of the Gibbs–Bogoliubov inequality to calculate the free energy of DLVO-fluids and -solids from the pair potential. In Section C.2, we review the general procedure and in C.2.1, we introduce the Gibbs–Bogoliubov inequality. In Section C.3, we apply the Gibbs–Bogoliubov inequality to the fluid phase, and in Section C.5, we do the same for solids. Finally, in Section C.6, we review a technique for easy lattice summations.

C.2 Free energy

In this thesis, we have typically considered systems of N spherical particles, interacting through an effective pair potential and volume terms. The Hamiltonian

effective is thus of the form

$$H = \Phi_0 + \sum_{i=1}^{N} \sum_{j>i}^{N} v_2(|\mathbf{R}_i - \mathbf{R}_j|), \tag{C.1}$$

where Φ_0 is a volume term that can depend on thermodynamic quantities such as temperature, chemical potential, colloid density, etc., but *not* on the positions $\mathbf{R}_i$ of the particles. The last term of Eq. (C.1) denotes the pair interactions in the system; the summation is over all colloid pairs, and $\mathbf{R}_i$ denotes the position of the center of particle i. The pair potential $v_2(r)$ is supposed to be of DLVO form, with a hard-core of radius a and a Yukawa-tail with screening length κ^{-1}, and is defined by

$$\beta V_2(r) = \begin{cases} \infty & r < 2a; \\ Z_>^2 \lambda_B \dfrac{e^{-\kappa r}}{r} & r > 2a, \end{cases} \tag{C.2}$$

where for convenience, we have denoted $Z_> = Ze^{\kappa a}/(1+\kappa a)$, Z is the charge of the colloid, $\beta = 1/k_B T$ is the inverse temperature, and λ_B is the Bjerrum length.

The thermodynamic properties and the phase behavior of the system follow from the free energy, which is related to the Hamiltonian by

$$F = -k_B T \ln\left[\mathrm{tr}_c \exp[-\beta H(\{\mathbf{R}_i\})]\right] = F^{(\mathrm{id})} + \Phi_0 + F^{(\mathrm{exc})}, \tag{C.3}$$

where tr_c denotes the classical trace over the colloid degrees of freedom, as defined in Eq. (2.4). The free energy has been decomposed into three parts on the rightmost side of this equation; the first of these denotes the ideal gas free energy and is given by

$$\beta F^{(\mathrm{id})} = N(\ln[n\mathcal{V}] - 1), \tag{C.4}$$

with $n = N/V$ the colloid density and $\mathcal{V}$ is an irrelevant constant volume that accounts for the kinetic energy and the internal partition function of the colloidal particles. The volume term survives because it is independent of the colloid positions and momenta and thus factors out of the phase-space integral, and the excess free energy can be expressed in terms of the pair potential as

$$F^{(\mathrm{exc})} = -k_B T \ln\left[\mathrm{tr}_c \exp\left[-\beta \sum_{i=1}^{N} \sum_{j>i}^{N} v_2(|\mathbf{R}_i - \mathbf{R}_j|)\right]\right]. \tag{C.5}$$

In the remainder of this Appendix, we disregard the volume term Φ_0 in our calculations, as it factors out of the free energy and does not need to be approximated. It can just be added to the approximated free energy of system as calculated in this Appendix.

The main problem that we are facing when calculating the free energy, is to evaluate the trace in Eq. (C.5), as $F^{(\mathrm{id})}$ and Φ_0 are known analytically. Unfortunately, no analytic way is known to carry out these integrations, which involve a double exponential. Therefore, we need to resort to approximate methods to evaluate it. Here, we exploit the Gibbs–Bogoliubov inequality.

C.2.1 The Gibbs–Bogoliubov inequality

The Gibbs–Bogoliubov inequality [109], which has been derived in many different forms by, for example, Gibbs [110], Bogoliubov [111], and Feynman [135], gives an upper limit for the free energy of a system, expressed in terms of the properties of a so-called reference system. This reference system is described by a Hamiltonian H_{ref} that is of the same form as Hamiltonian (C.1) of the original system, but can have a different, arbitrary, pair potential, i.e.,

$$H_{\text{ref}} = K + \Phi_0 + \sum_{i=1}^{N}\sum_{j>i}^{N} V_{\text{ref}}(|\mathbf{R}_i - \mathbf{R}_j|). \tag{C.6}$$

Here, V_{ref} is the pair potential of the reference system.

The Gibbs–Bogoliubov inequality is based on the following mathematical observation: for any two positive functions $A(\{\mathbf{R}_i\})$ and $B(\{\mathbf{R}_i\})$ which are equally normalized, i.e. for which $\int \mathrm{d}\mathbf{R}^N\, A(\{\mathbf{R}_i\}) = \int \mathrm{d}\mathbf{R}^N B(\{\mathbf{R}_i\})$, the inequality

$$\int \mathrm{d}\mathbf{R}^N\, A(\{\mathbf{R}_i\}) \ln A(\{\mathbf{R}_i\}) \leq \int \mathrm{d}\mathbf{R}^N\, A(\{\mathbf{R}_i\}) \ln B(\{\mathbf{R}_1\}) \tag{C.7}$$

is satisfied. This is easily checked by combining the two integrals, using the elementary inequality $\ln x \leq x - 1$, and exploiting the equal normalization of $A(\{\mathbf{R}_i\})$ and $B(\{\mathbf{R}_i\})$. Substituting $A(\{\mathbf{R}_i\}) = \exp[\beta\{F_{\text{ref}} - H_{\text{ref}}(\{\mathbf{R}_i\})\}]$ and $B(\{\mathbf{R}_i\}) = \exp[\beta\{F - H(\{\mathbf{R}_i\})\}]$ into relation (C.7) and rearranging some terms leads to the Gibbs–Bogoliubov equation

$$F \leq F_{\text{ref}} + \left\langle \sum_{i=1}^{N}\sum_{j>i}^{N} \big(V(|\mathbf{R}_i - \mathbf{R}_j|) - V_{\text{ref}}(|\mathbf{R}_i - \mathbf{R}_j|)\big) \right\rangle_{\text{ref}}, \tag{C.8}$$

which gives an upper bound for the free energy of the original system in terms of quantities of the reference system. The $\langle \ldots \rangle_{\text{ref}}$ on the right hand side of the inequality denotes a thermodynamic average *in the reference system*, i.e., $\langle(\ldots)\rangle_{\text{ref}} = \int \mathrm{d}\mathbf{R}^N \exp[-\beta H_{\text{ref}}](\ldots)/\exp[-\beta F_{\text{ref}}]$. The free energy of the reference system was denoted by F_{ref}.

The way to exploit the Gibbs–Bogoliubov inequality is to take a suitable reference system of which the thermodynamic properties, such as the equation of state and the pair distribution function, are known, and in which the thermodynamic average on the right hand side of Eq. (C.8) can be evaluated explicitly. The minimum of the right hand side of Eq. (C.8) as a function of variational system parameters can can then be used as an approximation of the free energy of the system of interest, i.e., we approximate

$$F \approx \min\left\{ F_{\text{ref}} + \left\langle \sum_{i=1}^{N}\sum_{j>i}^{N} \big(v(|\mathbf{R}_i - \mathbf{R}_j|) - v_{\text{ref}}(|\mathbf{R}_i - \mathbf{R}_j|)\big) \right\rangle_{\text{ref}} \right\}, \tag{C.9}$$

where the minimum is to be taken over (a set of) variational parameters of the reference system.

The choice of the reference system to use depends, of course, greatly on the exact system that is being studied. For our system (C.1), we use two different reference systems: for fluids we use a hard-sphere fluid where the sphere diameter acts as the variational parameter. For solids, we use a classical Einstein solid, with the mean square displacement from the lattice positions as variational parameter.

C.3 The fluid reference state

For fluid phases, a hard-sphere fluid is a suitable reference system to use, as very precise analytical free energy expressions exist for hard-sphere systems, and the thermodynamic average on the right hand side of the Gibbs–Bogoliubov inequality (C.8) can be carried out analytically, as we will show below.

The hard-sphere diameter, which we will denote by d, will be used as the variational parameter in the system. The free energy of the hard-sphere fluid can then be accurately denoted by [136]

$$F_{\text{ref}}(d) = F^{(\text{id})} + F^{(\text{CS})}(\eta_{\text{d}}), \tag{C.10}$$

where $F^{(\text{id})}$ is the ideal gas free energy defined in Eq. (C.4). For the excess free energy due to the hard-core interactions, we use the Carnahan–Starling approximation

$$\beta F^{(\text{CS})}(\eta_{\text{d}}) = \frac{\eta_{\text{d}}(4 - 3\eta_{\text{d}})}{(1 - \eta_{\text{d}})^2}, \tag{C.11}$$

where $\eta_{\text{d}} = n\pi d^3/6$ is the packing fraction of the reference system, which is related to the actual packing fraction η of the system of interest by $\eta_{\text{d}} = \eta(d/2a)^3$.

In a recent comparison of many different hard-sphere equations of state [137], the Carnahan–Starling equation of state was found to give very accurate results up to densities well into the crystalline state ($\eta_{\text{d}} < 0.6$).

We note here that the only dependence of the free energy of the reference system on the hard-sphere diameter is through the effective packing fraction η_{d}; the ideal gas part $F^{(\text{id})}$ does not depend on the hard-sphere radius.

For convenience, we denote the difference between the pair interactions of the original DLVO-system and the hard-sphere reference system by $\Delta V(r)$. It takes the following Yukawa-form:

$$\Delta V(r) \equiv V_2(r) - V_{\text{ref}}(r) = \begin{cases} 0 & r < d; \\ \lambda_{\text{B}} Z_{>}^2 \dfrac{e^{-\kappa r}}{r} & r > d. \end{cases} \tag{C.12}$$

Note that this pair potential no longer contains a hard core; the cores are taken into account by $F^{(\text{CS})}$, provided $d > 2a$.

Introducing the radial distribution function $g_2^{\mathrm{HS}}(\eta_\mathrm{d};r)$ of the hard sphere system (see, e.g., Refs. [108, 138]), the thermodynamic average of this difference of pair potentials as specified in Eq. (C.9) can be expressed as

$$\left\langle \sum_{i=1}^{N}\sum_{j>i}^{N} \Delta V(|\mathbf{R}_i-\mathbf{R}_j|)\right\rangle_{\mathrm{ref}} = \frac{N^2}{2V}\int_{|\mathbf{R}|>d} \mathrm{d}\mathbf{R}\, g_2^{\mathrm{HS}}(\eta_\mathrm{d};|\mathbf{R}|)\Delta V(|\mathbf{R}|), \tag{C.13}$$

where V is the system volume. By substituting the pair potential of Eq. (C.12) and rescaling the integration variable in units of the diameter, this expression can be written as

$$\left\langle \sum_{i=1}^{N}\sum_{j>i}^{N} \Delta V(|\mathbf{R}_i-\mathbf{R}_j|)\right\rangle_{\mathrm{ref}} = NZ_>^2\kappa\lambda_\mathrm{B}\frac{12\eta G(\eta_\mathrm{d};\kappa d)}{\kappa d}, \tag{C.14}$$

where the dimensionless integral $G(\eta_\mathrm{d};t)$ is defined as

$$G(\eta_\mathrm{d};t) = \int_1^\infty \mathrm{d}x\, g_2^{\mathrm{HS}}(\eta_\mathrm{d};x)x\exp[-tx]. \tag{C.15}$$

Note that $G(\eta_\mathrm{d};t)$ is a two-dimensional Laplace transform of the radial distribution function. This Laplace transform was calculated by Bravo Yuste and Santos in Refs. [139, 140] on the basis of a Padé-approximation [132]. Explicitly, their expression for $G(\eta_\mathrm{d};t)$ is given by

$$\frac{12\eta_\mathrm{d}G(\eta_\mathrm{d};t)}{t} = \frac{F(t)e^{-t}}{F(t)e^{-t}-1}, \tag{C.16}$$

where $F(t)$ is the $(2,4)$-Padé-approximant

$$F(t) = \frac{1+L_1t+L_2t^2}{1+S_1t+S_2t^2+S_3t^3+S^4t^3} \tag{C.17}$$

with the coefficients given by

$$L_1 = \frac{1+\frac{1}{2}\eta_\mathrm{d}}{1+2\eta_\mathrm{d}} + \frac{12\eta_\mathrm{d}}{1+2\eta_\mathrm{d}}\left(\tfrac{1}{2}L_2-S_4\right); \tag{C.18a}$$

$$S_1 = -\frac{3}{2}\frac{\eta_\mathrm{d}}{1+2\eta_\mathrm{d}} + \frac{12\eta_\mathrm{d}}{1+2\eta_\mathrm{d}}\left(\tfrac{1}{2}L_2-S_4\right); \tag{C.18b}$$

$$S_2 = -\frac{1}{2}\frac{1-\eta_\mathrm{d}}{1+2\eta_\mathrm{d}} + \frac{1}{1+2\eta_\mathrm{d}}\left[(1-4\eta_\mathrm{d})L_2+12\eta_\mathrm{d}S_4\right]; \tag{C.18c}$$

$$S_3 = -\frac{1}{12\eta_\mathrm{d}}\frac{(1-\eta_\mathrm{d})^2}{1+2\eta_\mathrm{d}} - \frac{1}{1+2\eta_\mathrm{d}}\left[(1-\eta_\mathrm{d})L_2+6\eta_\mathrm{d}S_4\right]. \tag{C.18d}$$

To make the expression (C.16) consistent with the Percus–Yevick equation of state [108, 141], it suffices to take $L_2 = S_4 = 0$. This is a convenient expression to combine

with Verlet–Weis corrections to $g_2^{\mathrm{HS}}(r)$, which will be reviewed in the next section. This is the expression that was used for the calculations in this thesis.

Alternatively, the approximation (C.16) can also be made consistent with the Carnahan–Starling equation of state (C.11) by taking the following choice for the coefficients L_2 and S_4:

$$L_2 = -12\eta_{\mathrm{d}}\frac{1-\eta_{\mathrm{d}}/2}{(1-\eta_{\mathrm{d}})^3}S_4; \tag{C.18e}$$

$$S_4 = -\frac{(1-\eta_{\mathrm{d}})^4}{72\eta_{\mathrm{d}}(\eta_{\mathrm{d}}^3-3\eta_{\mathrm{d}}-1)} \times\left[3-(1+2\eta_{\mathrm{d}})\sqrt{\frac{3(\eta_{\mathrm{d}}^2-5\eta_{\mathrm{d}}+7)}{\eta_{\mathrm{d}}^4-4\eta_{\mathrm{d}}^3+4\eta_{\mathrm{d}}^2+4\eta_{\mathrm{d}}+1}}\right], \tag{C.18f}$$

To conclude, we combine Eqs. (C.9), (C.10), (C.11), and (C.14), and find that the free energy of the fluid state with Hamiltonian (C.1) is approximated by

$$\beta F \approx \beta F^{(\mathrm{id})} + \Phi_0 + \min_d\left\{\beta F^{(\mathrm{CS})}(\eta_{\mathrm{d}}) + NZ_>^2\kappa\lambda_{\mathrm{B}}\frac{12\eta_{\mathrm{d}}G(\kappa d)}{\kappa d}\right\}, \tag{C.19}$$

where $G(t)$ is given by Eqs. (C.16)–(C.18f). The minimization over the effective hard-sphere diameter d can be easily performed numerically (see, e.g., [132, 142]). Such a minimum does indeed exist for all system parameters, as the Carnahan–Starling excess free energy (C.11) diverges to positive infinity as the effective packing fraction becomes very high; the minimal effective diameter is of course given by the physical hard sphere diameter, i.e., $d \geq 2a$.

C.4 Verlet–Weis corrections

If we take a Percus–Yevick approach, and thus choose $L_2 = S_4 = 0$ for the approximation (C.16), we can additionally employ a correction to the pair-distribution function of the hard-sphere system, originally due to Verlet and Weis [143] (see also Ref. [108], Appendix C). Verlett and Weiss proposed these extra corrections to the Percus–Yevick pair distribution function to better match the radial distribution function to data from Monte-Carlo simulations.

They considered the radial distribution function $g_2^{\mathrm{HS}}(\eta;x)$ to be of the form

$$g_2^{\mathrm{HS}\prime}(\eta;x) = g_2^{\mathrm{HS}}(\eta';x) + \delta g(\eta';x) \tag{C.20}$$

where $\eta' = \eta - \eta^2/16$ is a corrected packing fraction and $\delta g(\eta';x)$ is a short-range correction, given by

$$\delta g(\eta';x) = A\frac{\exp[-\alpha(x-2)]\cos[\alpha(x-2)]}{x}. \tag{C.21}$$

The parameters A and α were found by fitting $g_2^{\mathrm{HS}\prime}(\eta; x)$ to Monte-Carlo data, and are given by

$$A = \frac{3\eta'^2}{2}\frac{1 - 0.7117\eta' - 0.114\eta'^2}{(1-\eta')^4}; \tag{C.22a}$$

$$\alpha = 6A\frac{(1-\eta')^2}{\eta'(1+\eta'/2)}. \tag{C.22b}$$

In the specific case we are studying here, this correction has two effects. First of all, in all expressions involving the hard-sphere radial distribution function, i.e., Eqs. (C.10), (C.11), (C.16)–(C.18f) and (C.19), the effective packing fraction η_d needs to be replaced with the Verlett–Weiss-corrected packing fraction $\eta'_\mathrm{d} = \eta_\mathrm{d} - \eta_\mathrm{d}^2/16$. Secondly, an extra term, resulting from the correction term $\delta g(x)$, needs to be added to the function $G(\eta; t)$ of Eq. (C.16). This term is given by

$$\delta G(\eta'; t) = \int_1^\infty \mathrm{d}x\, e^{-xt} x\, \delta g(x) = Ae^{-2t}\frac{t+\alpha}{2\alpha^2 + 2t\alpha + t^2}. \tag{C.23}$$

Incorporating these corrections, the expression (C.19) for the free energy is replaced by

$$\begin{aligned}\beta F \approx \beta F^{(\mathrm{id})} + \min_d \Bigg\{ &\beta F^{(\mathrm{CS})}(\eta_\mathrm{d}) \\ &+ Z_>^2 \kappa\lambda_\mathrm{B}\frac{12\eta'_\mathrm{d}}{\kappa d}\left[G(\eta'_\mathrm{d}; \kappa d) + \delta G(\eta'_\mathrm{d}; \kappa d)\right]\Bigg\},\end{aligned} \tag{C.24}$$

which is also easy to minimize numerically.

C.5 The crystalline reference state

For the crystalline state, we take a different approach than for liquids. The choice of the reference system is now the classical Einstein crystal on a lattice equal to that of the crystal phase of interest, e.g., FCC or BCC. The frequency, or, equivalently, the mean square displacement of the particles from their lattice positions, will now serve as the variational parameter. This approach is based on ideas by Shih [144].

We assume that the crystalline state is perfect, i.e., there are no lattice defects, stacking faults, vacancies in lattice positions or multiple particles at a single lattice position. The potential for each particle around its lattice position is given by a harmonic trap $V(\mathbf{r}) = \frac{1}{2}m\omega^2\mathbf{r}^2$. The free energy of a single particle is thus given by

$$\beta F_1 = -\ln\left[\mathcal{V}^{-1}\int \mathrm{d}\mathbf{r}\, \exp[-\beta V(|\mathbf{r}|)]\right] = \ln\left[\left(\frac{\gamma}{\pi}\right)^{3/2}\mathcal{V}\right] \tag{C.25}$$

where $\gamma^{-1} = 2k_B T/m\omega^2$ is the mean square displacement of the particle in the trap, and will function as the variational parameter.

The free energy of the entire lattice is therefore given by

$$\beta F_{\text{solid,ref}} = N \ln\left[\left(\frac{\gamma}{\pi}\right)^{3/2} \mathcal{V}\right] \tag{C.26}$$

Following Eq. (C.9), we thus find the following expression for the reference free energy of the crystalline phase of the Yukawa system (C.1):

$$F_{\text{solid}} = \min_{\gamma} \left\{ F_{\text{solid,ref}} + F^{(\text{exc})}_{\text{solid}} \right\}, \tag{C.27}$$

where the excess part of the free energy of the crystal is defined as

$$F^{(\text{exc})}_{\text{solid}} = \left\langle \sum_{i=1}^{N} \sum_{j>i}^{N} V_2(|\mathbf{R}_i - \mathbf{R}_j|) \right\rangle_{\text{ref}} \tag{C.28}$$

and the effective colloid–colloid pair potential is given by Eq. (C.2).

The probability distribution $P(r)$ of finding a particle at a distance r from its lattice position, is given by a Boltzmann distribution; in the reference system of non-interacting particles this is simply $P(r) = (\gamma/\pi)^{3/2} \exp[-\gamma r^2]$. Exploiting the fact that all lattice sites are equivalent and placing the origin at an arbitrary lattice site, the excess free energy of the solid can be written as

$$\beta F^{(\text{exc})}_{\text{solid}} = N \sum_{\mathbf{R}\neq\mathbf{0}} \int \mathrm{d}\mathbf{r} \int \mathrm{d}\mathbf{r}'\, P(r) P(r') V_2(|\mathbf{r} - (\mathbf{R} + \mathbf{r}')|), \tag{C.29}$$

where the summation on the right hand side is over the lattice positions outside the origin. By substituting the explicit expression for the pair potential (while neglecting the hard cores), exploiting Parseval's theorem, and evaluating these integrals in momentum space, we find

$$\begin{aligned} \beta F^{(\text{exc})}_{\text{solid}} = \frac{1}{4} Z_>^2 e^{\kappa^2/2\gamma} \sum_{\mathbf{R}\neq\mathbf{0}} \frac{\lambda_B}{R} \Bigg\{ & e^{-\kappa R} \operatorname{erfc}\left[\sqrt{\kappa^2/2\gamma} - R\sqrt{\gamma/2}\right] \\ & - e^{\kappa R} \operatorname{erfc}\left[\sqrt{\kappa^2/2\gamma} + R\sqrt{\gamma/2}\right] \Bigg\}, \end{aligned} \tag{C.30}$$

where $R = |\mathbf{R}|$ is the distance of lattice position $\mathbf{R}$ from the origin, and $\operatorname{erfc}(x) = 1 - \operatorname{erf}(x)$ is the error function complement.

This expression is still somewhat complicated, and because of the lattice sum, it cannot easily be minimized as a function of γ. For simplicity, therefore, we approximate the expression (C.30) as

$$\beta F^{(\text{exc})}_{\text{solid}} \approx \frac{1}{2} Z_>^2 e^{\kappa^2/2\gamma} \sum_{\mathbf{R}\neq\mathbf{0}} \frac{\lambda_B}{R} e^{-\kappa R} \tag{C.31}$$

which is accurate, provided $\gamma D\kappa \gg 1$, where D is the typical nearest-neighbor distance between two particles in the lattice. This approximation turns out to be fairly accurate for the density regimes in which we are interested ($\eta > 0.01$ for the solids).

Gathering these results, we find that the free energy of the solid phase is given by

$$\beta F_{\text{solid}} = \Phi_0 + \min_{\gamma} \left\{ N \ln \left[\left(\frac{\gamma}{\pi} \right)^2 \mathcal{V} \right] + \frac{N}{2} Z_>^2 e^{\kappa^2/2\gamma} S_1 \right\}, \tag{C.32}$$

where the lattice sum S_1 is given by

$$S_1 = \lambda_B \sum_{\mathbf{R} \neq \mathbf{0}} \frac{e^{-\kappa |\mathbf{R}|}}{|\mathbf{R}|} \tag{C.33}$$

with the lattice positions $\mathbf{R}$ determined by the lattice geometry. Note that the lattice sum (C.33) does not depend on the variational parameter γ. Hence, the free energy (C.32) can be analytically minimized with respect to γ. The minimum condition reads

$$\gamma = Z_>^2 \frac{S_1}{6} \frac{e^{\kappa^2/\gamma}}{\kappa^2}, \tag{C.34}$$

the solution of which is given in terms of the Lambert W-function [145] by

$$\gamma = \kappa^2 \left[2W \left(\frac{3}{Z_>^2 S_1} \right) \right]^{-1}. \tag{C.35}$$

The Lambert W-function is defined as the inverse function of $f(W) = We^W$; many good numerical approximations for it are known (see, e.g., [132, 142, 145]).

C.6 Lattice summations

The lattice sum S_1 of Eq. (C.33) can, in principle, be summed by iterating over all lattice sites. For three-dimensional lattices, however, this would mean evaluating a triple summation for a given value of the screening parameter κ. Computationally, it is much more efficient to calculate the number of lattice sites at each distance from an (arbitrarily chosen) origin in advance, and for each evaluation of the sum S_1 only evaluate a one-dimensional iteration over the distance from the origin.

Picking the origin at an arbitrary lattice site, and introducing a set of primitive vectors $\{\mathbf{e}_1, \mathbf{e}_2, \mathbf{e}_3\}$ of a lattice structure [146], any point in the lattice can be decomposed as

$$\mathbf{R} = n_1 \mathbf{e}_1 + n_2 \mathbf{e}_2 + n_3 \mathbf{e}_3, \tag{C.36}$$

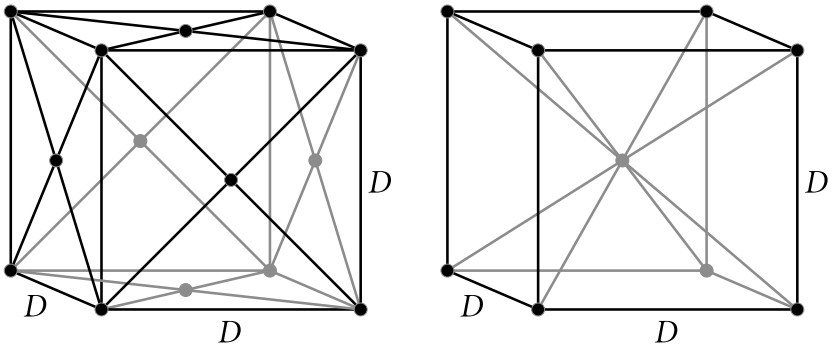

FIGURE C.1 — FCC (left) and BCC (right) lattice structures in the conventional unit cells with edge length D.

	FCC		BCC	
j	$\lvert\mathbf{R}\rvert$	N_j	$\lvert\mathbf{R}\rvert$	N_j
0	0	1	0	1
1	$\frac{1}{\sqrt{2}}D_{\mathrm{FCC}}\sqrt{1}$	12	$\frac{1}{2}D_{\mathrm{BCC}}\sqrt{1}$	0
2	$\frac{1}{\sqrt{2}}D_{\mathrm{FCC}}\sqrt{2}$	6	$\frac{1}{2}D_{\mathrm{BCC}}\sqrt{2}$	0
3	$\frac{1}{\sqrt{2}}D_{\mathrm{FCC}}\sqrt{3}$	24	$\frac{1}{2}D_{\mathrm{BCC}}\sqrt{3}$	8
4	$\frac{1}{\sqrt{2}}D_{\mathrm{FCC}}\sqrt{4}$	12	$\frac{1}{2}D_{\mathrm{BCC}}\sqrt{4}$	6
5	$\frac{1}{\sqrt{2}}D_{\mathrm{FCC}}\sqrt{5}$	24	$\frac{1}{2}D_{\mathrm{BCC}}\sqrt{5}$	0
6	$\frac{1}{\sqrt{2}}D_{\mathrm{FCC}}\sqrt{6}$	8	$\frac{1}{2}D_{\mathrm{BCC}}\sqrt{6}$	0
7	$\frac{1}{\sqrt{2}}D_{\mathrm{FCC}}\sqrt{7}$	48	$\frac{1}{2}D_{\mathrm{BCC}}\sqrt{7}$	0
8	$\frac{1}{\sqrt{2}}D_{\mathrm{FCC}}\sqrt{8}$	6	$\frac{1}{2}D_{\mathrm{BCC}}\sqrt{8}$	12
9	$\frac{1}{\sqrt{2}}D_{\mathrm{FCC}}\sqrt{9}$	36	$\frac{1}{2}D_{\mathrm{BCC}}\sqrt{9}$	0
10	$\frac{1}{\sqrt{2}}D_{\mathrm{FCC}}\sqrt{10}$	24	$\frac{1}{2}D_{\mathrm{BCC}}\sqrt{10}$	0
11	$\frac{1}{\sqrt{2}}D_{\mathrm{FCC}}\sqrt{11}$	24	$\frac{1}{2}D_{\mathrm{BCC}}\sqrt{11}$	24
12	$\frac{1}{\sqrt{2}}D_{\mathrm{FCC}}\sqrt{12}$	24	$\frac{1}{2}D_{\mathrm{BCC}}\sqrt{12}$	8

TABLE C.1 — This table show the number of lattice positions N_j at a distance $\lvert\mathbf{R}\rvert$ around a central lattice position for BCC and FCC lattices. The D_{FCC} and D_{BCC} are the edge lengths of the conventional unit cells for the FCC and BCC lattice, as displayed in Fig. C.1.

for certain n_1, n_2, and n_3. The lattice sum S_1 can hence be written as

$$S_1 = \sum_{n_1=-\infty}^{\infty} \sum_{n_2=-\infty}^{\infty} \sum_{n_3=-\infty}^{\infty}{}' f(|n_1\mathbf{e}_1 + n_2\mathbf{e}_2 + n_3\mathbf{e}_3|), \tag{C.37}$$

with $f(R) = \lambda_B e^{-\kappa R}/R$, and where the prime denotes the exclusion of the term $\{n_1, n_2, n_3\} = (0,0,0)$ in the summations. In the current case, we are only interested in square lattices, so we may assume without loss of generality that each of the primitive lattice vectors is normalized equally, i.e., $|\mathbf{e}_1| = |\mathbf{e}_2| = |\mathbf{e}_3|$. The possible distances between two lattice sites then are given by $\lambda j^{1/2}$ for positive integers j and some number λ that is yet to be determined (see below). The lattice sum can be written as

$$S_1 = \sum_{j=1}^{\infty} N_j f(\lambda\sqrt{j}), \tag{C.38}$$

where N_j denotes the number of lattice sites that are present at a distance $\lambda j^{1/2}$ from the origin.

Note that we have reduced the triple summation in Eq. (C.37) to a single summation in Eq. (C.38). The latter expression is computationally very easy to calculate, assuming the function N_j is known. This function N_j, however, only depends on the lattice geometry and not on the screening κ, and therefore needs to be computed only once and can be stored for later use.

To compute N_j and λ for an FCC and a BCC lattice, we first choose appropriate primitive lattice vectors:

$$\text{FCC}: \qquad \{e_1, e_2, e_3\} = \frac{D_{\text{FCC}}}{2}\big\{(1,1,0),(1,0,1),(0,1,1)\big\}; \tag{C.39a}$$

$$\text{BCC}: \qquad \{e_1, e_2, e_3\} = \frac{D_{\text{BCC}}}{2}\big\{(-1,1,1),(1,-1,1),(1,1,-1)\big\}, \tag{C.39b}$$

where $D_{\text{FCC}} = 2a\sqrt[3]{2\pi/3\eta}$ and $D_{\text{BCC}} = 2a\sqrt[3]{\pi/3\eta}$ are the edge lengths of the conventional cubic unit cells of the FCC and BCC lattices (see Fig. C.1), respectively, expressed in terms of the colloidal radius a and packing fraction η. The square distances in the FCC and BCC lattice are therefore given by

$$\text{FCC:} \quad \mathbf{R}^2 = \frac{D_{\text{FCC}}^2}{2}(n_1^2 + n_2^2 + n_3^2) + \frac{D_{\text{FCC}}^2}{2}(n_1n_2 + n_1n_3 + n_2n_3) \tag{C.40a}$$

$$\text{BCC:} \quad \mathbf{R}^2 = \frac{3D_{\text{BCC}}^2}{4}(n_1^2 + n_2^2 + n_3^2) - \frac{D_{\text{BCC}}^2}{2}(n_1n_2 + n_1n_3 + n_2n_3) \tag{C.40b}$$

where the $-\infty < n_1, n_2, n_3 < \infty$ are integers. Note that thus all distances between lattice points are indeed of the form $\lambda\sqrt{j}$ for some integer j, with $\lambda_{\text{FCC}} = D_{\text{FCC}}/\sqrt{2}$ and $\lambda_{\text{BCC}} = D_{\text{BCC}}/2$ for the FCC and BCC lattice structures, respectively.

The function N_j can easily be pre-calculated by evaluating Eqs. (C.40a) and (C.40b) for all $-n_{\max} < n_1, n_2, n_3 < n_{\max}$ for some (large) cutoff value of $n_{\max}$, and

simply keeping track of the number of lattice sites at distance $\lambda\sqrt{i}$ for integer i. For reference, the function N_j is shown in Table C.1 for a $j \leq 12$.

We exploit this efficient technique to calculate S_1 from Eq. (C.38), hence γ from Eq. (C.35), and hence the free energy of the crystalline phase from Eq. (C.32).

Bibliography

[1] P. G. de Gennes, Rev. Mod. Phys. **64**, 645 (1992).

[2] G. Bosma, C. Pathmamanoharan, E. H. A. de Hoog, W. K. Kegel, A. van Blaaderen, and H. N. W. Lekkerkerker, J. Colloid Interface Sci. **245**, 292 (2002).

[3] K. Butter, A. P. Philipse, and G. J. Vroege, J. Magn. Magn. Mater. **252**, 1 (2002).

[4] C. M. van Kats, P. M. Johnson, J. E. A. M. van den Meerakker, , and A. van Blaaderen, Langmuir **20**, 11201 (2004).

[5] K. Butter, K. Kassapidou, G. Vroege, and A. P. Philipse, J. Colloid Interface Sci. **287**, 485 (2005).

[6] G. A. van Ewijk, G. J. Vroege, and A. Philipse, J. Magn. Magn. Mater. **201**, 31 (1999).

[7] P. M. Johnson, C. M. van Kats, and A. van Blaaderen, Langmuir **21**, 11510 (2005).

[8] R. P. A. Dullens, M. Claesson, D. Derks, A. van Blaaderen, and W. K. Kegel, Langmuir **19**, 5963 (2003).

[9] C. I. Zoldesi, C. A. van Walree, and A. Imhof, Langmuir 22 **22**, 4343 (2006).

[10] A. Yethiraj and A. van Blaaderen, Nature **421**, 513 (2003).

[11] A. van Blaaderen, A. Imhof, W. Hage, and A. Vrij, Langmuir **8**, 1514 (1992).

[12] M. Brunner, C. Bechinger, W. Strepp, V. Lobaskin, and H. von Grünberg, Europhys. Lett. **58**, 926 (2002).

[13] D. G. A. L. Aarts, M. Schmidt, and H. N. W. Lekkerkerker, Science **304**, 847 (2004).

[14] D. Aarts, J. Phys. Chem. B **109**, 7407 (2005).

[15] S. Asakura and F. Osawa, J. Chem. Phys. **22**, 1255 (1954).

[16] A. Vrij, Pure Appl. Chem. **48**, 471 (1976).

[17] Y. Levin, Rep. Prog. Phys. **65**, 1577 (2002).

[18] J.-P. Hansen and H. Löwen, Annu. Rev. Phys. Chem. **51**, 209 (2000).

[19] C. N. Likos, Phys. Rep. **348**, 267 (2001).

[20] M. Dijkstra and R. van Roij, Phys. Rev. Lett. **89**, 208303 (2002).

[21] J. M. Brader, R. Evans, M. Schmidt, and H. Löwen, J. Phys.: Condens. Matter **14**, L1 (2001).

[22] C. Russ, H. H. von Grünberg, M. Dijkstra, and R. van Roij, Phys. Rev. E **66**, 011402 (2002).

[23] M. Brunner, J. Dobnikar, H. H. von Grünberg, and C. Bechinger, Phys. Rev. Lett. **92**, 078301 (2004).

[24] J. Dobnikar, M. Brunner, H. H. von Grünberg, and C. Bechinger, Phys. Rev. E **69**, 031402 (2004).

[25] F. G. Donnan and A. Harris, J. Chem. Soc. **99**, 1554 (1911).
[26] F. G. Donnan, Z. Electrochem. **17**, 572 (1911).
[27] F. G. Donnan, Chem. Rev. **1**, 73 (1924).
[28] K. Mysels, *Introduction to colloid chemistry* (Wiley, New York, 1967).
[29] R. van Roij, J. Phys.: Condens. Matter **15**, S3569 (2003).
[30] A. P. Philipse, J. Phys.: Condens. Matter **16**, S4051 (2004).
[31] M. Rașa, B. H. Erné, B. Zoetekouw, R. van Roij, and A. P. Philipse, J. Phys.: Condens. Matter **17**, 2293 (2005).
[32] B. Derjaguin and L. Landau, Acta Physicochim., URSS **14**, 633 (1941).
[33] J. W. Verwey and J. T. G. Overbeek, *Theory of the stability of lyotropic colloids* (Elsevier, Amsterdam, 1948).
[34] H. C. Hamaker, Physica **4**, 1085 (1937).
[35] E. M. Lifschitz, Sov. Phys. JETP **2**, 73 (1956).
[36] L. Bergström, Adv. Colloid Interface Sci. **70**, 125 (1997).
[37] B. J. Alder and T. E. Wainwright, J. Chem. Phys. **27**, 1208 (1957).
[38] P. N. Pusey, W. van Megen, P. Bartlett, B. J. Ackerson, J. G. Rarity, and S. M. Underwood, Phys. Rev. Lett. **63**, 2753 (1989).
[39] M. J. Stevens and M. O. Robbins, Europhys. Lett. **12**, 81 (1990).
[40] A.-P. Hynninen and M. Dijkstra, Phys. Rev. Lett. **94**, 138303 (2005).
[41] V. Reus, L. Belloni, T. Zemb, N. Lutterbach, and H. Vesmold, J. Phys. II France **7**, 603 (1997).
[42] V. Reus, L. Belloni, T. Zemb, N. Lutterbach, and H. Versmold, Colloids Surf., A **151**, 449 (1999).
[43] E. B. Sirota, H. D. Ou-Yang, S. K. Sinha, P. M. Chaikin, J. D. Axe, and Y. Fujii, Phys. Rev. Lett. **62**, 1524 (1989).
[44] S. H. Chen, E. Y. Sheu, J. Kalus, and H. Hoffman, J. Applied Cryst. **21**, 751 (1988).
[45] C. P. Royall, M. E. Leunissen, and A. van Blaaderen, J. Phys.: Condens. Matter **15**, S3581 (2003).
[46] J. C. Crocker and D. G. Grier, Phys. Rev. Lett. **73**, 352 (1994).
[47] K. Vondermassen, J. Bongers, A. Mueller, and H. Versmold, Langmuir **10**, 1351 (1994).
[48] K. Ito, H. Yoshida, and N. Ise, Science **263**, 66 (1994).
[49] B. V. R. Tata, E. Yamahara, P. V. Rajamani, and N. Ise, Phys. Rev. Lett. **78**, 2660 (1997).
[50] N. Ise, T. Okubo, M. Sugimura, K. Ito, and H. Nolte, J. Chem. Phys. **78**, 536 (1983).
[51] A. E. Larsen and D. G. Grier, Nature **385**, 230 (1997).
[52] B. V. R. Tata, M. Rajalakshmi, and A. K. Arora, Phys. Rev. Lett. **69**, 3778 (1992).
[53] T. Palberg and M. Würth, Phys. Rev. Lett. **72**, 786 (1994).
[54] B. V. R. Tata and A. K. Arora, Phys. Rev. Lett. **72**, 787 (1994).
[55] H. Lowen, Phys. A **235**, 129 (1997).
[56] A.-P. Hynninen, M. Dijkstra, and R. van Roij, J. Phys.: Condens. Matter **15**, S3549 (2003).
[57] A.-P. Hynninen, M. Dijkstra, and R. van Roij, Phys. Rev. E **69**, 061407 (2004).
[58] C. Russ, M. Brunner, C. Bechinger, and H. H. von Grünberg, Europhys. Lett. **69**, 468 (2005).

[59] C. Russ, K. Zahn, and H.-H. von Grünberg, J. Phys.: Condens. Matter **15**, S3509 (2003).

[60] K. Zahn, G. Maret, C. Russ, and H. H. von Grünberg, Phys. Rev. Lett. **91**, 115502 (2003).

[61] A.-P. Hynninen, M. Dijkstra, and A. Z. Panagiotopoulos, J. Chem. Phys. **123**, 84903 (2005).

[62] M. Dijkstra and R. van Roij, J. Phys.: Condens. Matter **10**, 1219 (1998).

[63] P. B. Warren, J. Chem. Phys. **112**, 4683 (2000).

[64] A. Diehl, M. C. Barbosa, and Y. Levin, Europhys. Lett. **53**, 86 (2001).

[65] P. B. Warren (2000), , cond-mat/0006289.

[66] A. R. Denton, Phys. Rev. E **62**, 3855 (2000).

[67] S. N. Petris and D. Y. C. Chan, J. Chem. Phys. **116**, 8588 (2002).

[68] D. Y. C. Chan, P. Linse, and S. N. Petris, Langmuir **17**, 4202 (2001).

[69] P. B. Warren, J. Phys.: Condens. Matter **15**, S3467 (2003).

[70] B. Beresford-Smith, D. Y. C. Chan, and D. J. Mitchell, J. Colloid Interface Sci. **105**, 216 (1985).

[71] R. van Roij and J.-P. Hansen, Phys. Rev. Lett. **79**, 3082 (1997).

[72] R. van Roij, M. Dijkstra, and J.-P. Hansen, Phys. Rev. E **59**, 2010 (1999).

[73] P. Debye and E. Hückel, Phys. Z. **24**, 185 (1923).

[74] L. D. Landau and E. M. Lifšic, *Statistical physics*, Course of theoretical physics; vol. 5 (Pergamon Press, Oxford, 1980), 3rd ed.

[75] V. McGahay and M. Tomozawa, J. Chem. Phys. **97**, 2609 (1992).

[76] M. E. Fisher and Y. Levin, Phys. Rev. Lett. **71**, 3826 (1993).

[77] Y. Levin and M. Fisher, Physica A **225**, 164 (1996).

[78] A. Z. Panagiotopoulos and M. E. Fisher, Phys. Rev. Lett. **88**, 045701 (2002).

[79] D. W. Cheong and A. Z. Panagiotopoulos, J. Chem. Phys. **119**, 8526 (2003).

[80] V. Lobaskin and P. Linse, J. Chem. Phys. **109**, 3530 (1998).

[81] V. Lobaskin and P. Linse, J. Mol. Liquids **84**, 131 (2000).

[82] T. Hiemstra, J. C. M. De Wit, and W. H. Van Riemsdijk, J. Colloid Interface Sci. **133**, 105 (1989).

[83] S. Alexander, P. M. Chaikin, P. Grant, G. Morales, P. Pincus, and D. Hone, J. Chem. Phys. **80**, 5776 (1984).

[84] V. Kralj-Iglič and A. Iglič, J. Phys. II France **6**, 477 (1996).

[85] I. Borukhov, D. Andelman, and H. Orland, Phys. Rev. Lett. **79**, 435 (1997).

[86] R. Evans, Adv. Phys. **28**, 143 (1979).

[87] R. Evans, *Fundamentals of inhomogeneous fluids* (Dekker, New York, 1992), chap. Density functionals in the theory of nonuniform fluids, pp. 85–175.

[88] H. Löwen, P. A. Madden, and J. P. Hansen, Phys. Rev. Lett. **68**, 1081 (1992).

[89] H. Löwen, J.-P. Hansen, and P. A. Madden, J. Chem. Phys. **98**, 3275 (1993).

[90] M. Fushiki, J. Chem. Phys. **97**, 6700 (1992).

[91] J. Dobnikar, Y. Chen, R. Rzehak, and H. H. von Grünberg, J. Phys.: Condens. Matter **15**, S263 (2003).

[92] E. Trizac, L. Bocquet, M. Aubouy, and H. von Grünberg, Langmuir **19**, 4027 (2003).
[93] E. Trizac and Y. Levin, Phys. Rev. E **69**, 031403 (2004).
[94] Y. Levin, E. Trizac, and L. Bocquet, J. Phys.: Condens. Matter **15**, S3523 (2003).
[95] E. Trizac, L. Bocquet, and M. Aubouy, Phys. Rev. Lett. **89**, 248301 (2002).
[96] L. Bocquet, E. Trizac, and M. Aubouy, J. Chem. Phys. **117**, 8138 (2002).
[97] H. H. von Grünberg, R. van Roij, and G. Klein, Europhys. Lett. **55**, 580 (2001).
[98] M. N. Tamashiro and H. Schiessel, J. Chem. Phys. **119**, 1855 (2003).
[99] Y. Levin, M. C. Barbosa, and M. N. Tamashiro, Europhys. Lett. **41**, 123 (1998).
[100] J. T. G. Overbeek, Prog. Biophys. Biophys. Chem. **6**, 57 (1956).
[101] L. Belloni, Colloids Surf. A **140**, 227 (1998).
[102] R. A. Marcus, J. Chem. Phys. **23**, 1057 (1955).
[103] J. Dobnikar, Y. Chen, R. Rzehak, and H. H. von Grünberg, J. Chem. Phys. **119**, 4971 (2003).
[104] J. Dobnikar, R. Rzehak, and H. H. von Grünberg, Europhys. Lett. **61**, 695 (2003).
[105] M. Deserno and H. H. von Grünberg, Phys. Rev. E **66**, 011401 (2002).
[106] M. Deserno and C. Holm, *Electrostatic Effects in Soft Matter and Biophysics* (Kluwer, Dordrecht, 2002), vol. 46 of *NATO Science Series II — Mathematics, Physics and Chemistry*, chap. Cell model and Poisson–Boltzmann theory: a brief introduction, ISBN 1-4020-0197-5.
[107] M. Rașa and A. P. Philipse, Nature **429**, 857 (2004).
[108] J.-P. Hansen and I. R. McDonald, *Theory of simple liquids* (Academic Press, London, 1986), ISBN 0-12-323851-X.
[109] A. Isihara, J. Phys. A (Proc. Phys. Soc.) **1**, 539 (1968).
[110] J. W. Gibbs, *Elementary principles in Statistical Mechanics* (Oxford University Press, Oxford, 1902), *chapter XI*.
[111] N. N. Bogoliubov, Dokl. Akad. Nauk SSSR **119**, 244 (1954).
[112] Y. Levin, J. Chem. Phys. **113**, 9722 (2000).
[113] J. M. Caillol, D. Levesque, and J. J. Weis, J. Chem. Phys. **107**, 1565 (1997).
[114] G. Orkoulas and A. Z. Panagiotopoulos, J. Chem. Phys. **110**, 1581 (1999).
[115] Q. Yan and J. J. de Pablo, J. Chem. Phys. **111**, 9509 (1999).
[116] Y. Levin and M. E. Fisher, Physica A **225**, 164 (1995).
[117] P. M. Biesheuvel, J. Phys.: Condens. Matter **16**, L499 (2004).
[118] P. Linse, J. Chem. Phys. **113**, 4359 (2000).
[119] R. van Roij and R. Evans, J. Phys.: Condens. Matter **11**, 10047 (1999).
[120] R. van Roij, J. Phys.: Condens. Matter **12**, A263 (2000).
[121] M. E. Fisher, J. Phys.: Condens. Matter **8**, 9103 (1996).
[122] Y. Monovoukas and A. P. Gast, J. Colloid Interface Sci. **128**, 533 (1989).
[123] H. Wennerström, B. Jönssen, and P. Linse, J. Chem. Phys. **76**, 4665 (1982).
[124] G. S. Manning, Q. Rev. Biophys. **11**, 179 (1978).
[125] G. V. Ramananthan, J. Chem. Phys. **88**, 3887 (1988).
[126] M. Knott and I. J. Ford, Phys. Rev. E **63**, 31403 (2001).
[127] A.-P. Hynninen and M. Dijkstra, J. Chem. Phys. **123**, 244902 (2005).

[128] H. H. von Grünberg, J. Colloid Interface Sci. **219**, 339 (1999).

[129] T. Gisler, S. F. Schulz, M. Borkovec, H. Sticher, P. Schurtenberger, B. D'Aguanno, and R. Klein, Journal of Chemical Physics **101**, 9924 (1994).

[130] B. W. Ninham and V. A. Parsegian, J. Theor. Biol. **31**, 405 (1971).

[131] S. Kawaguchi, A. Yekta, and M. A. Winnik, J. Colloid Interface Sci. **176**, 362 (1995).

[132] W. H. Press, B. P. Flannery, S. A. Teukolsky, and W. T. Vetterling, *Numerical recipes in C* (Cambridge University Press, Cambridge, 1992), 2nd ed., ISBN 0521431085.

[133] L. Shapran, M. Medebach, P. Wette, T. Palberg, H. J. Schöpe, J. Horbach, T. Kreer, and A. Chatterji, Coll. Surf. A **270–271**, 220 (2005).

[134] P. Wette, H. J. Schöpe, and T. Palberg, J. Chem. Phys. **116**, 10981 (2002).

[135] R. P. Feynman and M. Cohen, Phys. Rev. **102**, 1186 (1956).

[136] N. F. Carnahan and K. E. Starling, J. Chem. Phys. **51**, 635 (1969).

[137] A. Mulero, C. Galán, and F. Cuardros, Phys. Chem. Chem. Phys. **3**, 4991 (2001).

[138] L. Reichl, *A Modern Course in Statistical Physics* (Edward Arnold Publishers Ltd, 1980), ISBN 0-7131-2789-9.

[139] S. Bravo Yuste and A. Santos, Phys. Rev. A **43**, 5418 (1991), *note that this article contains typos in essential formulas; these errors were pointed out and corrected in Ref. [140].*

[140] S. Bravo Yuste, M. López de Haro, and A. Santos, Phys. Rev. E **53**, 4820 (1996).

[141] J. K. Percus and G. J. Yevick, Phys. Rev. **110**, 1 (1958).

[142] M. Galassi, J. Davies, J. Theiler, B. Gough, G. Jungman, M. Booth, and F. Rossi, *GNU Scientific Library Reference Manual* (Network Theory Ltd, 2005), revised 2nd ed., ISBN 0954161734.

[143] L. Verlet and J.-J. Weis, Phys. Rev. A **5**, 939 (1972).

[144] W. Y. Shih, I. A. Aksay, and R. Kikuchi, J. Chem. Phys. **86**, 5127 (1987).

[145] E. W. Weisstein, *Lambert w-function*, From MathWorld—A Wolfram Web Resource. http://mathworld.wolfram.com/LambertW-Function.html.

[146] N. W. Ashcroft and N. D. Mermin, *Solid state physics* (Saunders College Publishing, 1976).

Samenvatting

Zachte materie

Het onderwerp van dit proefschift zijn zogenaamde colloïden. Colloïden zijn feitelijk microscopische deeltjes met diameters tussen een nanometer en een micrometer. Zulke deeltjes zijn enerzijds zo klein dat ze slechts onder een microscoop kunnen worden waargenomen, maar aan de andere kant wel veel groter dan atomen en moleculen.

Colloïden zijn een vorm van zogenaamde 'zachte materie', waartoe ook onder meer eiwitten, DNA-moleculen, virusdeeltjes, celwanden, yoghurt, kunststoffen, rubber en andere polymeersystemen behoren. De gezamenlijke eigenschap van al deze systemen is inderdaad dat ze "zacht" zijn: flexibel en buigzaam.

Het feit dat er in de meeste systemen zo veel verschillende soorten deeltjes voorkomen, in allerlei vormen, en van allerlei groottes, is een van de redenen dat het moeilijk is de eigenschappen van zachte-materiesystemen uit te rekenen. Colloïden kunnen bijvoorbeeld 10000 keer zo groot zijn als de watermoleculen waartussen ze zich bewegen, maar om het hele systeem goed te beschrijven moeten wel al deze deeltjes op een of andere manier worden meegenomen. Bovendien zijn er meestal, bahalve de deeltjes waaruit het oplosmiddel bestaat, ook nog andere deeltjes aanwezig in het systeem, zoals zoutionen of polymeerketens. Terwijl we vooral geïnteresseerd zijn in het gedrag van de grote, zachte-materiedeeltjes, beinvloedt de aanwezigheid van de kleine achtergronddeeltjes de manier waarop de grotere deeltjes met alkaar interageren. Zo blijkt bijvoorbeeld dat grote colloïden elkaar een beetje gaan aantrekken als je er kleine polymeren aan toevoegt. Door de interacties tussen de polymeren onderling en de polymeren met de colloïdale deeltjes in rekening te brengen, is het mogelijk om precies uit te rekenen hoe de aanwezigheid van de polymeren de interacties tussen de andere deeltjes beïnvloedt.

Er is de laatste tijd veel aandacht voor systemen van zachte materie, zowel vanuit de industrie als vanuit de fundamentele wetenschap. De aandacht vanuit de industrie is begrijpelijk als je bedenkt wat voor soort systemen er allemaal onder de noemer "zachte materie" vallen: dat varieert van toepassingen in de cosmetische en de voedingsmiddellenindustrie (huid- en zonnebrandcrême, shampoo en yoghurt zijn allemaal voorbeelden van zachte materie) tot moderne LCD en TFT

computer- en televisieschermen. Enkele bekende recente toepassingen zijn elektronisch papier en fotonische materialen voor optische computerchips.

Vanuit een fundamenteel oogpunt zijn systemen van zachte materie vooral interessant omdat ze, vanwege hun grootte en lage snelheid, relatief gemakkelijk kunnen worden bestudeerd: terwijl voor onderzoek aan traditionele gecondenseerde materie bijvoorbeeld verstrooiingsexperimenten nodig zijn, kunnen zachtemateriesystemen simpelweg onder een optische microscoop worden bekeken. Het is zelfs mogelijk om filmopnamen te maken van deeltjes in zulke systemen om hun beweging via de computer te analyseren. Bovendien kunnen de deeltjes ook via een zogenaamd laser-pincet individueel worden verplaatst of gevangen.

Wat het gebied van zachte materie nog eens extra interessant maakt, is dat het zich afspeelt op de grens van de natuurkunde, de scheikunde en de (moleculaire) biologie. Celmembranen en oplossingen van DNA-moleculen zijn typische voorbeelden van zachte materie, die in biologische systemen alleen kunnen worden begrepen door de chemie van de DNA-moleculen en de natuurkunde van hun interacties met de waterige omgeving en de daarin aanwezige ionen te combineren.

Colloïden

Zoals gezegd zijn colloïden een specifieke vorm van zachte materie: het zijn suspensies van microscopische deeltjes in een oplosmiddel als water of alcohol. Bekende voorbeelden zijn inkt (een oplossing van pigmentdeeltjes in water of alcohol), latex-verf (oplossing van rubberachtige polymeren in water), klei (dunne, hard schijfjes in water) of vetdeeltjes in bijvoorbeeld melk. In de suspensie zijn vaak ook nog andere chemische componenten aanwezig, zoals polymeerketens, eiwitten, of zoutionen. De colloïdale deeltjes zelf zitten qua grootte in tussen een nanometer (grofweg tien keer zo groot als een atoom) en een micrometer (ongeveer honderd keer zo klein als de dikte van een menselijke haar), en kunnen allerlei verschillende vormen hebben.

Colloïdale deeltjes kunnen in het laboratorium onder een optische microscoop worden gevolgd en gefilmd; de posities en de bewegingen van de deeltjes kunnen dan later met de computer worden geanalyseerd. Bovendien is het mogelijk om een of meerdere deeltjes op individueel niveau te manipuleren door middel van een laser-pincet. In zo'n laser-pincet wordt een deeltje gevangen in een laserstraal, en kan hij bijvoorbeeld naar een andere positie in het systeem worden versleept, of hij kan juist netjes op zijn positie worden gehouden. Door zo'n laser-pincet met de computer aan te sturen, is het mogelijk om honderden deeltjes tegelijk op te sluiten of te manipuleren.

Het is tegenwoordig mogelijk om veel verschillende vormen en soorten colloiden te maken in het laboratorium: bollen, plaatjes, naalden, deeltjes met een halter-vorm, holle bollen, enz. Deze deeltjes kunnen bovendien uit allerlei verschillende materialen bestaan, zoals metalen (bijv. goud, aluminium of ijzer), glas, rubber, of plastic. Bovendien is het tegenwoordig mogelijk om heel veel van (vrij-

wel) precies dezelfde deeltjes te maken, zodat bijvoorbeeld alle bollen dezelfde diameter hebben, en mooi rond zijn. Dit is belangrijk, omdat eventuele verschillen tussen de deeltjes afwijkingen kunnen geven in experimenten.

De specifieke colloïdale systemen waar dit proefschrift over gaat, zijn harde bollen (van bijvoorbeeld glas of plastic) in water of alcohol. Bij het oplossen van zulke colloïden in water, treedt een chemische reactie op waarbij positief geladen zoutdeeltjes (de zogeheten counterionen) zich losmaken van het oppervlak van de colloïden, en daarbij een negatieve lading achterlaten op het oppervlak. Hierdoor krijgen de colloïden dus allemaal een negatieve lading en stoten ze elkaar af. De precieze grootte van de lading, en dus de sterkte van de afstoting tussen de deeltjes, hangt af van allerlei factoren; het materiaal waaruit de colloïden bestaan is uiteraard belangrijk, maar ook de temperatuur en het soort oplosmiddel dat is gebruikt.

Belangrijk is verder dat colloïdale suspensies behalve de colloïden zelf, het oplosmiddel en de counterionen, ook nog extra zoutionen bevatten. Deze zouten splitsen zich namelijk in een positief en een negatief ion op het moment dat ze oplossen, en worden daardoor aangetrokken of afgestoten door de colloïden. Het zout kan expres zijn toegevoegd (bijvoorbeeld keukenzout) om de eigenschappen van het systeem te veranderen, maar het kan ook gewoon vervuiling zijn door bijvoorbeeld koolzuur uit de lucht die oplost. Bovendien hebben de meeste oplosmiddelen ook van nature een minimale hoeveelheid aanwezige zoutionen; een liter zuiver, gedestilleerd water bevat bijvoorbeeld altijd minimaal 2 microgram aan H^+ en OH^--ionen.

DLVO-theorie

De traditionele manier waarom zulke suspensies van hoog geladen, bolvormige colloïden worden beschreven, is door middel van zogenaamde DLVO-theorie. Deze is in de jaren '40 ontwikkeld door de Nederlanders Verwey en Overbeek en door de Russen Derjaguin en Landau.

In deze theorie speelt de aanwezigheid van extra zoutionen in de suspensie een belangrijke rol. De colloïden zijn negatief geladen en stoten elkaar dus af; een gedeelte van de zoutionen is echter positief geladen, en wordt dus juist aangetrokken door de veel grotere colloïdale deeltjes. Deze positieve zoutionen vormen daardoor een wolk van positieve lading om het negatief geladen colloïd-deeltje, en schermt daardoor de lading van het deeltje voor een groot deel af. Netto komt dit effect erop neer dat de afstoting tussen de colloïden sterk wordt afgezwakt. De mate van afzwakking, en de grootte van de zoution-wolken rondom de deeltjes, hangt echter af van de totale hoeveelheid zout die in het systeem aanwezig is: is er veel zout, dan zitten de zoutionen dicht bij het oppervlak van de deeltjes en is de afscherming groot. Bij lage zoutconcentraties daarentegen, bevinden de zoutdeeltjes zich verder van de oppervlakken van de colloïden, en is de afscherming minder groot.

Als nu de zoutconcentratie lager en lager wordt gemaakt, worden de wolken dus steeds uitgestrekter, tot op een gegeven moment de zoution-wolken van nabu-

rige deeltjes gaan overlappen. De grootte van de ionenwolken en de sterkte van de afscherming door de zoutionen wordt dan dus ook afhankelijk van de aanwezigheid van naburige colloïden. Deze situatie treedt op bij zeer lage zoutconcentraties, die pas sinds het eind van de jaren '80 experimenteel haalbaar bleken. Deze situatie wordt echter niet meer beschreven door de DLVO-theorie, en vereist dus een andere aanpak.

Fasegedrag

In een gas kunnen de gasdeeltjes zich vrijelijk bewegen, zonder dat ze veel andere deeltjes tegenkomen. In een vaste stof daarentegen zitten de deeltjes ieder op een vaste positie, waaromheen ze hooguit een beetje kunnen trillen. Een vloeistof zit hier een beetje tussenin: de deeltjes zitten niet vast in een kristal en kunnen in principe nog vrij bewegen, maar ze botsen vaak met naburige deeltjes en de dichtheid van een vloeistof is veel hoger dan dat van een gas.

Net als een normale vloeistof die kan verdampen en stollen, kunnen ook colloiden zich als een gas, een vloeistof of een vaste stof gedragen. De colloïdale deeltjes spelen dan dus de rol van de moleculen in het gas, de vloeistof of de vaste stof.

Het blijkt zo te zijn dat een vloeistof–kristal overgang (dus stollen of smelten) heel veel voorkomt in de natuur; hier zijn geen speciale eigenschappen van de deeltjes voor nodig: het is voldoende dat ze elkaar afstoten. Voor een overgang tussen een gas en een vloeistof (verdampen of condenseren), moeten er in het systeem echter aantrekkende krachten aanwezig zijn. Op het eerste gezicht zou je dus zeggen dat in een systeem van gelijk geladen colloïden, die elkaar dus afstoten, alleen een overgang tussen een vloeistof- en een kristalfase kan voorkomen. Die faseovergang is in het verleden uitgebreid bestudeerd en blijkt prima beschreven te kunnen worden op basis van de hierboven beschreven DLVO theorie die de afstotende interacties tussen geladen colloïdale bollen beschrijft.

In de afgelopen 20 jaar zijn er echter experimenten gedaan die lijken te suggereren dat er in colloïdale systemen ook fase-overgangen kunnen plaatsvinden tussen een gas en een vloeistof, of tussen een gas en een vaste stof. Zulke overgangen kunnen niet worden verklaard op basis van de traditionele DLVO theorie. Ze treden bovendien op bij zulke lage zoutconcentraties, en zulke hoge ladingen van de colloïdale deeltjes, dat DLVO-theorie ook niet meer geldig is.

Het onderwerp van dit proefschrift is een nieuwe theorie die deze overgangen wel kan verklaren. De theorie, die wordt afgeleid in hoofdstuk 5, is een combinatie van twee bestaande benaderingen van de zogenaamde Poisson–Boltzmann-theorie, en beschrijft de interacties tussen de colloïdale deeltjes op een effectieve manier. Het blijkt dat, hoewel de interacties tussen de deeltjes, net als in de traditionele DLVO-theorie, nog steeds afstotend zijn, de sterkte van de interacties afhangt van de deeltjesdichtheid. Bovendien blijkt dat de *aantrekkende* kracht tussen de colloïden en de zoutdeeltjes een belangrijke rol speelt, en voldoende cohesie geeft om overgangen tussen een gas en een vloeistof en tussen een gas en een kristal te

kunnen verklaren. We hebben tevens laten zien hoe groot de lading op de colloïden moet zijn voordat dergelijke verschijnselen optreden.

Een extra complicatie in het geheel is, dat de lading van de colloïdale deeltjes niet constant is, maar zelf ook afhangt van de aanwezige concentratie van zoutionen in het systeem: als er veel zoutionen aanwezig zijn, hebben die de neiging om zich op het oppervlak van de colloïden te binden, en neemt de netto lading van de colloïden af. Andersom, als er weinig zout aanwezig is, lossen de deeltjes aan het oppervlak gemakkelijk op, en neemt dus de lading van het colloïd-deeltje toe. Dit evenwicht tussen de ionen in de oplossing en de ionen op het oppervlak van de colloïdale deeltjes hebben we ook in onze theorie verwerkt; deze variant is beschreven in hoofdstuk 7. Het blijkt dat het door dit evenwicht erg lastig is om deeltjes te maken met een lading die hoog genoeg is om de hierboven genoemde verschijnselen te kunnen waarnemen. Dit zou een van de redenen kunnen zijn, waarom het erg moeilijk blijkt om de gas–vloeistof en de gas–kristal overgangen in het laboratorium te reproduceren.

Dankwoord

In de eerste plaats wil ik René bedanken voor zijn goede begeleiding en prettige samenwerking tijdens de afgelopen vier jaar. Hij slaagde er met zijn enthousiasme altijd in om me te motiveren, en zijn fysische intuïtie en talloze ideeën heb ik altijd kunnen voortbouwen.

Albert, Antti-Pekka, Jean-Pierre, Mirçea en Marjolein wil ik bedanken voor vele nuttige en interessante discussies. Ik bedank Henk van Beijeren voor zijn scherpe blik en vele nuttige suggesties tijdens de afronding van mijn proefschrift.

Verder wil ik graag al mijn collega's van het Instituut voor Theoretische Fysica en het Spinoza Instituut bedanken voor de gezellig sfeer, interessante luchdiscussies en leuke instituutsuitjes. Een speciale vermelding verdient Michiel, met wie ik de afgelopen vier jaar met veel plezier een kamer heb gedeeld, en die altijd bereid was te helpen met een fysisch of wiskundig probleem. Ook wil ik mijn direct derde-verdieping collega's Astrid, Dennis, Henk Vocks, Mathijs en Masud bedanken voor vele interessante discussies tijden de luch en de koffie; of het nu ging over virtuele-bomenprogramma's, Ubuntu of wereldpolitiek, ik heb van al onze discussies genoten. Geertje, Biene en Wilma wil ik bedanken voor al hun hulp bij allerhande administratieve en ondersteunende zaken.

Tenslotte bedank ik mijn ouders, Arie en Riet, voor hun steun en interesse in de afgelopen jaren, en Bernard, Dennis, Frank, Jan, Hans, Hendrik, Maaike, Natasja, Ron, Stefan en Sylvain voor vele gezellige koffiepauzes, filmavonden, bioscopenbezoeken en whiskyproeverijen en andere hoognodige afleiding van mijn onderzoek.

Curriculum Vitae

Bas Zoetekouw was born on October 29, 1977 in Tiel, the Netherlands. He attended the Lingecollege in Tiel from 1990, and obtained his gymnasium diploma in 1996. In September of that same year, he started his studies of physics and mathematics at Utrecht University. After completing the propaedeutic exam in both mathematics and physics, he decided to continue in theoretical physics. He wrote a Master's thesis on the subject of "collective excitations in Bose–Einstein condensates" under the supervision of Henk Stoof and Rembert Duine, and graduated *cum laude* in April of 2002.

After graduation, he started his doctoral research under supervision of René van Roij on the subject of the phase behavior of charged colloids. The results of this research are presented in this thesis. During this period, he attended a number of international conferences, schools and workshops, where he also presented the results of his research. Furthermore, he was a teaching assistant for third-year quantum mechanics classes during this period.

In November 2006, he will start as a research scientist at Philips Research.